$Ge_{1-x}Mn_x$/Si (001) Heteroepitaxy: A study of how Mn Incorporates during Molecular Beam Epitaxial growth of Self Assembled Quantum Dots

A Dissertation

Presented to

The faculty of the school of Engineering and Applied Science
University of Virginia

In Partial Fulfillment of the requirements for the degree of

DOCTOR OF PHILOSOPHY

in Materials Science and Engineering

By

Joseph K. Kassim

August

2012

APPROVAL SHEET

The dissertation

is submitted in partial fulfillment of the requirements

for the degree of

Doctor of Philosophy

Joseph Kassim

AUTHOR

The dissertation has been read and approved by the examining committee:

Jerrold A. Floro

Jerrold Floro, Adviser

Petra Reinke, Chairperson

Raul Baragiola, Member

Archie Holmes

Archie Holmes, Member

Dana Elzey, Member

Accepted for the school of Engineering and Applied Science

James H. Ayl

Dean, School of Engineering and Applied Science

August

2012

Abstract

The development of spintronics promises to yield a novel set of spin based devices that offer less power consumption and heat dissipation compared to charge driven devices. The underlying technology exploits the spin degree of freedom of electrons in solid-state devices and seeks to control and manipulate the magnetism in semiconductors through carrier concentration. Group IV dilute magnetic semiconductors (DMS) with room temperature ferromagnetism could be functionalized as a type of fundamental building block for spintronics devices.

Motivated by recent reports of above-room temperature dilute ferromagnetism in Mn-doped Ge quantum dots (QDs) grown by molecular beam epitaxial (MBE) co-deposition on Si (001), we examine the morphology, structure and chemistry of this system in detail. The goal of this work is to correlate the heteroepitaxial growth and the resulting magnetic properties of the Mn_xGe_{1-x}/Si (001) self-assembled QDs as a potential quantum-confined DMS system. DMS strain-induced quantum dots pose a particular challenge to synthesize, since far-above-chemical-equilibrium Mn incorporation in Ge requires low growth temperatures and low surface diffusivity to minimize formation of unwanted phases, while quantum dot self-assembly inherently requires elevated growth temperatures and high surface diffusivity. We systematically explore the effect of the relative Mn:Ge flux during MBE growth. It is a critical focus of this work to clearly ascertain where Mn resides in our Ge-QD/Si (001) films, and in so doing to contribute to our understanding of the basic origins of magnetic ordering in this system.

We synthesized heteroepitaxial self-assembled heteroepitaxial QD's by MBE co-deposition of $Ge_{1-x}Mn_x$ with $x = 0 – 0.16$. Depending on the doping level, Mn is observed

to partition into solution in the Ge QD layer, into arrays of Mn-rich Si solutions buried directly below Ge islands, and into epitaxial and endotaxial Mn silicide phases. In all our Mn-containing films, only low temperature magnetism is observed, with Curie temperatures less than 220 K and saturation moments 4 – 7 μ_B/Mn. The magnetic signal is extremely weak, given that even our most Mn-rich sample contains only 4.7×10^{14} Mn/cm^2 total, required careful analysis and interpretation. Nonetheless, it is clear that we do not observe indications of room temperature ferromagnetism, contrary to recently published results.

Acknowledgements

I wish to express my deepest gratitude to my advisor, Prof. Jerry Floro, for his mentorship, encouragement and believing in me throughout my graduate career. I would never have been able to finish my dissertation without his excellent guidance. His sincere interest in my research, unconditional walk in hours and lengthy science discussion were invaluable for my development as a critical thinker. I could never ask for more.

I also thank my committee: Prof. Reinke, Prof. Baragiola, Prof. Holmes, Prof. Elzey, and Prof. Howe for their continued guidance and critical questioning of my research.

I acknowledge our collaborators Prof. Petra Reinke, and Dr. Christopher Nolph at the University of Virginia, Prof. Matthieu Jamet at CEA/INAC Grenoble, Stephen Smith at Evans Analytical Group. I also gratefully acknowledge Professor Jeff Drucker and Dexin Kong at Arizona State University. Additional research support at NIST and BNL were very resourceful.

I thank the entirety of the University of Virginia Department of Materials Science and Engineering. I thank my closest colleagues, Dr. Christopher Petz, Dr. Melissa Dolph, Dr. Wenjing Yin, Tony Kember, Chris Duska, Priya Ghatwai, Jatin Amatya, Clive Ntuli (UVa E.E dept.)

And lastly, I greatly appreciate all of my family and friends. It was their support that provided the endurance to pursue a decade of higher education. I thank Rev. Carroll Houle in a special way for making my higher education possible.

List of Figures

List of Terms and Symbols

a - lattice parameter
AFM - Atomic force microscopy
d - Interplanar spacing
ε - lattice mismatch
E_B- surface binding energy
E_{coh} - Cohesive film strain
E_{ex} - Exchange energy
FC – Field cooled
FFT - Fast fourier transform
FIB - Focused ion beam
γ - Surface energy
HAADF - High angle annular dark field
HRTEM - High resolution transmission electron microscopy
iFFT - Inverse fast fourier transform
M - Biaxial modulus
m - mass
MBE - Molecular beam epitaxy
MFM - Magnetic force microscopy
ML - Monolayer
N - Number of particles
N_A – Avogadro's number
P - Pressure
PPMS - Physical property measurement system
QCM - Quartz crystal microbalance
QD - Quantum dot
r - radius
R_g - deposition rate
RHEED - Reflection high energy electron diffraction
S-K - Stranski-Krastanov
S-W - Stillinger-Weber
SEM - Scanning electron microscope
SIMS - Secondary ion mass spectroscopy
STEM - Scanning transmission electron microscope
TEM - Transmission electron microscope
TRIM - Transport of Ions in Matter
UHV - Ultra high vacuum
WL - Wetting layer
XTEM - Cross sectional transmission electron microscopy

Brief Author Biography

Joseph Kassim is originally from Nairobi, Kenya. He received his Bachelors of Science, with Distinction in Physics at St. Cloud State University in Spring of 2006, having transferred from Egerton University, Kenya.

Immediately following, Joseph joined Oracle Inc. Minneapolis office. After being accepted at the University of Virginia for graduate school, her left this software engineer position. He commenced his graduate work at the University of Virginia in Fall 2007, completing his Ph.D in 2012 while working in the HyperMBE laboratory of Prof. Jerrold A. Floro. A list of publications and presentations to-date is given below.

Publications

1. J. K. Kassim, C. Nolph, M. Jamet, S. Smith, P. Reinke, J.A. Floro. "Mn Solid Solutions in Self-Assembled Ge/Si (001) Quantum Dot Heterostructures". *Appl. Phys. Lett.* In progress. (2012)
2. J. K. Kassim, C. Nolph, M. Jamet, P. Reinke, J.A. Floro. "$Ge_{1-x}Mn_x$ Heteroepitaxial Quantum Dots: Growth, Morphology and Magnetism". *J. Appl. Phys.* In progress. (2012)
3. J. K. Kassim, C. Nolph, M. Jamet, P. Reinke, J.A. Floro. "Structure and Magnetism of Ternary Intermetallics Formed During Mn Doping of Ge/Si (001) Self-Assembled Quantum Dots". *J. Appl. Phys.* In progress. (2012).

4. C.A. Nolph, J. Kassim, J.A. Floro, and P. Reinke. “Surface Driven Mn doping of Ge Quantum Dots – An STM Study of Mn-Interaction with the Ge QD {105} Facets and the Wetting Layer”. In progress. (2012).

Presentations

1. J. K. Kassim, J.A. Floro. "Mn_xGe_{1-x} /Si (001) Heteroepitaxy: A study of how Mn incorporates during quantum dot self-assembly". *Poster presentation at 2012 Spring Materials Research Society Meeting*, San Francisco, CA, 10 April 2012.
2. J. K. Kassim, J.A. Floro. "Ge1-xMnx Heteroepitaxial Quantum Dots: Growth, Structure and Magnetism". *Oral presentation at International Semiconductor Device Research Symposium (ISDRS)*, University of Maryland College Park, MD, 8 December 2011.
3. J. K. Kassim, J.A. Floro. "Magnetic, structural and morphological characterization of self- assembled dilute magnetic Mn_xGe_{1-x} quantum dots". *Oral presentation at American Vacuum Society Meeting*, Nashville, TN, 2 November 2011.
4. J. K. Kassim, and J.A. Floro. "Heteroepitaxial self-assembly of Ge Quantum Dots on $SrTiO_3$" *Poster presentation at North American Molecular Beam Epitaxy (NAMBE)*, Princeton, NJ, 9-12 August 2009.
5. J. K. Kassim, A. Davidson, M. Paul, A. Gupta, and R. M. Kolagani. “Thickness Dependent Transport Properties of Perovskite Metal Oxide Thin Films.” *Oral presentation at National Conference on Undergraduate Research (NCRU),* University of North Carolina at Asheville, North Carolina, April 6th – 8th 2006.

6. J. K. Kassim, A. Gupta, and R. M. Kolagani. “Thickness Dependent Transport Properties of Manganite Thin Films.” *Oral presentation at Annual Society for Physics Students tri-state conference*, Luther College, Decorah, Iowa , October 2005.

Awards and Funding

1. Center for Nanoscale Materials (Argonne, IL) proposal # 24877 : 2011-2012
2. Research for Undergraduate, NSF grant number DMR -0453342: Summer 2005

Table of Contents

Chapter 1: Introduction

1.1 Motivation

In 1965, Gordon Moore predicted that the number of transistors in an integrated circuit will double approximately every two years. The trend in scaling down of Si based transistors is approaching its physical limitation challenging Moore's Law which has been adhered to for almost half a century. A reduction in device length scale cannot continue indefinitely due to material properties and fundamental limitations of solid state devices. This has led to exploration of new material and qualitatively new solutions for faster, smaller and energy efficient electronics device.

The development of spintronics [1] promises to yield a novel set of spin based devices that offer less power consumption and heat dissipation compared to charge driven devices. The underlying technology exploits the spin angular momentum degree of freedom of the electron in solid-state devices and seeks to control and manipulate the spin state variable in memory application and logic switch rather than charge [2], [3]. The two spin states, spin-up and spin-down, represent the '0' and '1' states in logical operations.

In the last decade, spintronics research has experienced rapid growth, and many of the essential elements of spintronics devices are now in place [1], [4–6]. However, while great progress has been made in some areas, other areas still suffer from the lack of materials "building blocks". Group IV semiconductors, which remain as the foundation of modern microelectronics, can be functionalized as dilute magnetic semiconductors (DMS), a semiconductor hosting small amounts of transition metal atoms (Mn, Fe, Cr, etc.) with typical concentrations of 3 to 8 %. A DMS is a semiconductor that exhibits semiconductor properties as well as a special kind of ferromagnetisms. The spin degree of freedom may also be combined with charge degree of freedom to explore unprecedented applications of spintronics to microelectronics. The electric field control of ferromagnetic transition in dilute magnetic semiconductor (DMS) can be achieved by making use of the ability to readily control carrier concentrations and transport characteristics in semiconductors via doping and gate voltages [7].

Their compatibility with Si-technology, make $Ge_{1-x}Mn_x$ DMS very desirable for spintronics building blocks. The Ge - Si band matching offers potential advantages in lowered interface scattering reduced current and spin polarization losses [8]. Despite their promising candidacy, the experimental realization and synthesis of group IV DMS with room temperature (RT) ferromagnetism (FM) has posed a material science challenge. While major studies of Mn-doped homoepitaxial Ge films (a group IV DMS system) have been performed, much less has been done on magnetic doping of heteroepitaxial group IV quantum dots (QD's) as shall be discussed.

Much less work has been done on magnetic doping of Group IV quantum dots such as Ge dots that self-assemble via heteroepitaxial growth on Si [9–11]. Their ability to spatially localize magnetic moments at the nanoscale [12], possibility of high T_c due to hole confinement [13], and their high crystalline quality makes QD's candidates for the development of spin-based devices. Lyu et al. through theoretical modeling showed that hybridization between the quantum confined holes in the DMS QD's and the itinerant holes in the semiconductor valence band makes holes transfer between QD's. This may induce long range order ferromagnetic ordering of the localized spins [14]. The spin interaction of the electron and hole is enhanced through keeping a single magnetic ion at the center of a quantum dot (QD) and decreasing the size of the QD. This results in a gigantic internal magnetic field larger than that seen in bulk semi-magnetic semiconductors [15]. The exchange interactions between these magnetic nanostructures and hence the ferromagnetic properties [16] can be controlled by varying their size, density and positioning of these dots. Many of these concepts are developed based on a theoretical underpinning, but their experimental realization is often limited by the challenges of the materials synthesis.

It is critical goal of this thesis to study and explore the heteroepitaxial growth and the resulting magnetic properties of the Mn_xGe_{1-x}/Si (001) self-assembled quantum dots (QDs) as a potential DMS system. DMS strain-induced quantum dots pose a particular challenge to synthesize, since far above chemical equilibrium Mn incorporation in Ge requires low growth temperatures and low surface diffusivity to minimize phase separation and formation of unwanted phases, while quantum dot self-assembly invariably requires elevated growth temperatures and high surface diffusivity. We systematically explore the diverse ***growth parameter space*** provided by our hyper-thermal molecular beam epitaxy (HT-MBE) system. The focus is to examine how epitaxial growth schemes promote Mn incorporation and determine the overall ***magnetic response***, while conversely, exploring the Mn impurity affects on epitaxial growth and self-assembly. The goal of this work is to clearly ascertain where Mn incorporates in our films, especially where the magnetically-active Mn resides, and in so doing to contribute to our understanding of the basic origin of ferromagnetic (FM) ordering in this system.

1.2 Literature review

1.2.1 Mn_xGe_{1-x} homoepitaxy

Since the first evidence of hole mediated ferromagnetic ordering in MBE grown 0.1µm thick homoepitaxial layer of $Ge_{1-x}Mn_x$ was first reported in 2002 by Park *et al*, with T_C increasing linearly with Mn concentration from 25 up to 116 K [17], extensive research has been carried out in order to create Mn_xGe_{1-x} group IV DMS materials with a goal of room temperature ferromagnetism for possible spintronics applications [17–20]. To date, there are many reports on $Ge_{1-x}Mn_x$ films grown by molecular beam epitaxy (MB) [17], [21–29], ion implantation [30–36] , and bulk crystal growth [20], [37]. It was shown that $Ge_{1-x}Mn_x$ DMS requires Mn concentration of up to 5% to exhibit FM [38], [39], [26], [40–42]. Fabrication of epitaxial $Ge_{1-x}Mn_x$ DMS films, free of intermetallic precipitates, was reported to require growth rates lower than 0.4 nm/min and low growth temperature (50 °C< T_S < 85 ° C) [42]. Bougeard et al. observed intermetallic free MBE grown 200 nm $Ge_{0.95}Mn_{0.05}$ homoepitaxial films deposited at T_s = 60 ˚C. TEM micrographs revealed cubic clusters which were coherently embedded in the Ge matrix that exhibit dark contrast. [43]. They report that these 15% Mn rich clusters were superparamagnetic with a $\mu_H = 435\ \mu_B$ and $T_c > 160$ K.

Besides reports of precipitate-free dilute $Ge_{1-x}Mn_x$ films [43], [23], Mn segregation and phase separation have also been reported. These effects restrain the homogeneity of these Mn_xGe_{1-x} films [28]. Other results have shown a wide range of Curie temperatures (T_c) between 5 K and 400 K data and contradicting observations [10], [17], [20], [21], [26], [38], [44–50] in the observed ferromagnetism. We therefore lack a suitable approach to prepare these spintronic device structures with reliable performance.

A comprehensive understanding of the relation between structure and magnetism, which is the basis for control of materials properties, has not yet been achieved.

Recently Zeng et al. proposed a new subsurfactant epitaxy approach as a kinetic pathway for Mn incorporation in Ge (100) [51]. They take advantage of the surfactant action of Mn (improving layer by layer growth of Ge) as well as the subsurfactant action of Mn (tendency of pre-MnSi deposited Mn atoms to occupy subsurface interstitials sites located between the two topmost Ge layers) [52]. They deposit Mn atoms on Ge at low temperatures (~150 K and RT), to inhibit lateral diffusion and clustering as well as trapping Mn in interstitial sites. The Mn atoms populate specific subsurface Ge (100) interstitial sites associated with the 2x1 surface reconstruction. As a subsequent Ge layer is deposited. Mn migrates to the new surface and but leaves behind a uniformly distributed small fraction.

1.2.2 Phase separation and surface segregation

Phase separation is a critical challenge in the synthesis of Mn-doped DMS's as mentioned earlier. Mn tends to assume a spherically symmetric magnetic ground state which can be accommodated at extremely low concentrations in the Ge diamond cubic lattice by substituting a Ge atom. However, at concentrations far less that 1 at.%, Ge:Mn in equilibrium will form intermetallic phases as shown in the binary phase diagram Figure 1-1. The low solubility-limit of Mn in Ge, measured to be around 10^{-6} % [113] can limit the use of GeMn as a DMS if grown by equilibrium growth techniques. The Ge:Mn binary phase diagram shows that all the stable phases are on the high-Mn-content side of the phase diagram [114]. This implies that Mn atoms in Ge have a strong tendency to aggregate. Several stable phases observed in equilibrium growth are $Mn_{3.4}Ge$

[115, 116], Mn_7Ge_3 (κ) [115], $Mn_{11}Ge_8$1 [117], Mn_5Ge_3 (η) [118], Mn_2Ge, and Mn_5Ge_2 (ξ). This makes out-of-equilibrium growth techniques necessary to form a metastable diluted system and avoid formation of stable phases.

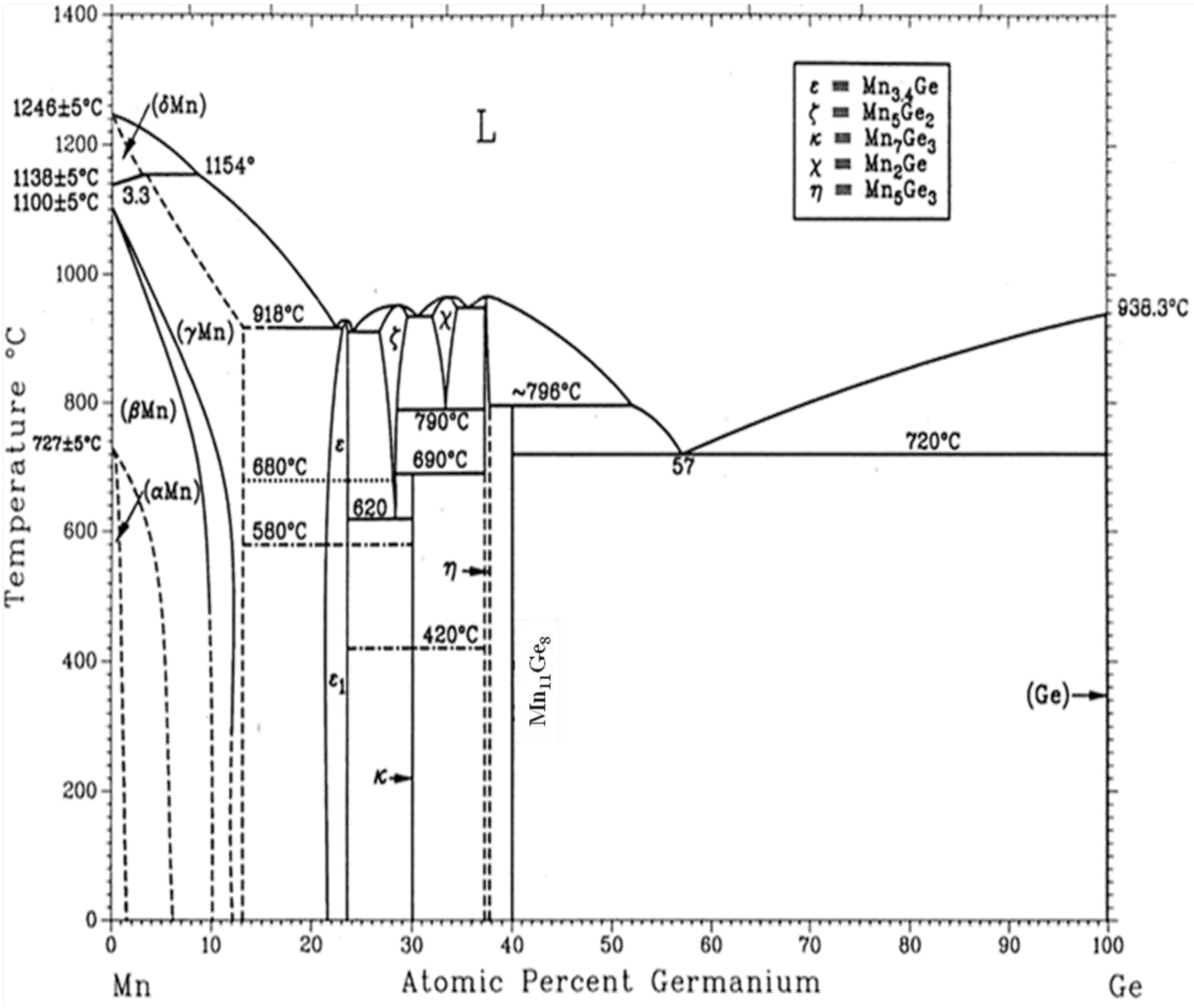

Figure 1-1: Mn-Ge binary alloy phase diagram [53].

Achieving metastable doping levels has been a major limiting factor in exploring the range of magnetic atoms that can be incorporated in the DMS. Various fabrication techniques have been employed to realize Ge:Mn DMS's. Irrespective of the fabrication technique, surface segregation and phase separation were dependent on the growth temperature and growth rate [28], [41], [54]. These secondary phases, particularly

Mn_5Ge_3 ("η" phase) and $Mn_{11}Ge_8$, can be true ferromagnets (Mn_5Ge_3 with a $T_c = 296$ K [55] and $Mn_{11}Ge_8$ with a $T_c = 274$ K [40]), which are undesirable, can confuse interpretation of magnetic measurements, considerably affecting transport properties in Ge:Mn DMS thin films and are detrimental for device applications [38].

Thermodynamic stable phases, mostly Mn_5Ge_3, $Mn_{11}Ge_8$ and Mn_5Ge_2 clusters have been reported. Among others researchers, Ahler et al. [23], Bihler et al [28], Padova et al. [24], Morresi et al. reported Mn_5Ge_3 in 40 nm $Ge_{1-x}Mn_x$ with $x \geq 0.03$ homoepitaxial films grown at $T_s = 160$ ˚C [56]. HRTEM of these cluster reveal several orientation relations (OR) below, Table 1-1.

Orientation Relation	Mn %	Growth conditions	Ref
Mn5Ge3 (0001)/ [$\underline{2}$110] || Ge (001)/[110]	**0.03**	**300nm, T_g=225 ˚C**	[28]
Mn_5Ge_3 (11-23)/[21-31] || Ge (110)/[3-11]	**0.02-0.1**	**40-85nm, T_g=793 ˚C**	[57]
Mn_5Ge_3 (03-30)/[-2110] || Ge (2-20)/[110]	**0.010, 0.033, 0.051**	**40nm, 160 ˚C**	[58]
Mn5Ge3 (0001)/ [11-20] || Ge (001)/[110]	**0.034**	**200nm, T_g=225 ˚C**	[59]
Mn_5Ge_3 (0001)|| Ge (100) OR Mn_5Ge_3 (0001)|| Ge (010)	**0.01-0.11**	**80nm, T_s=600 ˚C**	[46]
Mn_5Ge_3 (0001)/[-2110] || Ge (001)/ [110]	**–**	**T_g = 700-800 ˚C**	[60]

Table 1-1: Observed Mn_5Ge_3 orientation relations.

A particularly thorough study was performed by Lenchner et al., who observed several OR for embedded Mn_5Ge_3 precipitates in 200 nm thin $Ge_{0.966}Mn_{0.034}$ homoepitaxial films on Ge (001) substrates using a combination of synchrotron grazing incidence (GID), coplanar geometry x-ray diffraction (XRD) and transmission electron microscopy (TEM) [61]. They reported two types of clusters: clusters that were buried in the layer versus those that lie close to the surface with different but well defined orientations. They reported two orientations of the Mn_5Ge_3 with respect of the cubic Ge matrix; the c_{hex} – axis of the cluster parallel to Ge [001] and the a_{hex} – axis of the cluster parallel to Ge [110].

Nanocolumn self-assembly has also been observed in GeMn films [62], [48], [45]. Among the several studies of nanocolumn structures, Jamet et al. reported the growth of high T_c (> 400 K) ferromagnetic LT-MBE $Ge_{0.94}Mn_{0.06}$ films containing Mn-rich, self-assembled nanocolumns [26]. They infer that these $MnGe_2$ self nanocolumns form via 2D spinodal decomposition also suggested by Sato et al. for GaMnAs using combined *ab initio* + Monte Carlo calculations [63]. Nanocolumns were also observed by Li et al. as a result of self-organization of the dopant [27]. Their results strongly suggested the need for realistic doping distribution in theoretical modeling.

1.2.3 Room temperature ferromagnetism in Mn-Doped Ge QDs

Mn incorporation in Ge strain-induced quantum dots poses a particular challenge to synthesize, since formation of highly-metastable Mn solutions requires low growth temperatures, whereas quantum dot self-assembly invariably requires elevated growth temperatures necessary of high surface diffusivity. Despite these divergent requirements on Mn mobility, Xiu, et al., (we will refer to them here as “UCLA”) recently showed remarkable results using experimental conditions that closely mirror our own. Given the obvious importance of their results to this work, we will describe this work in further detail here. UCLA grew 8.5 ML of $Mn_{0.05}Ge_{0.95}$ QD’s on a p-type Si (001) substrates by MBE at 450ºC [10]. HR-TEM revealed excellent lattice coherence between the ~30 nm tall and ~ 8 nm wide domes as shown in Figure 1-2. Composition mapping using electron energy loss spectroscopy (EELS) indicates there is Mn in both the domes and in a region directly below the domes. The buried, Mn-enhanced region is also clearly apparent from bright field imaging. A similar diffusion zone had been reported previously in (In, Mn)As and (In, Cr)As QDs systems [64], [65].

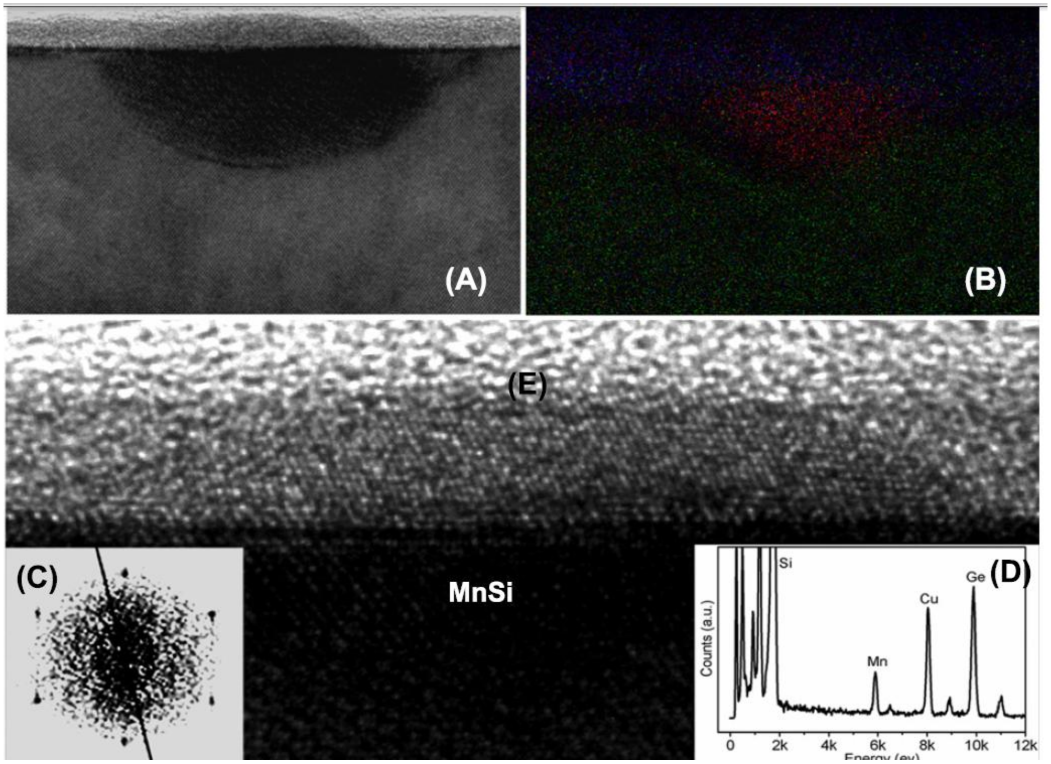

Figure 1-2. The structural properties of $Mn_{0.05}Ge_{0.95}$ QDs grown on a p-type Si substrate. (A) A high-resolution TEM (HR TEM) cross-section image of a QD. Mn diffuses into the Si substrate, which is shown directly underneath QD. (B) The EELS composition mapping of Mn distribution. (C) The corresponding SAED pattern of QD, revealing a single-crystalline structure. (D) An EDS composition spectrum showing that both Mn and Ge are present QD. (E) An enlarged HR TEM image to show the detailed lattice structure of QD [2].

EDX analysis done over many QDs revealed a Mn:Ge atomic ratio of about 0.144 : 1. Since approximately 1/3 volume fraction of Mn was distributed in QD’s, they estimated an average Mn concentration of 4.8 ± 0.5% in the QD’s – we infer from this that they believed their EDX probe could not distinguish between Mn in the Ge vs. Mn in the Si.

UCLA observed remarkably robust ferromagnetism, as shown in Figure 1-3. SQUID magnetometry showed hysteresis loops from 5 K to 400 K with a maximum coercivity of 170 Oe at 5 K, $T_c > 400$ K and an M_{sat} of 1.8 μ_B. Given the extremely small amounts of Mn present, their data in Figure 1-3 are amazingly “quiet”. Using the known Mn moment, they estimated that 60% of the Mn atoms were active. Performing room temperature MFM of the QD’s, they reported that each QD was a single domain particle and ruled out the possibility of Mn_5Ge_3 and $Mn_{11}Ge_8$ ferromagnetic phases in the film. They attributed the above room temperature ferromagnetism to hole mediation in the QD’s. However, they are not able to rule out the possibility of Mn aggregation which may enhance the T_c.

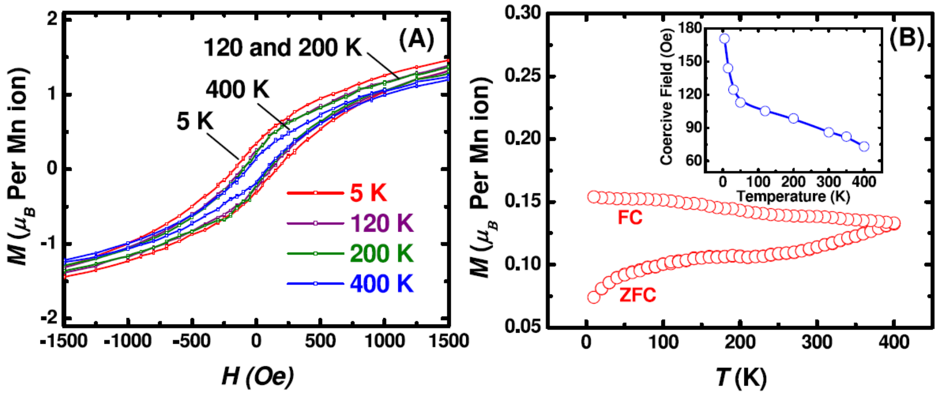

Figure 1-3. Magnetic properties of the $Mn_{0.05}Ge_{0.95}$ QDs grown on a p-type Si substrate at 450 ˚C. (A) Hysteresis loops measured at different temperatures from 5 to 400 K. The observation of a hysteresis loop at 400 K indicates a strong ferromagnetism above room temperature; (B) Zero field cooled and field cooled magnetizations of QDs with a magnetic field of 100 Oe; the inset shows the coercivity values at different temperatures [2].

As will be discussed throughout this dissertation, we attempt to reproduce this work and provide better understanding of the Ge:Mn self-assembly process. We will provide a much more detailed view of how Mn incorporation evolves with growth conditions. But we will also show that magnetic response obtained by Xiu, et al., cannot be reproduced.

To gain further insight into the growth process and a better understanding of the magnetic properties, we investigate here the influence of Mn concentration on morphological evolution and magnetism of heteroepitaxial $Ge_{1-x}Mn_x$ QD's grown by molecular beam $Ge_{1-x}Mn_x$ films. We show that Mn has a marginal affect on the QD morphology, but secondary phase formation is observed at higher Mn contents. For the Mn contents explored here, only low temperature ferromagnetism is found, despite employing growth conditions nominally very similar to those shown previously to provide for much higher Curie temperatures [14].

1.2.4 Origin of magnetism in group IV DMS

It is vital to establish the origin of magnetism in DMS research in order to discern the intrinsic magnetism from clustering or possible of film contamination. The ferromagnetic interaction in group IV DMS is hole mediated where the magnetic impurity's spin interacts with the holes to provide coupling that drives ordering [17]. Even though this idea is widely accepted, the magnetism mechanism varies depending on the magnetic semiconductor host material, the doping level, and the inhomogeneitities in the system (related to the growth process).

The origin of FM in Ge_xMn_{1-x} has been described using models such as the Ruderman-Kittel-Kasuya-Yoshinda (RKKY) interaction model [66], [67], a mean-field Zener model proposed by Dietl et al. [68], [69], and a theory involving percolation of bound magnetic polarons [70]. *Ab initio* calculations have also been employed to examine coupling [71]. To date, the model that has been most widely invoked to interpret experimental results is the bound magnetic polaron (BMP) model. This approach suggests that the localized carrier density is highly inhomogeneous and concomitantly results into an inhomogeneous exchange interaction [72]. Exchange interaction of localized holes with magnetic impurities forms bound magnetic polarons consisting of a large number of magnetic impurities around the localized hole as illustrated in Figure 1-4 below. As the temperature of the DMS material is lowered, a first FM transition associated with T_c*occurs in finite-size regions with higher local impurity concentration (impurity clustering). A further reduction in temperature perpetuates the growth and merging of BMPs between these regions until ferromagnetic alignment promulgates across the whole material. This is the second FM transition corresponding to T_c.

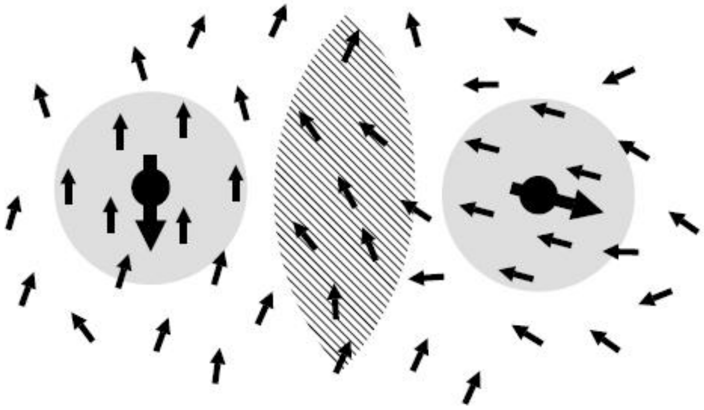

Figure 1-4 Illustration of the interaction of two bound polarons (gray circles) with magnetic impurity and hole spins, shown with small and large arrows, respectively. The black circles represent localized holes. The hatched region represents magnetic impurities that feel weak exchange interactions from both neighboring polarons [73].

All these models assume that the ferromagnetism in group IV DMS's is hole mediated through exchange coupling and increases with increase in transition metal (TM) dopant concentration. Among the 3d TMs (, Fe, Mn, Ni, Cr, V, Co etc), Mn is favored because of its high magnetic moment, high substitutional doping over interstitial doping and less clustering compared to the others [7]. When doped in a Ge host, Mn (antiferromagnetic in bulk) experiences a *p-d* hybridization between the 3d^5 Mn orbitals and the 4p^2 Ge orbitals as illustrated in Figure 1-5.

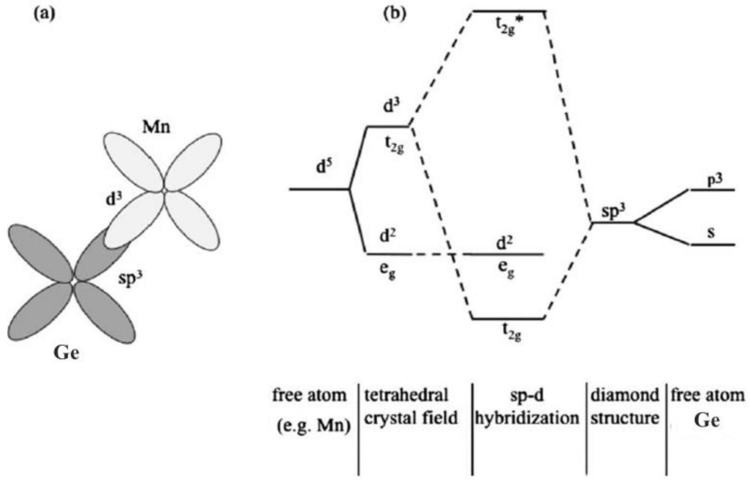

Figure 1-5. (a) Schematic of *p-d* hybridization between the Mn d orbitals and the Ge p orbitals; (b) Illustration of the crystal field and hybridization effect [74].

The moment per Mn in a DMS was determined from first principle study by Shaughnessy et al., who show that Mn atoms can occupy either a substitutional (S) and a tetrahedral interstitial (I) sites when embedded in a group IV semiconductor matrix such as Ge and Si [74]. Using a 8 – 216 atoms cell model, they show that there are *p-d* hybridized bonds between Mn and its nearest neighbor Si atom ONLY in the S site since Si bonds in the I sites are already saturated as shown in Figure 1-6. The I site consistently has lower energy of formation than the S site. The difference is, in general, about 0.500 eV. Comparing Fe to Mn, the latter was shown to have a higher M_{sat}/μ_B of the TEM in both S and I sites. The model predicts the moments for Mn to be 3 μ_B/Mn. Larger moments up to 5 μ_B/Mn observed for 0.1 at. % Mn [75] were reported to be a consequence of the weakened *p-d* hybridization between the Mn and one of its nearest neighbor Si atoms, resulting from the introduction of the second-neighbor interstitial Si [76] .

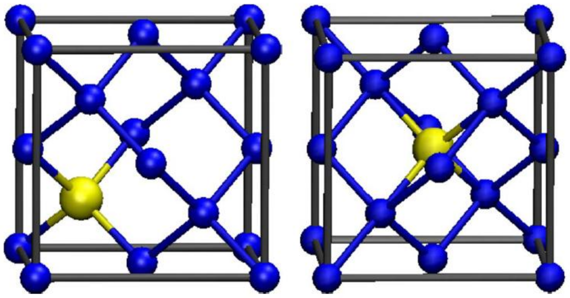

Figure 1-6. Left: 8-atom Si unit cell with Si atoms in blue and showing a Mn atom (yellow) at an S site. Right: 8-atom cell with Mn at the I site [74].

Hole-mediated ferromagnetic ordering opens up the possibility to control magnetic properties simply by changing the carrier density with a gate voltage, a distinct advantage for high speed, low power devices. DMSs are further interesting because their multi-component nature in principle allows the semiconducting and magnetic properties of these alloys to be tuned over a wide range by adjusting the composition [77].

$Ge_{1-x}Mn_x$ films have been reported to exhibit ferromagnetism, superparamagnetism, paramagnetism, and a spin- glass state [78], or a combination of these magnetic phases. A spin glass is a frustrated magnetic state where the spins are randomly aligned with conflicting ferromagnetic and antiferromagnetic interactions. As you cool a spin glass toward it T_c in a magnetic field, its moment increases following Curie law. It changes it magnetization below T_c. Spin glasses differ from ferromagnetic materials by the fact that after removal of the external magnetic field, ferromagnetic remain magnetized indefinitely at the its magnetic remanence (M_r). Paramagnetic materials differ from spin glasses by the fact that, after removal of the external magnetic field, the magnetization rapidly falls to zero, with no remanence.

1.3 Epitaxial Ge/Si (001) Quantum Dots

The heteroepitaxial self-assembly of coherently strained Ge islands on Si (001) oriented substrates has been extensively studied starting two decades ago [79–86]. The lattice parameter, **a**, of Ge is 4% larger than that of Si. This resultant lattice mismatch drives the formation of islands as a pathway to relaxation of the film cohesive strain (ε_{coh}) ,and subsequent transitions from one island shape to another [80], [87], [88]. For Ge/Si(001), ε_{coh} = -4.2%.

$$\varepsilon_{coh} = \frac{a_{film-}\ a_{substrate}}{a_{substrate}} \qquad 1\text{-}1$$

These islands allow local expansion of the lattice parameter at unconstrained surfaces and therefore provide a means of relaxation of the film [89]. Island formation precedes dislocation introduction in the system. The growth mode for heteroepitaxial self-assembled Ge/Si (001) system is a classic Stranski-Krastanov (SK) process. By virtue of its lower surface energy, Ge initially wets the Si and grows in a layer-by-layer fashion to a kinetically determined [90] 2D wetting layer (WL) thickness of three monolayers. This is followed by formation of 3D islands above the WL. Island formation precedes the formation of misfit dislocation [79], [91].

There is a competition between the surface free energy reduction and the increase in strain energy due to addition of the Ge layers. When the island volume exceeds a critical volume V_c, subsequent adatoms will form 3D islands since the free energy of Ge is reduced by forming coherent clusters. The critical volume can be obtained by minimizing the change in total free energy of the system $E_{tot} = E_s + E_r$ where E_s is the increase in surface free energy associated with nucleation of island and E_r is the elastic relaxation energy, given by:

$$E_{tot}\ V\ \ = 4\Gamma V^{\frac{2}{3}}\, tan^{\frac{1}{3}}\theta - 3V\frac{\varepsilon^{2}\ 1-\nu}{\pi\mu}\ tan\theta \tag{1-2}$$

where **Γ** =γ_f cscθ - γ_s cotθ, V is the island volume, θ the contact angle between the island and the facets and the planer surface, σ the misfit stress, μ the shear modulus, ν the Poisson’s ratio, γ_f and γ_s being the surface energy free energy per unit area for the facet and the normal orientation respectively of a “hut” having a square-based pyramidal shape with height h, base l, and contact angle θ [79], [85].

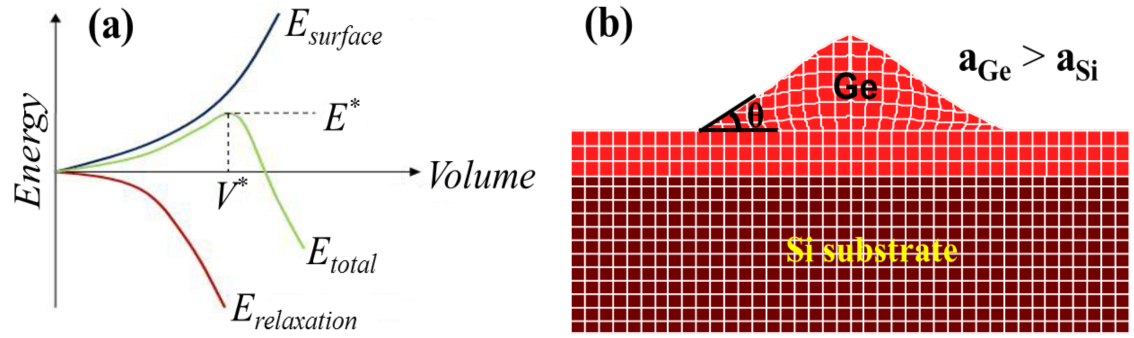

Figure 1-7. (a) Energy change associated with the nucleation of islands as a function of island volume; (b) sketch of QD strain driven self-assembly process following the SK mode of growth where the 1st 3ML are pseudomorphically strained and grow layer by layer followed by a 3D growth of islands.

Because of the energy barrier E_c involved in the nucleation of islands, we expect that the nucleation rate, R_s to be:

$$R_s \sim De^{\frac{E_c}{k_B T}} \tag{1-3}$$

where D is the surface diffusion constant. In this view, the critical nucleation volume of islands scales as ε^{-6}, where ε is the lattice mismatch strain, hence island size can be reduced by using larger strains (i.e., going to pure Ge on Si). The critical volume, V_c is obtained by maximizing Eqn. 1-2 with respect to volume yielding:

$$V_c = \frac{8\Gamma\, tan^{1/3}\, \pi\mu}{\varepsilon^2 \;\; 1-\nu \;\;\; tan\theta}^{\;1/3} \qquad \text{1-4}$$

The length scale associated with strain-driven islanding is proportional to

$$L \propto \frac{\Delta\Gamma}{M\varepsilon_{coh}^2} \qquad \text{1-5}$$

where $\Delta\Gamma$ is the change in surface energy, M is an elastic modulus, and ε_{coh} is the lattice mismatch strain.

The size, density and shape of strained islands depend on kinetic aspects, including substrate temperature of (T_s), amount of material deposited and deposition rate. Elevated substrate temperatures are required to provide adatom diffusion lengths that are the same order as the intrinsic length scales for islanding set by the mismatch strain. In the Ge_xSi_{1-x} system, island morphological evolution is well-established. After the wetting layer, the first islands to form are huts [81] and square-based pyramids (or rectangular-based huts at lower temperatures**)** [92]. These islands are bound by {105} facets tilted by 11.3˚ to (001) as shown in Figure 1-8.

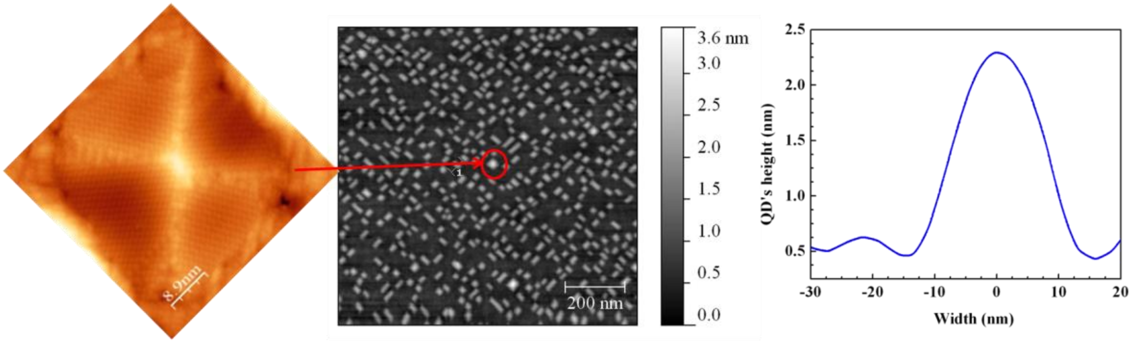

Figure 1-8. Center: AFM images of 6 ML Ge/Si (001) QD's grown at T_g = 550 ˚C showing an array of square and elongated huts (along Si [001] and [010]. Inset: an STM image of a typical Ge hut bound by four {105} facets [93]; Left: Line scan of the hut marked with 1 on the left showing typical size and 11.5˚ facets.

As these islands grow and reach a critical volume, they can transform into a dome-shaped islands as shown in Figure 1-9. Dome islands relieve more strain than the pyramid due to favorable energetics and features four (113), (102) and steeper {15 3 23} [88] facets that form angles of 25.2°, 26° and 33° respectively with the (001) substrate plane.

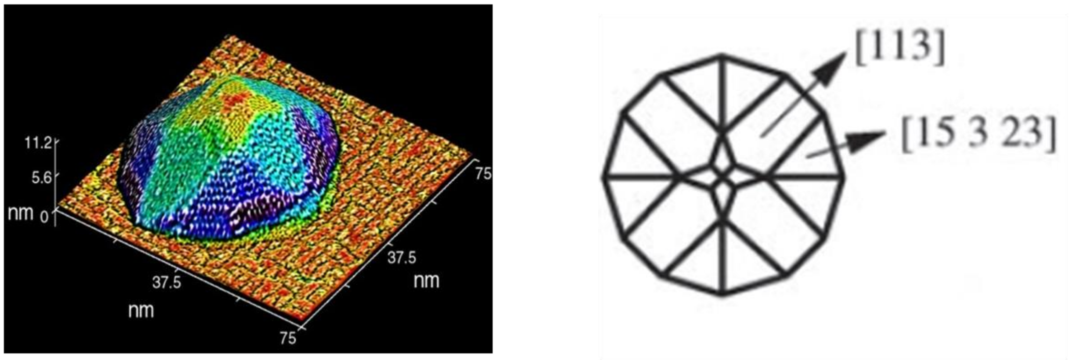

Figure 1-9. STM image of a multifaceted dome [80] and a schematic showing the facets of a dome.

Pyramids and domes are coherently strained, meaning that they are dislocation free. Further growth may result into **superdomes,** which are dislocated domes [94]. These *dislocated* domes can have similar facets to coherent domes but much larger sizes due to their reduced elastic energy.

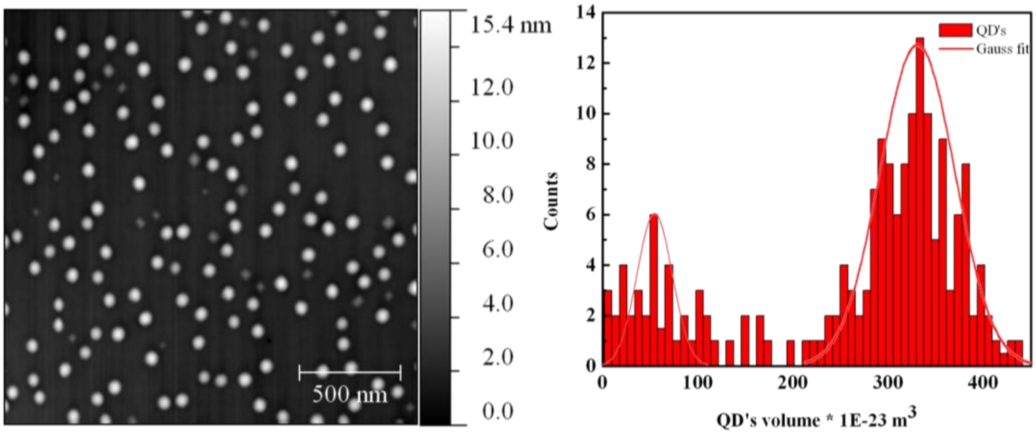

Figure 1-10. Left: AFM image of 6 ML Ge/Si (001) grown at T_g = 600 ˚C showing a dense array of huts domes; Right: Statistical volume distribution of the island. Gaussian peaks are used to fit

the distribution data. This is a bimodal growth distribution typical of nucleation and growth via Oswald ripening.

The presence of different island types leads to bi- or tri-modal distributions as shown in Figure 1-10 and by Ross et al. [95] and Medeiros – Ribeiro et al. [80] . Each distribution peak corresponds to a energy optimum island size.

Figure 1-11 shows a process phase space for MBE grown Ge_xSi_{1-x} / Si (001) alloys with x = 0.3 by Floro et al. [96]. This phase space covers the evolution of quantum dots in both the near equilibrium regime (high growth temperatures [T_s] and low deposition rates [R_{dep}]) and the kinetically limited growth regime (low T_s hence low surface diffusivities, and high R_{dep}). It serves as a useful tool in mapping out island specific growth conditions.

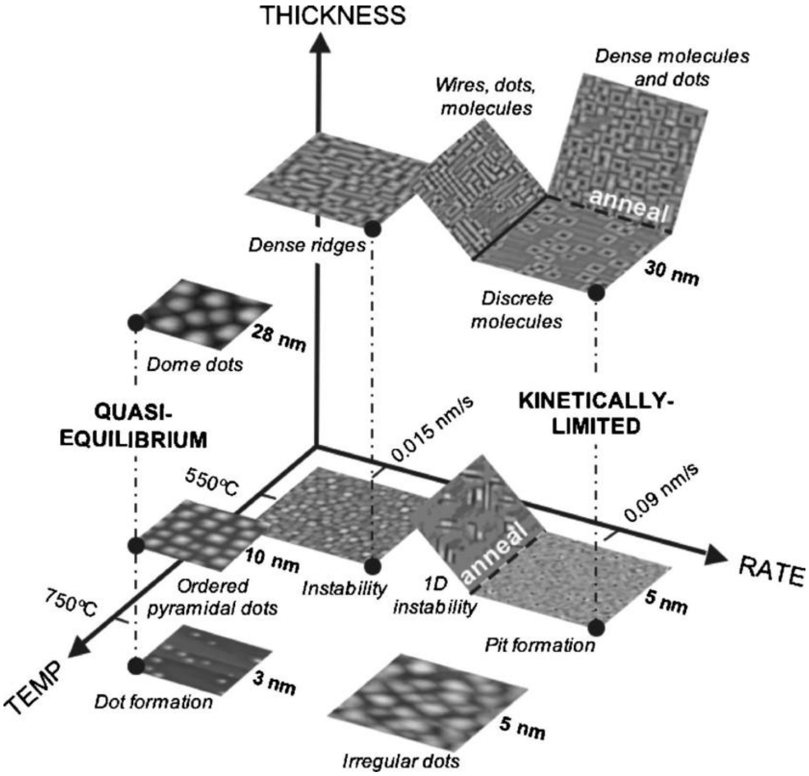

Figure 1-11: The process phase space for strained-induced morphological evolution during Ge_xSi_{1-x} / Si (001) alloys with x = 0.3 MBE growth [96].

It has been shown that while most of the Ge atoms stay on the surface of Si (001) at room temperature, inter-diffusion can occur during deposition at elevated temperature [97]. Minimal intermixing has been achieved at temperatures below 550 ˚C.

The relatively high temperatures required for quantum dot self-assembly would seem to be completely antithetical to metastable Mn incorporation in a solution phase. Nonetheless, using our hyper-thermal molecular beam epitaxy (HT-MBE) system, we seek to study formation of self-assembled Mn_xGe_{1-x} metastable quantum dots using the diverse growth parameter space provided by molecular beam epitaxy. We have to pursue and establish far-from-equilibrium growth conditions to control metastable Mn incorporation and magnetism, as well as to fine-tune the QD shape, dimensions, and population density. It is the goal of my dissertation to explore, control and exploit Mn_xGe_{1-x} quantum dot growth dynamics, and to assess their impact on the resulting magnetic behavior. If they can be synthesized, Ge:Mn quantum dots may provide superior magnetic properties to Mn_xGe_{1-x} films due to quantum confinement effects. In addition, the synthesis of magnetic Mn_xGe_{1-x} QD’s using templating techniques [98] allows precision in their spatial localization and size distribution which can be used in spintronic devices such as logic switch. Ferromagnetism persisting up to room temperature would be desirable for this system for practical applications.

Chapter 2: Characterization technique and Experimental

2.1 Introduction

The following techniques used in this research are reported here (in order): Reflection high energy electron diffraction (RHEED) , atomic force microscopy (AFM), transmission electron microscopy (TEM), energy dispersive x-ray (EDX) analysis, and magnetic measurements using superconducting quantum interference device (SQUID) magnetometry, and vibrating sample magnetometry (VSM).

2.2 Reflection high energy electron diffraction

RHEED is an in situ technique used for real–time characterization of epitaxial growth and crystalline surfaces. We are able to employ this technique to monitor our Si substrate surface and consequently our films during epitaxial growth. An electron beam of 22 to 25 keV is directed towards the sample at a grazing incidence angle, typically 1 to 2˚, to ensure that the high energy electrons interact only with the crystal near surface region, due to very small penetration depths of order 10 nm.

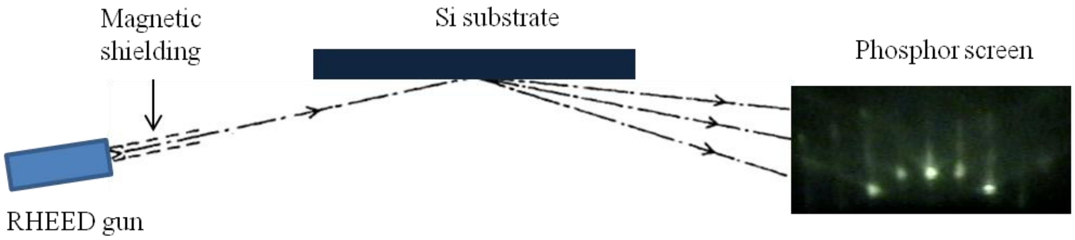

Figure 2-1: Schematic of the RHEED setup in the MBE chamber showing a RHEED pattern recorded from a Si (001) (2x1) surface in the [110] azimuth showing an atomically smooth 2-dimensional surface.

Figure 2-1 shows a schematic of the RHEED implementation in our MBE system where an electron beam produced by an electron gun is incident to our sample mounted on a manipulator. The forward scattered electrons strike the phosphor screen. Electrons that happen to pass through nanoscale raised surface features can result in bulk-like diffraction patterns. RHEED provides a large scattering cross section for the forward scattered electrons resulting to a very large Ewald sphere. The intersection of the Ewald sphere and the diffracted beam (reciprocal lattice rods) occur at some height resulting in a spotty diffraction pattern. The diffraction pattern is viewed from a front view port using a front-viewing non coated phosphor screens due to the geometry of the existing view ports in the MBE system. The diffraction pattern is captured via a charge coupled device (CCD) camera and recorded on DVD storage media.

To minimize the effect of stray magnetic fields emanating from the sputter guns, the incident RHEED electron beam path is covered with CO-NETIC magnetic shielding. Moreover, the RHEED electron gun is differentially pumped as illustrated in Figure 2-2 to allow routine operation at higher pressure without arching and reducing the cathode life time.

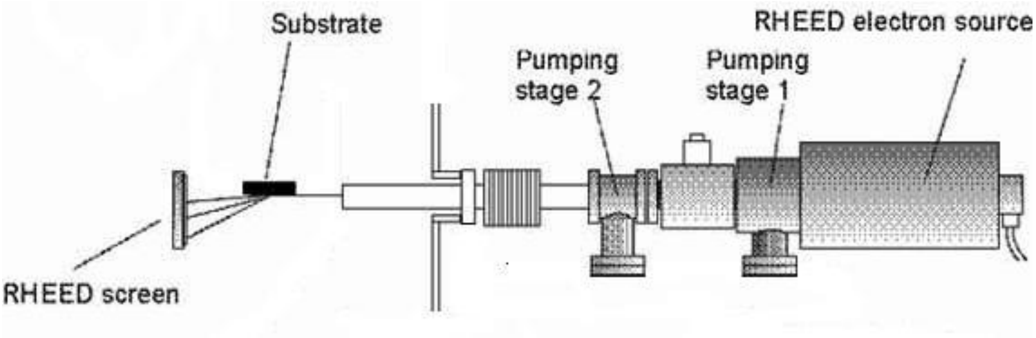

Figure 2-2: Schematic of RHEED setup illustrated the double differential pumping system utilized in the MBE chamber [Image taken from Staib instruments manual].

RHEED patterns are recorded in the Si <110> zone axis. Figure 2-3 shows typical patterns during Ge QD’s growth on Si (001) substrate.

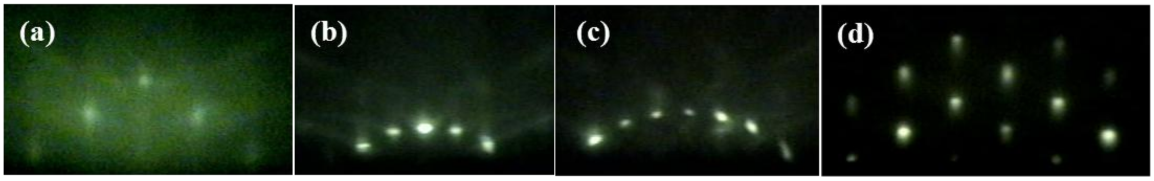

Figure 2-3. Typical RHEED patterns during Ge/Si (001) sample processing in the MBE in the Si <110> azimuth. (a) diffuse 2D (1x1) pattern due to SiO_2 on surface of the Si wafer; (b) first and (c) second order Laue spots indicating a (2x1) surface reconstruction of Si after native oxide desorption at T_s = 800 °C. This 2D pattern is reminiscent of an atomically smooth 2-dimensional surface; (d) atomically rough 3D pattern resulting from transmitted diffraction through Ge quantum dots.

2.3 Atomic force microscopy

AFM was the primary *ex situ* surface analysis technique used for post-growth analysis. This technique allows topographical measurement of all surface nanostructures including quantum dots, secondary phases, pits, and contamination. Unless otherwise stated, an NT-MDT Solver Pro microscope (Figure 2-4) was employed.

Figure 2-4: Image of a NT-MDT Solver Pro –M AFM fitted with a Smena head.

This instrument is equipped with two scan-heads; universal and smena for scanning by sample and scanning by tip methods respectively. The maximum scan area obtainable using the universal head is a 13 μm x 13 μm scan area. The Smena head boasts of a much larger scanning range, 100 μm x 100 μm, in addition to closed loop positioning for precise tip placement.

Topography measurement techniques

Topographic imaging with AFM is accomplished via contact, semi-contact (tapping) or non-contact modes. Figure 2-5 shows surface forces as they relate to the probe – sample separation distance for the three scan modes.

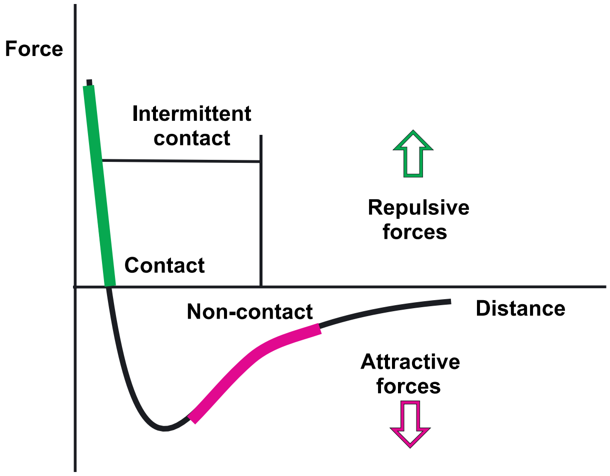

Figure 2-5: Schematic diagram of surface forces as they relate to the probe – sample separation distance for different scan modes [99].

In **contact mode**, the tip located at the end of a cantilever scans the sample in contact with the surface. The force on the tip is repulsive with a mean value of 10^{-9} N. This force is set by pushing the cantilever against the sample surface with a piezoelectric positioning element. In this mode, the deflection of the cantilever is sensed and compared in a DC feedback amplifier to some desired value of deflection. Since we are scanning in ambient atmosphere, contact mode is limited due to excessive tracking forces on the tip when in contact with the surface. This results into undesired noise levels in the topography images.

Non-contact mode is used in applications where the tip damage reduction is paramount. In this mode the tip hovers 50 - 150 Angstrom (Å) above the sample surface. Attractive Van der Waals forces acting between the tip and the sample are detected, and topographic images are constructed by scanning the tip above the surface. Unfortunately the attractive forces from the sample are substantially weaker than the forces used by contact mode. Therefore the tip must be given a small oscillation so that AC detection methods can be used to detect the small forces between the tip and the sample by measuring the change in amplitude, phase, or frequency of the oscillating cantilever in response to force gradients from the sample.

Tapping mode, also known as semi-contact mode, was the scanning technique of choice in this work. In this mode, the tip located at the end of a cantilever is oscillated at its resonant frequency. The tip's average position is in the attractive region of Figure 2-5. When fully extended, the tip touches the surface atoms of the sample and repelled back due to its inter – atomic interaction forces. This intermittent contact with the sample surface is what is referred to as *tapping*. This interaction with the surface causes a reduction in the oscillation amplitude. A piezoelectric drive adjusts the tip height of the tip by raising it away from the sample in order to re-attain the previous oscillation amplitude. In this way, the tip can be rastered across the sample and the magnitude of this feedback loop can thus be used to determine the topography. Tapping mode overcomes problems associated with friction, adhesion and electrostatic forces. Unless noted otherwise, the AFM scans in this thesis were taken in tapping mode.

Phase measurement techniques

Phase imaging is a powerful extension of tapping mode AFM that provides nanometer-scale information about surface structure often not revealed by other AFM techniques. By mapping the phase of the cantilever oscillation during the tapping mode scan, phase imaging goes beyond simple topographical mapping to detect variations in composition, adhesion, friction, viscoelasticity, and perhaps other properties. Since the tip contact area is directly related to the surface slope, phase imaging is great in highlighting island facets. Figure 2-6 shows an example of a typical tapping mode AFM scan of a Si/Si (001) impurity-generated dots grown at high Ar pressure showing both the topography and phase scans. All pyramids have a distinct boundary due to the transition from scanning the (001) to faceted surfaces. Phase images of islands exhibit the greatest contrast due to owing to their inherent change in surface slope.

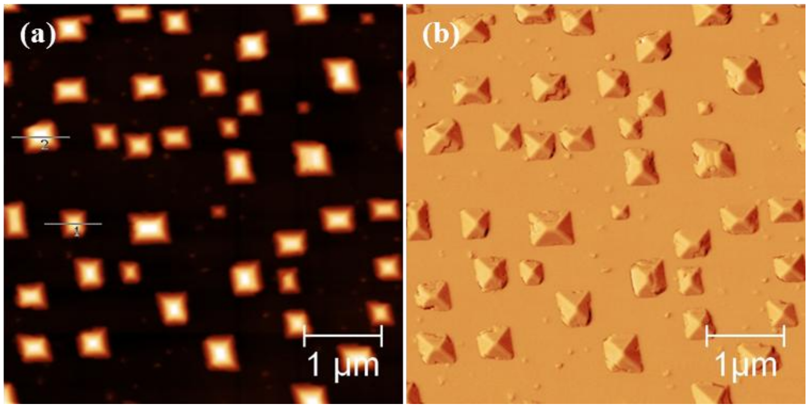

Figure 2-6. 25µm^{2}AFM scans of Si islands on Si (001) scanned along the [110] azimuth. (a) topography image; (b) corresponding phase contrast image.

2.4 Transmission electron microscopy

The structural properties of $Ge_{1-x}Mn_x$ QD's grown by molecular beam $Ge_{1-x}Mn_x$ films grown (Ge,Mn) films was studied using TEM. For this dissertation, two microscopes were extensively used: JEOL 2000FX operated at 200 kV with a LaB_6 filament, and Titan 80-300 operated at 300 kV with a W- field emission filament.

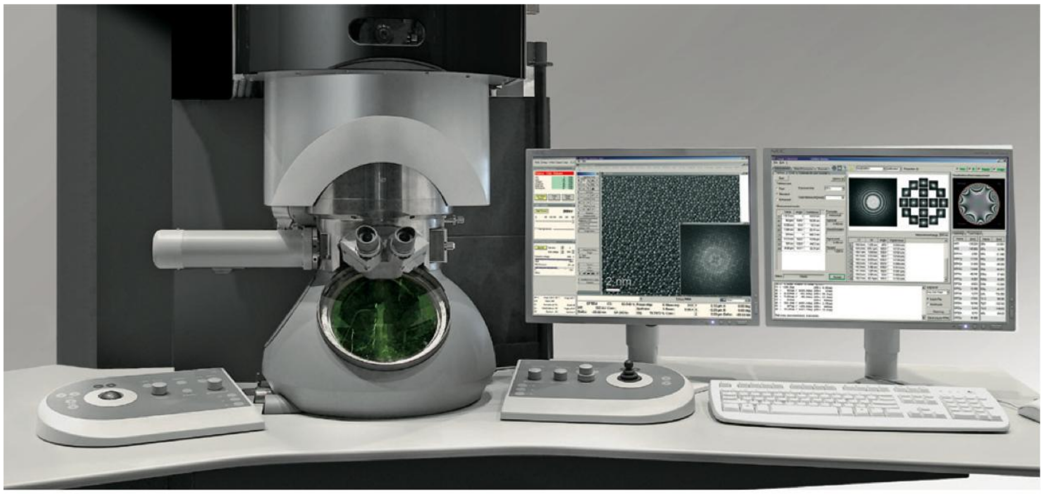

Figure 2-7: Picture of the Titan 80-300 equipped with HAADF detector, Gatan Orius cameras, Gatan energy filter series and a Si (Li) EDS detector with solid angle of 0.13 srad.

A beam of high energy electrons 80 – 300 kV is transmitted through an electron transparent ultra-thin specimen (50 - 100 nm), interacting with the specimen as it passes through it. Sample preparation techniques for both plan view and cross section are described in details in the Appendix 2.

An image is formed from the interaction and is magnified and focused onto a fluorescent screen and a CCD camera. Owing to the small de Broglie wavelength of electrons ($\lambda = h/p$). TEM is capable of imaging at a significantly higher resolution than standard optical microscopes even to single column of atoms, also known as High-resolution transmission electron microscopy (HRTEM).

When using high-resolution imaging techniques and large accelerating voltages, the possibility of specimen beam damage is greatly increased. Any electron that penetrates the specimen with an energy greater than the atomic cohesive energy, is capable breaking bonds and shifting atomic positions. With increased magnification, the electron fluence for a given area greatly increases, thus increasing the number of broken bonds and rate of atomic displacement. The extent of specimen damage will depend on the specimen thickness and the strength (and deformation mechanisms) of the material under investigation [100]. Damage may be worse in films that are already defective or dislocated.

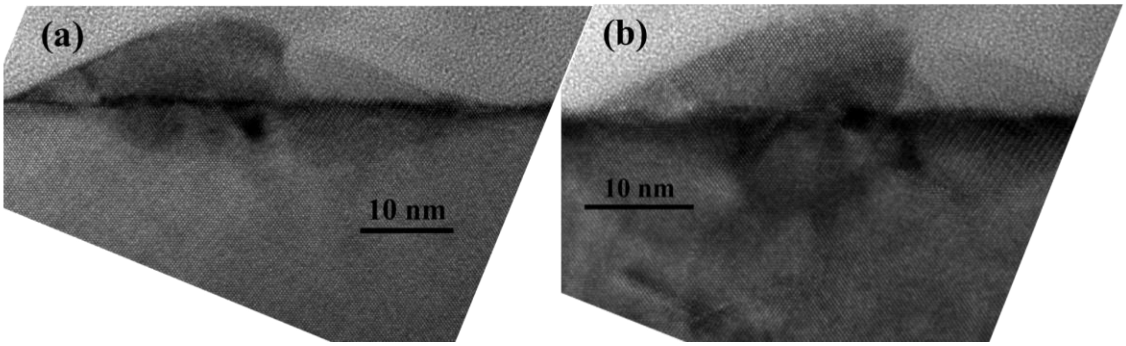

Figure 2-8. BF TEM micrographs taken illustrating the effect of the 300 kV on the specimen after extended dwell time. (a) Before and (b) After beam induced damage, {113} defects are observed in the specimen.

Energy Dispersive X-ray Microanalysis (EDX)

EDX spectroscopy coupled with TEM can provide elemental analysis on areas as small as nanometers in diameter. The interaction of the electron beam with energy E_0 with an inner shell electron e.g. K shell, may result in ejection of the electron. The hole in the K shell is subsequently filled by an outer shell electron, e.g., from the L3 shell. The excess energy associated with the electronic transition is emitted as a characteristic X-ray quantum as illustrated in Figure 2-9. EDX can be used to determine the elemental composition of individual points or to map out the lateral distribution of elements from the imaged area.

The spatial resolution is determined by the probe size, beam broadening within the specimen, and the effect of backscattered electrons on the specimen around the point of analysis. Thin specimens, a few hundred angstroms thick, in which self- absorption and fluorescence of the emitted x-rays are minimized, are needed for accurate quantitative analysis. The specimen is oriented in the sample holder such that the thin portion of the wedge faces the detector to minimize X-ray absorption. Characteristic x-rays are generated deeper in the specimen and the x-ray generation volume is larger as E_0 increases, also known as the x ray absorption effect.

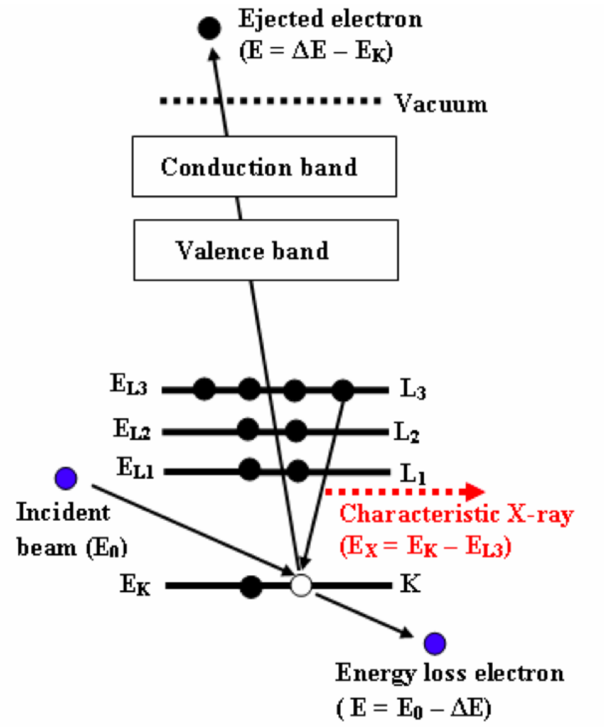

Figure 2-9: Schematic of X-ray production in EDX.

Qualitative analysis involves the identification of the elements present and is a prerequisite for quantitative analysis. The TEM imaging & analysis program (TIA) automatic qualitative analysis capabilities are quite good when the system is properly calibrated with standards (peaks within 10 eV of their actual energies). The program does background subtraction and peak deconvolution, and then applies an intelligent method of identification within constraints set by the operator. However, the operator should use his/her knowledge of chemical principles and of the specimen to manually check the results.

Only peaks which are statistically significant should be considered for identification. The minimum size of the peak should be 3 times the standard deviation of the background at the peak position. It is recommended to use high count rate or keep the dead time below 30 % to generate significant peaks.

To determine the x-ray intensity ratios (k value), use the specimen intensity I_i and the standard intensity $I_{(i)}$ for each element present in the sample. The measured intensity ratios should be equivalent to the ratios of mass or weight fractions giving the k value:

$$\frac{I_i}{I_{(i)}} = \frac{C_i}{C_{(i)}} = k \qquad \text{2-1}$$

In standardless quantitative analysis (what TIA terms “without standards”), the intensity that forms the denominator of the k ratio, I(i) , is provided by calculation rather than direct measurement. Typically the standards are derived from a suite of experimental standards measurements (a standards data base) performed by the manufacturer and subsequently adjusted for the characteristics of the local instrument. TIA automatically corrects the intensity for a host of matrix effects (ZAF); Z - atomic number effects (backscattered coefficient and stopping power), A - absorption effect (largest effect and occurs when x-rays are absorbed by atoms giving up Auger electrons), F - X- ray fluorescence effect (characteristic X –ray resulting from X –ray absorption by sample atoms). TIA does these corrections by fitting a phi-rho-z curve to the experimental data.

This is an ionization distribution in which ionizations, φ(ρz), are plotted against mass-depth (ρz)).

The EDX has a Mn detection limit of about 1.5 at.%. This takes account of the acquisition time, accelerating voltage and the line used to measure the element and in our case. It is calculated as three times the square root of the background at full width at half maximum intensity (FWHM) of the peak. Hence we have to have to have more than 1.5 at.% Mn to distinguish it from the noise level.

High angle annular dark field

HAADF is a Z-contrast imaging technique. Using this method, incoherent elastically scattered electrons are collected on an annular detector at high angles (typically 75-150 mrad). Incoherent electrons do not carry phase information so they cannot constructively (or destructively) interfere; thus the total intensity is the sum of each individual scattered electron.

HAADF is performed with a focused scanning electron probe and the image contrast mechanism is simply the total collected intensity at the annular detector during beam raster. Since specimen information is mapped to real space using select scattered electrons, HAADF is appropriately a dark-field technique.

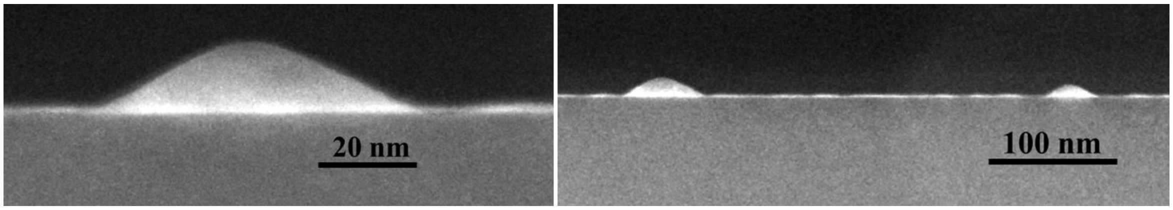

Figure 2-10: Example of HAADF –STEM images of Ge QD’s. In the HAADF micrograph, Ge having a greater Z than Si appears as the lighter intensity due to increased high angle scattering.

Higher-Z atoms have a greater scattering cross section, and generate greater scattering angles. Figure 2-10 shows an example of HAADF image. Brighter regions represent areas with increased Ge content, owing to its larger Z than Si or C. For atomic resolution and quantitative Z-contrast imaged, the specimen thickness must be less than 50 nm.

2.5 Magnetometry

Magnetic measurements were performed using a SQUID magnetometer at CEA/INAC in Grenoble by out collaborator, Matthieu Jamet. Additional magnetometry was conducted using a Quantum Design Physical Property Measurement System (PPMS) vibrating sample magnetometer (VSM) Model P525 owned by Prof. Wolf's group. However, comparison with the SQUID results indicates that the VSM data obtained earlier were insufficiently sensitive, and likely subject to parasitic signals that could not be removed without significant additional work. Hence, SQUID measurements, although quite limited, will be focused on in this work.

In all samples, the measurements were made with the external field oriented parallel to the sample surface. Careful handling of the samples from the MBE to the magnetometers was taken using non-magnetic tools to prevent any magnetic contamination. Specifically, samples were handled using nonmagnetic ceramic tweezers; all mounting and containment materials were non-magnetic. The samples were mounted on the quartz sample holder using GE7031 vanish and/or using Crystalbond 509. M(H) curves, M(T) and M_r(T) were measured with a in-plane external field.

The total magnetic signal is a sum of the diamagnetic signal from the Si substrate, any parasitic magnetic phases due to inherent magnetic contamination in the Si substrates, and the signal of interest from Mn atoms, which can be contained in multiple different magnetic phases. In order to obtain the magnetization curves due to the Mn deposited, we remove a line of negative slope representing the diamagnetic susceptibility of the Si substrate. Moreover, we remove a parasitic paramagnetic signal due to the Si substrate at low temperatures. These two subtractions techniques will be discussed further in chapter 3.

Data Treatment: Considering that our films contain only 1 – 4.7x10^{14} Mn/cm^2, which is less than that of a single atomic layer (when referenced to the Si (001) planar density), the expected maximum signal strength from the Mn (assuming at most 5 μ_B/Mn) is 1–4.5x10^{-6} emu. On the other hand, the Si substrate, which is about 260 μm thick, provides a diamagnetic signal of 1.5 x10^{-4} emu, up to 100 times larger than the Mn signal. Furthermore, as shown later, the Si substrate does seem to contain some spurious parasitic moments, which while small, still provides a larger signal than the Mn in our films. Hence, subtraction of the relatively large signals from the substrate is critical and extremely sensitive step, in analysis of the SQUID data.

In order to separate the magnetic contribution of different phases in (Ge,Mn) films, the Brillouin function [101] is used to subtract the paramagnetic component. This function describes the dependence of magnetization (M) to an applied field (B) and temperature in ideal paramagnets. The Brillouin function is defined by:

$$B_J\ x\ = \frac{2J+1}{2J}\coth\ \frac{2J+1}{2J}\,x\ - \frac{1}{2J}\coth\ \frac{1}{2J}\,x \tag{2-2}$$

In classical limit where B/T << 1, J → ∞, the Brillouin function reduces to the Langevin function:

$$M\ \ x\ \ = M_S\ \ \coth\ x\ \ - \frac{1}{x} \qquad \text{2-3}$$

M_s is the saturation moment per magnetic cluster

The magnetization is defined by:

$$M_s\,(x) = n\mu_H B_J(x) \qquad \text{2-4}$$

$$x = \frac{gJ\mu_B B_J}{k_B T} \qquad \text{2-5}$$

n is the number of atoms per volume

$\mu_{H=}\, gJ\mu_B$ is the average magnetic moment of the paramagnetic element

g is the Landé g-factor

μ_B is the Bohr magneton

where $\mu_0\, H$ is the applied magnetic field.

2.6 Experimental Methods

Molecular Beam Epitaxy

Molecular Beam Epitaxy (MBE) is one of the techniques for single crystal synthesis with a control of atoms at the monolayer scale, invented in the late 1960s at Bell Laboratories by J. R. Arthur and Alfred Y. Cho [102]. All of the growth experiments included in this dissertation were conducted in our custom, homebuilt Hyperthermal Molecular Beam Epitaxy (HyperMBE) chamber at University of Virginia (UVA) unless stated otherwise. HyperMBE is unique from other MBE systems in that it is designed to access a broad window of kinetic deposition parameters. Typical Group IV MBE utilizes thermal evaporation and/or electron beam evaporation of deposition materials. The benefit of these techniques is that operation is completely in UHV, minimizing the chances of contamination from process gasses. These evaporation techniques also have certain disadvantages including potential thermal loading of the sample, extensive outgassing, contamination of source material, and poor rate stability. Such growth techniques may be considered *thermal deposition* wherein “thermalized” atoms with low energies (e.g. ≤1 eV) are used. This holds a constraint on thin film growth such that high substrate temperatures (500-700 ºC) and slow deposition rates are required for smooth layer-by-layer film growth or to promote coherent Ge/Si(001) self-assembly of QDs.

In contrast, our MBE employs variable-distance magneton sputter guns for deposition of Ge and Si. In sputtering, Ar^+ derived from ionization of the sputtering gas, are accelerated towards the negatively charged the target material (cathode). The source material is eroded by the arriving ions via energy transfer causing the ejection of the neutral species of the source material to be ejected. These species can be individual atoms, clusters of atoms or molecules. The neutral particles travel in a straight line defined by the mean free path and deposit onto the substrate unless they collide with other particles in their trajectory path. In magneton sputtering, strong magnets are placed behind the target material to trap the free electrons in a magnetic field directly above the target surface. These electrons are not free to bombard the substrate to the same extent as with diode sputtering. At the same time the extensive, circuitous path carved by these same electrons when trapped in the magnetic field, enhances their probability of ionizing a neutral Ar gas molecule by several orders of magnitude. This increase in available Ar^+ significantly increases the deposition rate.

Energetics of deposition via magneton sputtering

An atom is ejected (sputtered) from the source material if the energy of the bombardment is greater than the surface binding energy, E_B. This is the energy required to remove an atom from the top surface layer in vacuum during the ion sputtering process. E_B of Si and Ge are 4.73 eV/atom and 4.29 eV/atom respectively [103]. In order to ignite a glow-discharge plasma an electric field is applied in the vicinity of the sputter target. By tuning the strength of the electric field, one can control Ar+ energy and hence the sputtering yield. However, the energy distribution of the ejected atoms is defined by the Thompson distribution [104] given by

$$\frac{dN(E)}{dE} = \frac{E}{E + E_b} \cos\theta \qquad \text{2-6}$$

where dN/dE is the number of particles in an energy interval dE, E is the kinetic energy, E_B is the surface binding energy and θ is the emission angle. The maximum in the energy distribution is reached at 0.5 E_B and features a long high-energy tail. The sputtered species in the tail end of the distribution, having energies far in excess of $E_{B,}$ are capable of re-sputtering material from the substrate. Fortunately, since sputtering is typically operated in a high background pressure of inert gas (1-10 mT), there is a high probability of thermalization due to vapor collisions.

The sputter guns are operated with DC power. Deposition rates can be varied between 0.05 Å/s and 6.5 Å/s depending on power and substrate-target separation, with no thermal loading on the sample. Using Transport of Ions in Matter (TRIM) modeling, we find ejected Si and Ge species to have energies in the range of 1-20 eV upon exiting the sputter target. Though the precise degree of deposition flux thermalization (process of sputtered species to reach thermal equilibrium with the surrounding through mutual interaction) during transit to the substrate in an Ar ambient has not been determined, the mean free path is plotted in Figure 2-11 as a function of pressure. The distance between the source and substrate ranges between 0.4 to 4.7 inches and the working pressure is 4.5 mT. In this work, the growths we performed with the gun positioned ~4 inches from the substrate. Considering the mean free path of the sputtered species to be ~ 1.2 inches, energetic Si and Ge atoms will undergo collisions en route, and are likely to be thermalized when they arrive at the substrate.

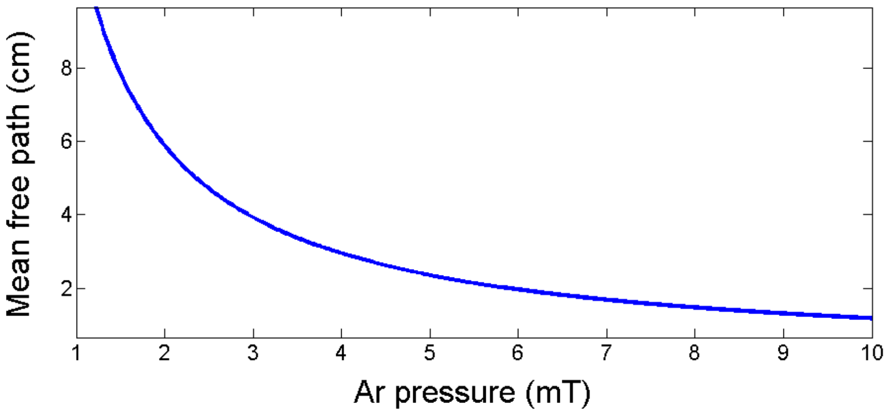

Figure 2-11: Mean free path of Argon as a function of pressure [105].

Our HyperMBE was developed to achieve necessary UHV vacuum levels for Si processing, < $5x10^{-10}$ T. To do so, the MBE is load-locked (see Figure 2-12B) using a transfer chamber that achieves 5 $x10^{-9}$ T via a single 300 L/s turbo-molecular pump. Upon transfer to position G, clean Si wafers undergo thermal treatment for carbidization, oxide desorption, and thin film deposition with control of the precise sample position via a 5-axis manipulator (F). UHV pumping on the reactor (A) includes a 600 L/s turbo-molecular pump, an ion pump at F, and dual titanium getter pumps. Finally, *in situ* real-time surface diffraction analysis is conducted via reflection high energy electron diffraction (RHEED) is conducted at glancing angle (< 4^o) with a 20 keV electron beam through a magnetically shielded aperture (Ø=1 mm). The aperture tube covers approximately ½ of the beam path and is double-differentially pumped with two small turbomolecular pumps at Figure 2-12 (H). In our particular setup, the additional precaution of shielding and differential pumping has been necessary to prevent electron scattering due to stray magnetic fields resulting from the magnetons.

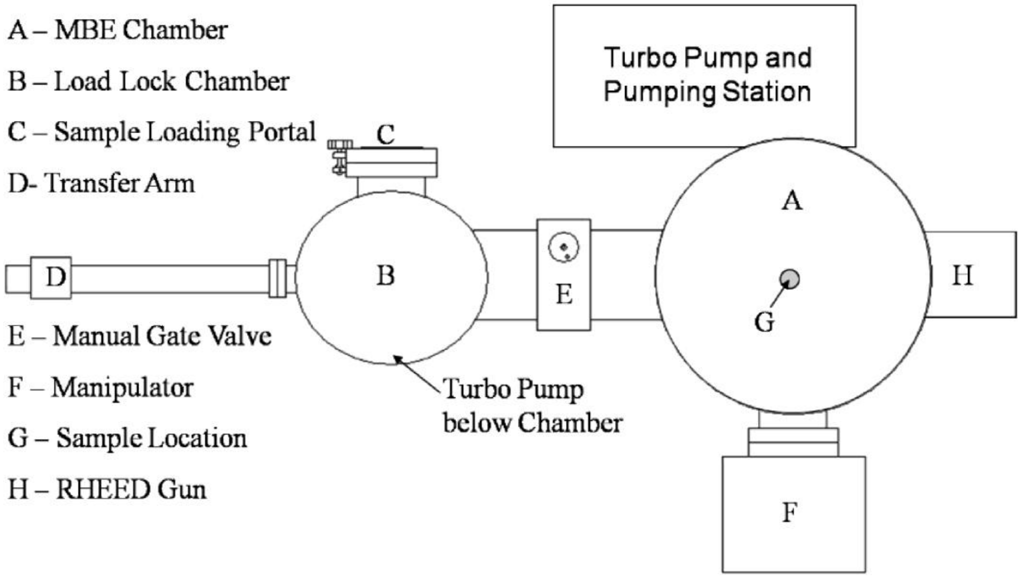

Figure 2-12: Top view of the UHV chamber showing key components for film synthesis [106].

The layout for all deposition sources is shown in Figure 2-13 below. Our main deposition species, Si and Ge, employ 2" sputter targets of 99.9999% (6N) purity. Mn was evaporated thermally using a Knudsen cell using 99.995% (4N5). Plasma ignition for magneton sputtering requires an argon pressure of ~4 mT. Ar with 99.999% (5N) purity is used. The Ar gas undergoes two purification stages, getter purification and liquid nitrogen (LN2) cold trap. These two stages are arranged in series. In the first stage, Ar from the tank is channeled through a PS2 – GC50-R-1-V Seas heated metal getter specifically designed for He and Ar purification. This getter removes O_2, H_20, CO, CO_2,

H_2, CH_4 and N_2 impurities to < 10 parts per billion (ppb). The getter alloy operates at elevated temperatures (350 to 400 ˚C) and removes impurities by forming irreversible chemical bonds. It does not release the impurities under any circumstances when getter is in operation. A cold getter (SEAS MC1 902 F) was also used in place of the heated getter for a fraction of the growths. This getter is used for purifying Ar, He, Kr, N_2, Ne and Xe gases and operates at room temperatures. Its removes O_2, H_20, CO, CO_2, H_2 and Non-Methane Hydrocarbons (NMHC) impurities to < 1 parts per billion (ppb). The getter purifies Ar gas is then channeled through a LN2 cold trap before being leaked in to the main chamber. The cold trap (~67 K) condenses all vapors in the Ar gas.

Additional information on deposition rate calibration via *in situ* quartz crystal microbalance (QCM) and *ex situ* secondary ion mass spectroscopy (SIMS), can be found in Appendix 3.

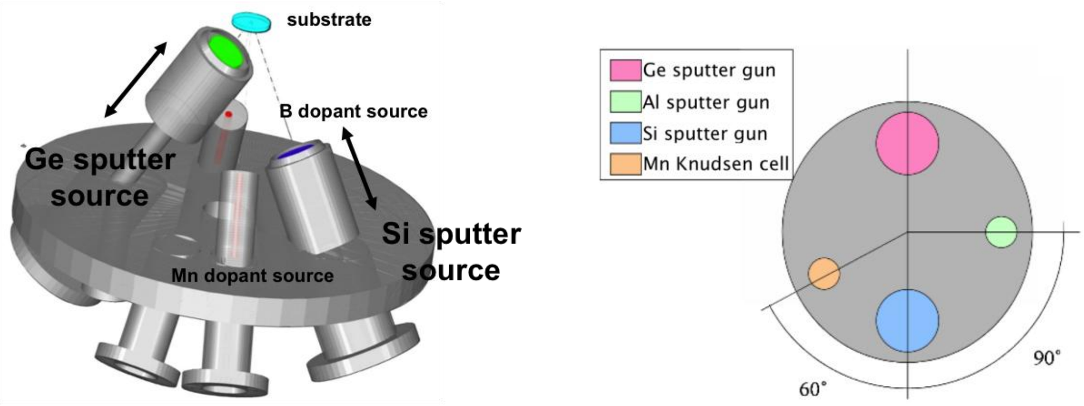

Figure 2-13: Layout of deposition sources in the HyperMBE [106].

2.7 Experimental details

Undoped Si (001) substrates, 263 µm thick, from Virginia Semiconductor, with resistivity ranging from 20-500 Ω cm and a miscut of 0.1˚ were used. The Si wafers from the box were chemically cleaned using a modified IMEC [107] Shiraki [108] method to produce substrate surfaces having reproducible smoothness and structural quality. We observed that 5 minutes IMEC clean was not enough to remove all the H-C on the Si surface, 9 minutes IMEC clean was used instead. This involves a H_2SO_4 + H_2O_2 mixture designed to remove organic contaminants from the wafer surface followed by a H_2O +HCl + H_2O_2 (3:1:1) mixture that forms a Si oxide coat, trapping metallic contaminants, which is later stripped off by a buffered oxide etch, and this sequence is repeated multiple times. The cleaning recipe included DI water rinses in between the steps

The wafers were then fixed on a molybdenum sample holder using ceramic tweezers and non-magnetic screw driver, and then loaded into the load-lock prior to transfer into the growth chamber after evacuation. The final protecting, non-stoichiometric SiO_x layer, formed in a concentrated H_2O +HCl + H_2O_2 mixture (1:3:1), was desorbed *in situ* at 820 ˚C for 10 minutes after a 15 hrs prebake at 600 ˚C. The cleaned Si surface structure was monitored *in situ* using reflection high-energy electron diffraction (RHEED) with primary energy equal to 23 keV in real time during desorption Prior to the QD's growth, a 500 Å thick Si buffer layer was then grown in a three-step growth method by varying the Si flux; 50 Å at 0.2 Å/s and T_s = 500 ˚C for followed by 450 Å at 0.5 Å/s and T_s = 750 ˚C and lastly, 0.2 Å/s and T_s = 750 ˚C. The firsts slow and cold step is meant to trap any defects and prevent them from propagating through the buffer.

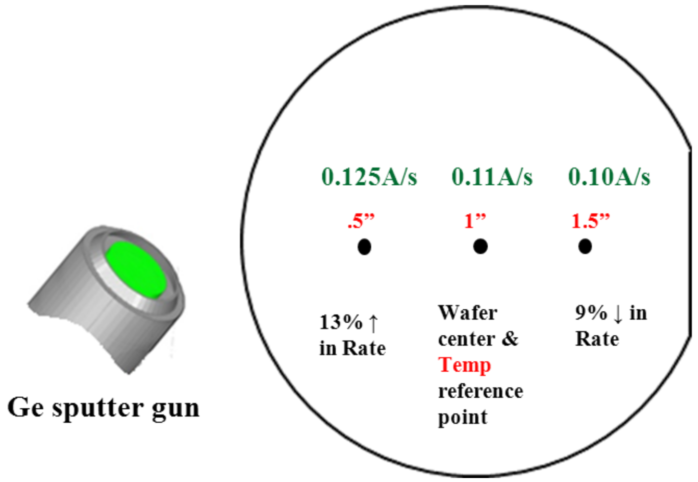

Figure 2-14. Schematic of the deposion rate gradient across the 2” Si wafer due to the geometry of the magneton sputter guns.

The pressure of the chamber was maintained at 4 mT of purified Argon, as measured by capacitance manometer during sputtering. Deposition rates were monitored using a quartz crystal rate monitor (QCM) that was moved into the exact substrate position. Ge QDs were grown at a deposition rate of 0.1 Å/s. It is critical that all sample characterized are cleaved from the center region of the wafer for consistency and for matching up to the calibrated deposition rate. We observed a deposition rate gradient across the 2” Si wafer (Figure 2-14) due to the geometry of the magneton sputter guns (this could be exploited for additional information in a given growth). The Ge and Si deposition rates are controlled by varying the DC gun power and the gun-to-substrate distance. The desired Mn flux was obtained by operating the Mn Knudsen cell at ~785 ˚C. The flux was found to be extremely sensitive to the chamber pressure, and to the length of time the cell was on. As a result, extreme care had to be taken maintain repeatable conditions from run to run. The cell also exhibits unusually long transient deposition rates after opening the cell shutter. To minimize shutter transient, the cell was fitted with an aperture that maintained a steady Mn deposition rate.

Chapter 3: $Ge_{1-x}Mn_x$ Heteroepitaxial Quantum Dots: Growth, Morphology and Magnetism

3.1 Introduction

This section will explore the growth and morphology evolution of $Ge_{1-x}Mn_x$/Si (001) self-assembled QD's as potential dilute ferromagnetic semiconductor. DMS strain-induced quantum dots pose a particular challenge to synthesize, since far above chemical equilibrium Mn incorporation in Ge requires low growth temperatures ($50\ °C < T_s < 85\ °C$) [42], [43], and low surface diffusivity to minimize phase separation and formation of unwanted phases, while quantum dot self-assembly invariably requires elevated growth temperatures and high surface diffusivity. By varying the Mn composition, we examine how the Mn flux interacts with the Stranski-Krastanov (SK) epitaxial growth mode. We characterize the impurity affects on epitaxial self-assembly and determine the overall magnetic response. In subsequent chapters we then look inside these samples with TEM to better characterize how Mn incorporates.

Quantum dots are candidates for the development of spin-based devices due to their ability to spatially localize magnetic moments at the nanoscale [12]. Achieving higher metastable doping levels might be a major limiting factor in enhancing the Curie temperature of the DMS. Recently, Xiu et al. presented evidence for above-room-temperature ferromagnetism in Mn-doped Ge quantum dots [9] formed by epitaxial self-assembly.

This remarkable result strongly motivates further research in this area. To gain further insight into the growth process and a better understanding of the magnetic properties, we investigate here the influence of Mn concentration on morphological evolution and magnetism of heteroepitaxial $Ge_{1-x}Mn_x$ QD's grown by molecular beam $Ge_{1-x}Mn_x$ films. Relevant to all two goals, 7.5 ML $Ge_{1-x}Mn_x$ QD's epitaxial films were grown with nominal Mn content of x = 0., 0.02, 0.05 and 0.10 and $T_g = 450$ °C. These conditions bracket all the common island morphologies in this system as well as those used by Xiu et al. We focused on growth at T_g that is on the lower end of typical Ge/Si (001) QD conditions, in order to better retain Mn and incorporate it as a substitutional dopant.

3.2 Growth

$Ge_{1-x}Mn_x$ epitaxial films were grown at 450 ºC with nominal Mn content of x = 0, 0.02, 0.05, and 0.10 and a $Ge_{1-x}Mn_x$ layer thickness of 6.5 - 7.5 monolayers (ML). For brevity, we shall simply refer to these as the 0%, 2%, etc., samples. These conditions bracket all the common island morphologies in the Ge/S (001) system. We focused on growth at T_g that is on the lower end of typical Ge/Si (001) QD conditions, in order to better retain Mn and incorporate it as a substitutional dopant. At 5% Mn, 3 ML and 6 ML thick films were also grown. Deposition rates were monitored using a quartz crystal rate monitor in the substrate position (QCM). Ge QDs were grown at a deposition rate of 0.1 Å/s.

The total Mn content (in atoms/cm^2) is quite small in these films, and non-trivial to determine. The Mn content in the 2% and 10% Ge:Mn QD films was verified using Secondary Ion Mass Spectrometry (SIMS). These two films were first capped with 100 nm amorphous Si deposited at room temperature. Ge and Mn SIMS depth profiles were obtained by sputtering through the Si cap, $Ge_{1-x}Mn_x$ QD layer and well into the Si substrate. The Mn signal was integrated over depth, and calibrated versus a Mn^+ implanted Si wafer standard. We have also performed optimized-sensitivity Rutherford Backscattering Spectroscopy on the 10% Mn sample, and the results agree well with SIMS.

3.3 Morphological Evolution:

RHEED patterns exhibit a 2x1 reconstructed Si surface after the oxide layer is desorbed at 800 ˚C and throughout the growth of 500 Å Si buffer at 750 ˚C. Figure 3-1 below shows RHEED images taken in the [011] azimuth. After the native oxide was desorbed at 800 ˚C for 10 minutes, the pattern develops a Laue circle of diffraction spots characteristic of an atomically flat and chemically clean, 2x1 reconstructed surface prior to growth, as shown in Figure 3-1 (a) and (b),. We obtain a transmission pattern in (c) due to 3D QD formation after co-deposition of 8.5ML of Mn_xGe_{1-x}/Si (001) at 450 ˚C.

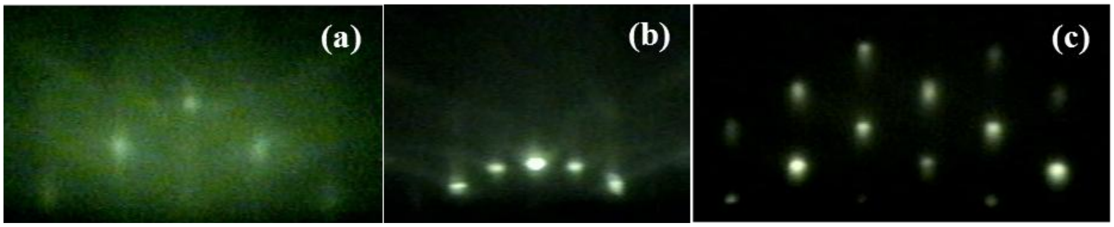

Figure 3-1. Typical RHEED patterns taken in the [011] azimuth of Si (001). (a) diffuse 2D (1x1) at 600 ˚C prior to native oxide desorption (b) first order Laue spots indicating a (2x1) surface reconstruction of Si after native oxide desorption at Ts = 800 °C. This 2D pattern is reminiscent of an atomically smooth 2-dimensional surface; (c) 3D pattern resulting from transmitted diffraction through 7.5 ML $Ge_{1-x}Mn_x$ quantum dots at 450 ˚C.

In the literature of Group IV epitaxy, transition metals are scrupulously avoided since they can strongly impact epitaxial growth.

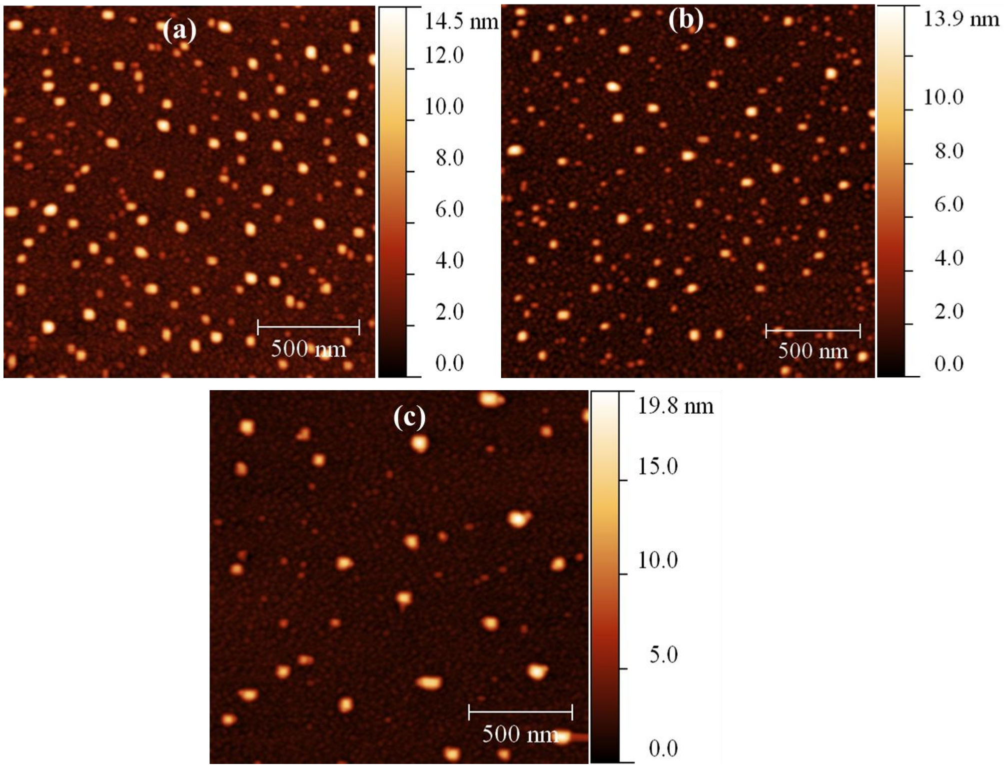

Figure 3-2. Comparison of morphological evolution with Mn content. 4 µm^2 AFM images of 7.5 ML Ge$_{1-x}$Mn$_x$ QD's heteroepitaxially grown on Si (001) with x = (a) 0, (b) 0.02, and (c) 0.05.

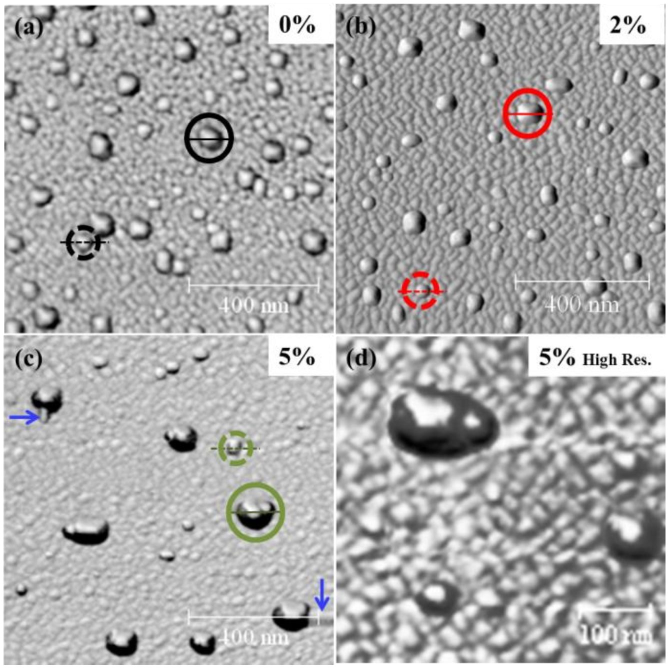

Figure 3-3. Comparison of morphological evolution with Mn content. (a) to (c): 1µm^2 AFM phase images of the same three samples as in Figure 1. Phase images reveal contrast associated

with faceting of the quantum dots. Topographic linescans have been obtained for the circled QDs and are shown in Figure 3-5. Arrowed features in (c) show incipient nanorods. (d) Higher resolution image of (c) obtained with a diamond- like carbon tip.

Quantum dot self-assembly would be expected to be particularly sensitive to a large metallic impurity flux. Figure 3-2 shows the island morphology as a function of Mn content in 7.5 ML Ge:Mn QD films grown the 0%, 2% and 5% samples, where the 0% film serves as a referent for our growth conditions. The standard quantum dot morphologies ubiquitous to the Ge/Si (001) system are observed in all three cases: “hut cluster” islands bound by pyramidal {105} [92] facets (“H”), dome clusters (“D”) bound by higher-angle [88] facets and larger superdomes (“SD”) [94], which are ostensibly semi-coherent due to the introduction of interfacial misfit dislocations. Overall, we observe a tri – modal growth distribution as shown in Figure 3-4.

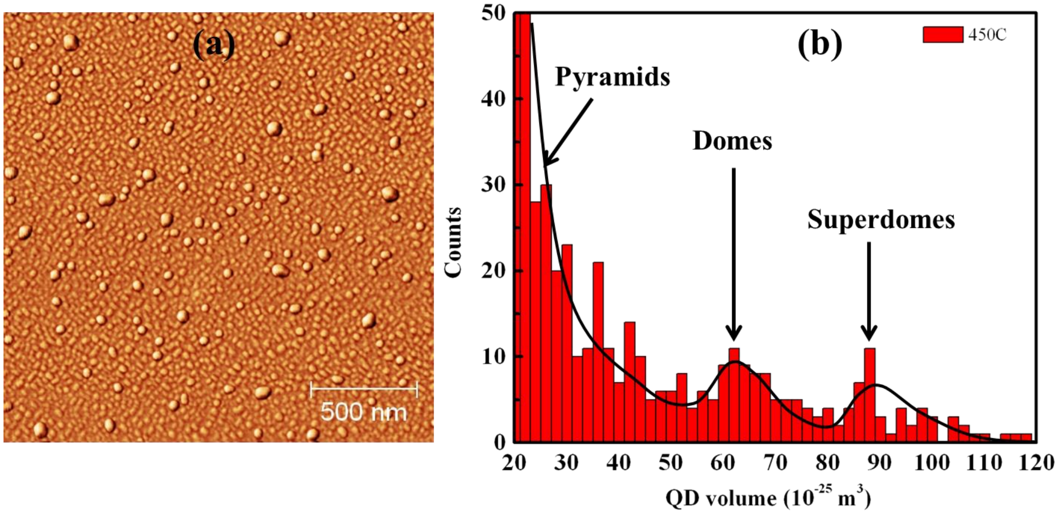

Figure 3-4. Left: 4 µm^2 AFM scan of a 7.5 ML Ge/Si (001) QD’s grown at 450 ˚C, with no added Mn. Right: Statistical volume distribution of the island showing a tri-modal distribution (pyramids, domes and superdomes.

With 2% added Mn, there is no perceptible affect on the Ge QD morphology, either qualitatively or quantitatively, as the distribution of island sizes and shapes is largely unaffected by the Mn flux. However, at 5% Mn, the morphology is more clearly perturbed. Figure 3-2 (c) and Figure 3-3 (c) suggest a significant reduction in the density of the D and SD areal density, accompanied by an increase in the mean QD size (these statements will be quantified below).

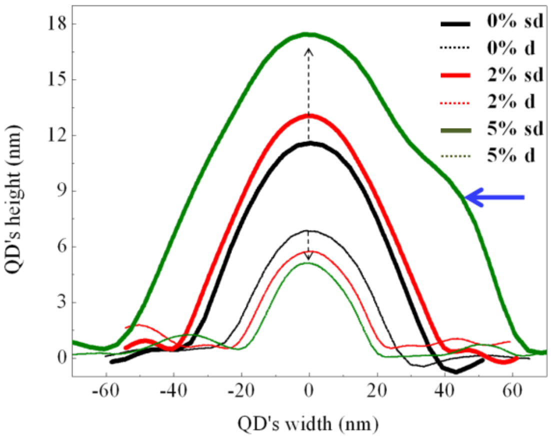

Figure 3-5. Comparison of morphological evolution with Mn content. Line scans obtained from the labeled islands in Figure 3-3. The solid lines correspond to superdomes (SD) and dashed lines to domes (D). The arrow highlights a protrusion.

Importantly, at 5% Mn, many of the Ge superdome islands exhibit *protrusions* - conjoined smaller islands, as shown in Figure 3-3(c) and (d). These are most likely second phase particles, as will be further demonstrated below. Figure 3-3(c) reveals that some of the protrusions actually have a rod-like appearance (arrows).

At 10% Mn content, major changes in morphology become apparent, see Figure 3-6, with large rod structures oriented along the two equivalent [110] directions of the substrate, which can be up to 1 um long, and are 50-100 nm across. Numerous, more equiaxed particles, whose asymmetric shapes differentiate them from the co-existing population of Ge D and SD dots, are also observed. There is an overall reduction in QD areal density, and the hut islands appear less well formed, in agreement with a recent scanning tunneling microscopy study [93].Equiaxed nanoclusters are more common in areal density than nanorods, but both are present over extended regions of the sample.

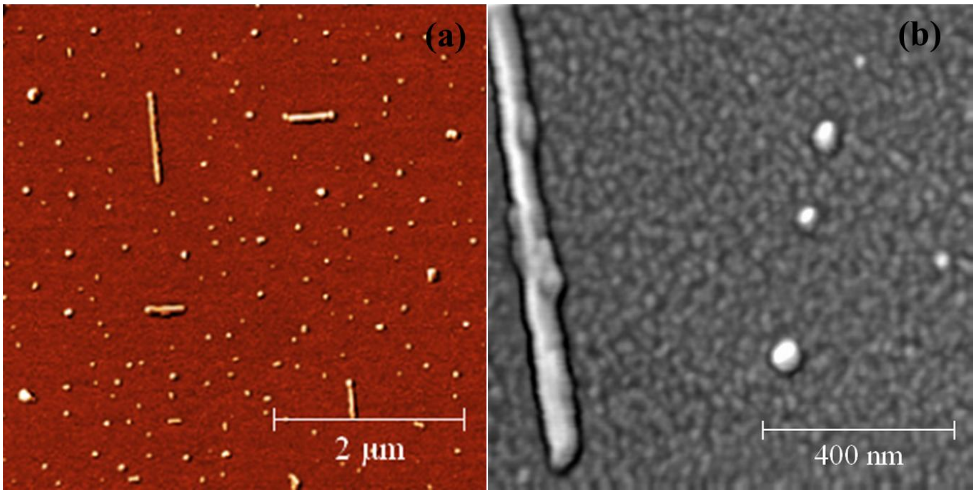

Figure 3-6. Morphology of second phase precipitates. (a) 25 μm^2 and (b) 1 μm^2 AFM phase images of 8.5 ML $Ge_{1-x}Mn_x$ /Si (001) QD's with x = 0.10.

At larger AFM scan sizes it becomes apparent that the rods have a dome denuded zone about them where D/SD islands and other intermetallic clusters do not form (although huts appear unperturbed), as shown in Figure 3-6 (a). Rods usually have a Ge QD attached to them, typically at one end. Additionally, they appear to be decorated by Ge along their length.

Table 3-1 and Figure 3-7 summarizes the trends in morphological evolution with Mn content. To obtain this data, a "flooding" process was performed to raise the local baseline height to a point where the domes, superdomes, and second phase particles are isolated above the background of small hut islands. Subjectivity in choosing the baseline is reflected in the error bars of in Figure 3-7. Flooding could not be performed for the huts themselves, so this data was obtained manually counting individual huts in a fixed area. It can be seen that increasing Mn content tends to increase the D/SD mean volume and decrease the areal density of these structures. Hut size (and therefore density) is nominally unaffected. We observed a peak in the areal density of second phase particles at x = 0.05. The implications and origins of this behavior are discussed later.

	x = 0	x = 0.02	x = 0.05	x = 0.10
SD vol. * 1E-24m^3	25.4 ± 1.3	19.7 ± 6.9	39.7 ± 1.5	84.0 ± 13.0
D vol. * 1E-24m^3	5.2 ± 0.6	3.9± 0.9	8.5 ± 2.5	13.9 ± 3.1
No. of D/SD per µm^2	52 ± 3 (6%)	49 ± 2 (4%)	14 ± 8 (66%)	9 ± 1 (11%)
D/SD vol. *1E-21/µm^2	0.59 ± 0.09	0.34 ± 0.01	0.3 ± 0.10	0.24 ± 0.03
No. of huts/µm^2	1674	1367	1300	1298
No. of nanostructures/µm^2	0	0	4.8 ± 0.5 (10%)	1.9 ± 0.3 (15%)
Mean “dome” grain size (nm)	36 ± 4	30.0 ±0.5	46 ± 4	44 ± 2
No. of D per µm^2	36 ± 3 (8%)	29 ± 5 (18%)	11 ± 1 (4%)	4.3 ± 0.5 (11%)
No. of SD per µm^2	15 ± 3 (6%)	17 ± 5 (29%)	7.4 ± 0.8 (11%)	5.0 ± 0.5 (10%)
SD vol. * 1E-21 per 1µm^2 AREA	0.31 ± 0.09 (29%)	0.27 ± 0.05 (20%)	0.35 ± 0.02 (6%)	0.45 ± 0.01 (2%)
Mean hut lateral size (nm)	36 ± 1 (3%)	30 ± 2 (7%)	34 ± 2 (6%)	30 ± 1 (3%)

Table 3-1. Tabulation of QD’s and nanostructure sizes, distribution and density obtained from AFM scans.

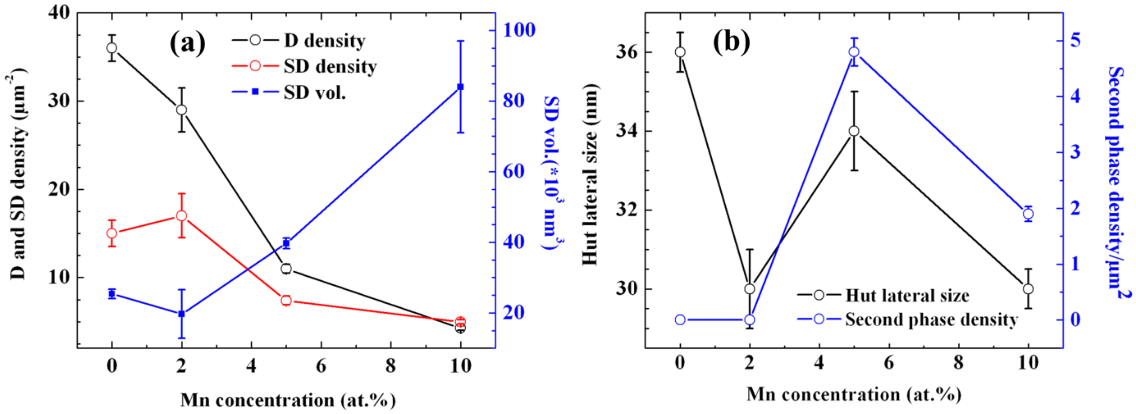

Figure 3-7. The effect of Mn content on size and areal density of various surface structures obtained from AFM scans. (a) D/SD areal density and SD volume; (b) mean lateral hut size and second phase areal density.

3.4 Magnetism:

As earlier mention in chapter 1, our most Mn-rich sample, the 10% sample, contains only 4.7x10^{14} Mn/cm^2, less than a full monolayer of atoms when referenced to the Si (001) plane. For a sample size of 4 x 6 mm (typical of the size required in magnetometers), the largest possible magnetic signal attributable to Mn is ~ 4.5 x 10^{-6} emu, assuming the Mn moment of 3 - 5 μ_B/Mn [109]. Although a SQUID magnetometer has the sensitivity to detect such a signal above the noise, the key challenge comes in accounting for signals from the surroundings. For example, the diamagnetic signal from a 260 μm thick Si substrate of the same lateral dimensions is 1.5 x 10^{-4} emu, ~10^{2} times larger than the Mn signal. Figure 3-8 (a) shows the unsubtracted M(H) of a 2% sample weighing 0.01406 grams. Even if spurious effects from impurities or the sample mounting agent are avoided or accounted for, we are inevitably left with the need to subtract a relatively very large substrate signal in order to reveal a very weak signal from the submonolayer of Mn. The resulting data will thus be very sensitive to the details of the subtraction process. Short of removing the substrate, these issues are intrinsic to investigating such small quantities of magnetic dopant, and the data must be viewed critically. Since this aspect is critical, we discuss our subtraction method in some detail here.

The total magnetic signal measured by the SQUID is the sum of the following contributions: the diamagnetic signal from the substrate, any parasitic ferromagnetic signal from the substrate (e.g., due to low-level transition metal impurity clusters), and the combined signal of any ferro/para/superpara/magnetic phases associated with Mn incorporation. In order to obtain the magnetization curves only due to Mn doping, we remove a line of negative slope representing the diamagnetic susceptibility of the Si substrate. This diamagnetic signal is taken at 100 K (300 K and 100 K data have a similar slope but the latter is considered less susceptible to parasitic magnetic contributions).

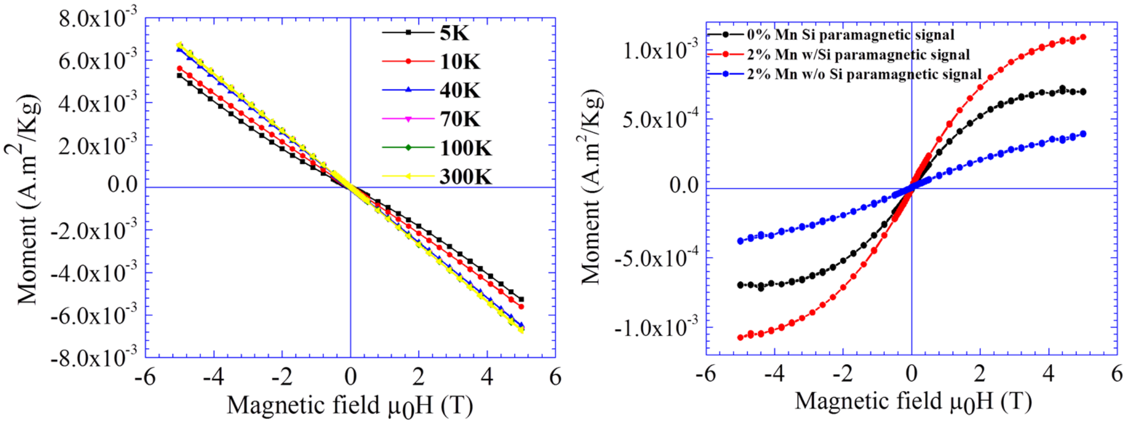

Figure 3-8. LEFT: SQUID measurement of raw M(H) curve of 2 at.% Mn sample before subtraction; RIGHT: M(H) curve of 0% Mn reference sample (black curve) and 2% Mn (red curve) at 5 K., with the diamagnetic slope at 100 K already been subtracted in both cases. The blue curve is the resultant M(H) curve of our film after subtracting the Si paramagnetic signal (black curve) from the red curve.

In addition, Si substrate exhibits a paramagnetic signal at low temperature that must be accounted for in the data analysis as shown in Figure 3-8. For this purpose, we subtracted (after mass renormalization) the M(H,T) data of the 0% sample from the 2% and 10% M(H,T) data (i.e, the control data at identical temperatures was subtracted). For a sample with *y* at. % Mn, this subtraction at temperature *x* Kelvin is given by;

$$M_{x\ Kelvin}^{y\ at.\%}\ H = M_{x\ Kelvin}^{y\ at.\%}\ H - H\,\frac{\Delta M}{\Delta H}\,\Big|_{100\ K}^{0\ at.\%} - M_{x\ Kelvin}^{0\ at.\%}\ H - H\,\frac{\Delta M}{\Delta H}\,\Big|_{100\ K}^{0\ at.\%} \tag{3-1}$$

A weakness of this approach is that variations in any parasitic magnetic impurities from substrate-to-substrate could greatly impact our ability to quantitatively interpret the data. Finally, we did not attempt subtractions for M(T) data; instead, we derive insight from direct comparisons of the curve shape in the 2% and 10% samples vs. the 0% Mn control.

Figure 3-9 compares the resulting magnetism data for the 2% and 10% samples. For the 2 at.% Mn sample at 5K, the M(H) curve is readily fit to either a Langevin or

Brillouin function, with similar results: the nominal moment is 4.1 ± 0.1 Bohr magnetons, which is reasonable. However, the areal density of magnetic species is $1.3\text{x}10^{15}$ cm^{-2}. This number is 10x greater than the known areal density of Mn from SIMS. This suggests the data is still subject to subtraction-related issues as discussed above or we have super-moments due to Mn superparamagnetic particles that have a blocking temperature below 5 K. It is therefore difficult to interpret this data. Similar considerations apply to the ZFC-FC data in Figure 3-9 (c) and the $M_r(T)$ data in Figure 3-9(d). It is clear, however, that we do not observe room temperature ferromagnetism.

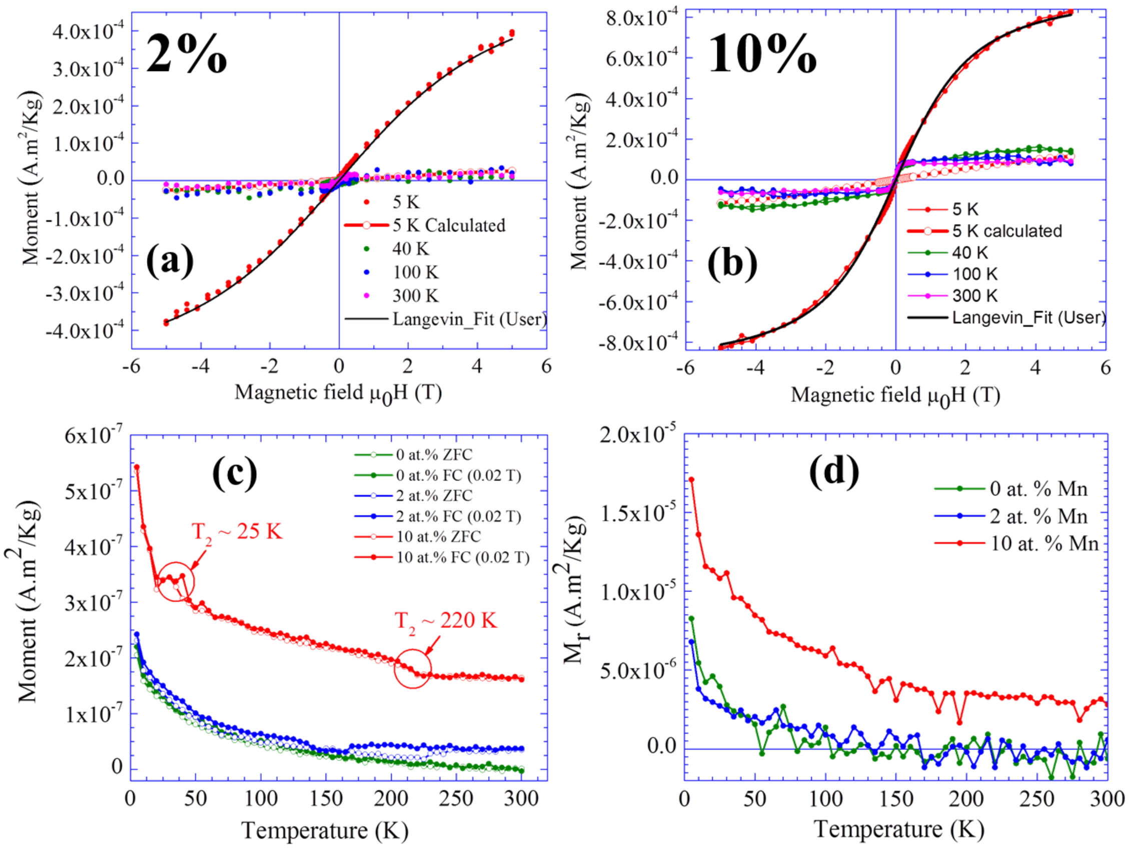

Figure 3-9. In-plane SQUID magnetism plots. M(H) curve of (a) 2 at. % Mn and (b) 10 at.% Mn samples showing loops from 5 to 300 K.; (c) ZFC-FC curves obtained at 0.02 T for the 0, 2 and 10% samples; (d) Remanence vs T for the 0, 2, and 10% sample.

Figure 3-9 (a) and (b) shows the calculated M(H) loop expected at 5 K assuming that Mn atoms are all active with a 3 μ_B moment and are substitutionally incorporated in the matrix.

For the 10% Mn sample, we observe a ferromagnetic signal that persists to 300 K. Fitting the M(H) curve at 5 K to a Langevin function (after subtracting the 300 K ferromagnetic moment), we obtain 6.7 ± 0.1 Bohr magnetons and a Mn level = 2.05×10^{15} atoms/cm^2. This Mn levels is 4x higher than that reported by SIMS. The ZFC-FC plot shows clear evidence of two magnetic phases, a paramagnetic phase with T_c at 25 K and a ferromagnetic phase with a T_c at 220 K.

The interpretation of this data will be will be discussed in more detail in the following two chapters.

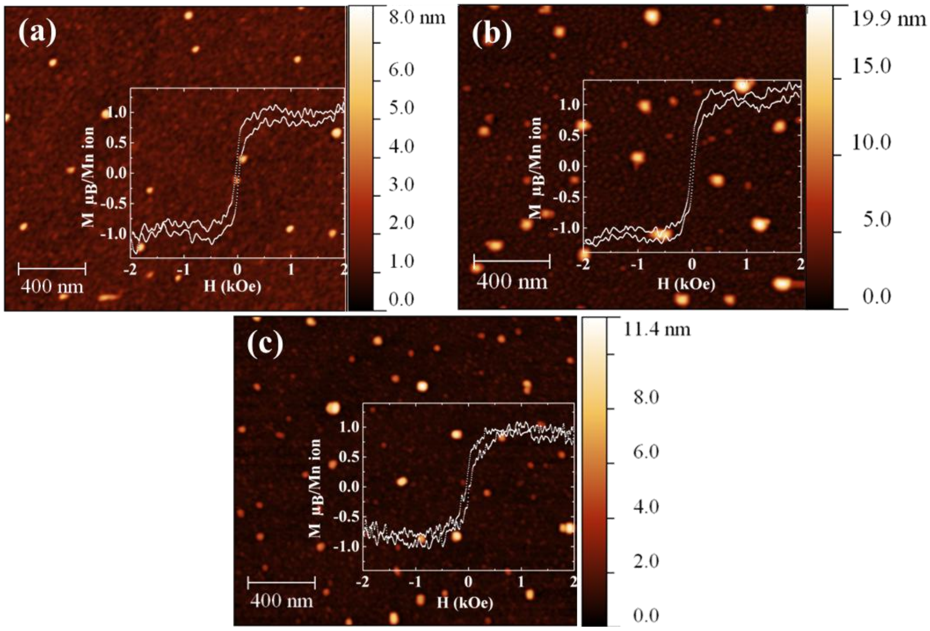

Figure 3-10. Comparison of surface morphology for different growth conditions with fixed Mn content of x = 0.05 from AFM scans. (a) 6 ML $Ge_{0.95}Mn_{0.05}$ at 450°C; (b) 8.5 ML $Ge_{0.95}Mn_{0.05}$ at 450 °C, and (c) 8.5 ML $Ge_{0.95}Mn_{0.05}$ at 400 °C. Inset: Corresponding VSM M(H) loops at 5 K showing a comparable magnetic moment in all the three cases.

Figure 3-10 (a) and (b) compare the surface morphology for $Ge_{0.95}Ge_{0.05}$ films grown at 450ºC, 6 ML and 8.5 ML thick. The 6 ML film has a much smaller density of dome QDs, and no SDs, which is expected for this thickness. Figure 6(c) shows the M vs. H loops for these samples at 5K, measured using a VSM. We find that the saturation moments measured by VSM are larger than those from the SQUID. Nonetheless, we do believe that relative behavior in the VSM data for samples with different Mn amounts, or as a function of measurement temperature, are meaningful. In the case of the two samples shown in Figure 3-9, identical M(H) loops are obtained (when M is normalized by the Mn amount), and M_s vs. T data are identical as well. It's worth pointing out that the parasitic magnetic effects due Si has not been subtracted in these VSM measurements. Therefore, this data cannot be qualitatively quantified any further.

3.5 Discussion

In what follows, we first compare our results with recent results in the literature for Mn doping during Ge QD formation during Ge/Si (001) molecular beam epitaxial growth. We then discuss in more detail how Mn affects and interacts with QD morphological evolution, and comment further on the magnetic behavior.

Comparison with recent literature results

As described in Chapter 1, Xiu, et al., recently reported room temperature ferromagnetism in Mn-doped Ge quantum dots on Si (001) [14,15]. They used conditions nominally quite similar to those being used here, i.e., Ge thickness 8.5 ML (1.2 nm), MBE growth temperature 450 ºC, deposition rate of 0.02 nm/s, and an estimated overall $Ge_{1-x}Mn_x$ content of x = 0.05.

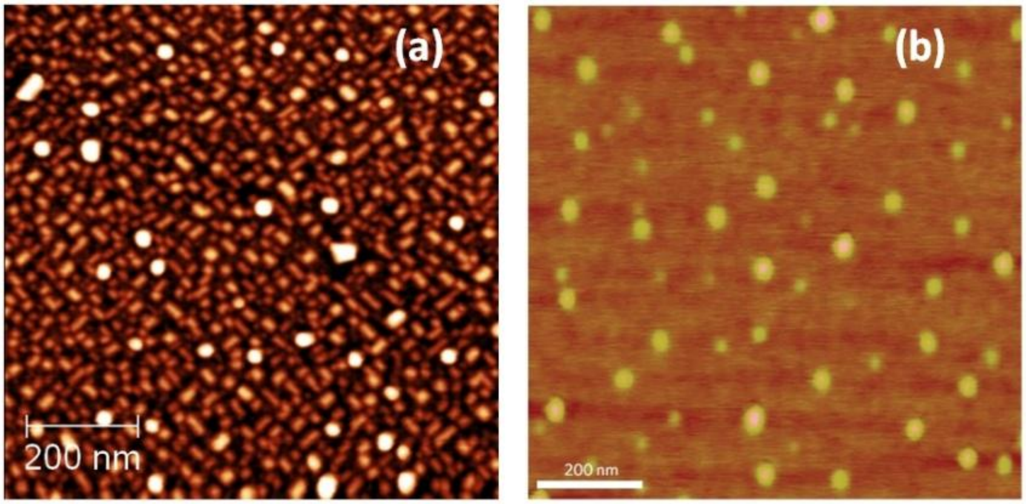

Figure 3-11. AFM comparison between 8.5ML $Mn_{0.05}Ge_{0.95}$ /Si(001) quantum dots at Ts=450˚C between (a) our samples and (b) Xiu, et al. sample [9].

They observed a Curie temperature > 400 K, with M_{sat} varying only from 1.8 to 1.5 μ_B/Mn at 5 K to 400 K respectively. TEM investigations indicate Mn incorporates both in the Ge QDs and in the Si underneath the QDs, but only diamond cubic structure is observed, that is, there are no indications of second phase formation. Our work brackets the growth conditions of Xiu, et al., but the results we obtain are rather different, both in terms of magnetic response, and in the surface-morphological and phase evolution.

In our samples, with overall Mn contents ranging from 2 – 10 at.% relative to Ge, ferromagnetism is only observed for T < 220 ºC, in the 10% sample, likely arising from second phases rather than a DMS phase (see Chapter 5). In the 2% Mn sample, paramagnetism is observed at low temperatures that likely includes a spurious contribution. Although there are challenges with the analysis of the magnetic data at such low signals, as described earlier, which may contribute to quantitative differences in M_{sat} between our work and Xiu, et al., we are confident that our samples are not ferromagnetic near room temperature.

All our films show the typical quantum dot morphologies observed for Ge/Si (001) growth, including hut clusters, domes and superdomes. As discussed more below, there are quantitative differences in size and areal density amongst our samples at higher Mn contents, but the island morphology is surprisingly insensitive to Mn flux. Xiu, et al., observed dome islands on a similar size and areal density level to ours, but {105} huts or pyramids are not observed, suggesting a more dramatic effect of Mn on QD formation than is observed here. They also did not observe SD islands, suggesting their mass equivalent film thickness was somewhat smaller than ours. However, the data shown in Figure 3-10, where the saturation moment was the same for two films with very different areal densities of D and SD dots, suggest that the magnetic response is not tied to these specific morphologies. This differs from Xiu, et al., where magnetic force microscopy isolated the magnetic moments to only the dome islands. Furthermore, in our samples, at 5% Mn content and higher, AFM micrographs show clear indications of second phase formation, not observed by Xiu, et al., at nominally the same overall Mn content. This is consistent with other studies showing copious second phase formation Ge:Mn/Ge (001) films, for growth temperatures above about 200 ºC (or lower) [23], [42], [43], [61], [110] ,and for Mn on Si (001) at 450 ºC [111].

Mn effects on morphological evolution

Somewhat surprisingly, the effect of Mn on surface morphology is relatively benign when 2% Mn flux is added to the Ge flux onto the Si (001) surface at 450 ºC. The morphology of $Ge_{1-x}Mn_x$ QDs closely mirror those observed in a pure Ge/Si (001) growth under the same condition and there is no obvious surface morphological indicator of second phase formation. However, for similar Ge mass equivalent thickness, secondary phase formation is observed by AFM for Mn concentrations $\geq 5\%$. Even then, however, the standard Ge QD morphologies persist, and are only slightly perturbed. Increasing Mn content does drive a clear decrease in D and SD areal density. Concurrently, mean D volume decreases while mean SD volume increases. The mean lateral size of the huts is largely unperturbed. These observations indicate that Mn flux somehow assists superdome coarsening kinetics at the expense of domes. This could arise from Mn acting as a surfactant, enhancing the surface mobility of Ge, or reducing detachment barriers. Mn has also been observed to similar effects on other Si surfaces [52].

Nanorods and nanoclusters first become apparent in AFM micrographs of samples with higher Mn content. Although we have not rigorously demonstrated here that these features are second phase nanostructures, extensive TEM analysis that shows this will be reported in subsequent chapters. The 5% Mn sample shows nascent second phase particles that appear to preferentially nucleate on Ge superdomes, perhaps due to the inhomogeneous strain at their perimeter. According to the data of Figure 3-7, there is a large drop in the areal density of 2nd phase particles going from 5% to 10% Mn. Presumably this results from nanorod growth and coarsening at the expense of the equiaxed nanoclusters. This could be driven by capillarity (reduction in the total interfacial energy) and/or reduction in chemical potential if the nanorod phase has lower free energy of formation.

Magnetic behavior

Experimental reports on magnetism in Ge:Mn alloys vary drastically, with Curie temperatures ranging from 5 - 400 K [17], [20], [112], [45], [46], [26], [21], [30], [38], [48], [10], [113], [75]. Mn is known to distribute inhomogeneously in Ge, even at temperatures low enough to suppress nucleation of crystallographically-distinct germanide phases [43], [45]. These Mn-enriched nanoclusters and/or nanocolumns, with a typical diameter of less than 5 nm, appear to be diamond cubic, in which case the Mn atoms are either substitutional or interstitial, or in some cases, amorphous structure is reported [45], [114], [115]. Mn concentration in these clusters has been measured using atom probe tomography to be as high as 20% for a film with average concentration of 2%, while EELS studies of nanocolumns indicate Mn enrichment to 30 - 40%. Under a narrow range of growth conditions, Jamet, et al., have shown nanocolumns exhibit T_c = 400 K. Similar to the observations of Xiu, et al., for Ge:Mn QDs, the origins of high temperature ferromagnetism are not well understood. What does seem clear is that the local environment of each Mn is critically important to the magnetism, and extremely difficult to control or even measure accurately. The wide range of reported magnetic response in the literature must be, in large part, due to this effect. The situation becomes ever more complex in this work, where the Si substrate may also play a role in the 2nd phase formation process.

3.6 Conclusion

We have synthesized epitaxial self-assembled heteroepitaxial $Ge_{1-x}Mn_x$ QD’s by MBE co-deposition, to examine the role of relative Mn flux on the QD morphology and magnetization. The affect of Mn on QD morphology is surprisingly benign at low Mn contents, but Mn does appear to enhance Ge surface mobility at higher flux levels. At 2% Mn relative to Ge, only standard Ge QDs are observed, whereas 2nd phase protrusions are observed nucleating on Ge dots at 5% Mn, and extensive 2nd phase structures are present on the surface for 10% Mn. In all cases, however, only low temperature ferromagnetism was observed. Further characterization using transmission electron microscopy is reported in the following chapters to assess the internal structure and chemistry of these films, in order to better understand how Mn incorporates, and to determine the origins of magnetism in this complex system.

Chapter 4: Mn Solid Solutions in Self-Assembled $Ge_{0.98}Mn_{0.02}$/Si (001) Quantum Dot Heterostructures

4.1 Introduction

This section will explore how Mn chemically incorporates in the inherently inhomogeneous $Ge_{0.98}Mn_{0.02}$ heteroepitaxial QD's quantum dot system, especially given the relatively high growth temperature of 450 ºC. It is critical to our understanding of the resultant magnetic properties to better assess how Mn chemically partitions in the intrinsically inhomogeneous Ge/Si (001) QD system. Here we provide detailed cross-section transmission electron microscopy (TEM), energy dispersive analysis of x-rays (EDX) and secondary ion mass spectrometry (SIMS) depth profiling of the structure and composition of $Ge_{0.98}Mn_{0.02}$ heteroepitaxial QD's.

4.2 Experiment

The 7.3 ML $Ge_{0.98}Mn_{0.02}$/Si (001) QD's were grown by MBE using magneton co-sputtering in 4.3 mT of getter-purified Ar. The base pressure was 1 x 10^{-10} Torr. Undoped Si (001) substrates were chemically cleaned and passivated with a sub-oxide that is desorbed in situ at 800 ºC; details are described elsewhere [Chapter 2]. Prior to the QD growth, a 500 Å Si buffer layer was grown at 750˚C, resulting in a smooth, 2x1 reconstructed surface as indicated by a bright circle of Laue spots in reflection high energy electron diffraction. A 7.3 ML thick Ge:Mn film was grown at 450 ºC and 0.1 ML/min. The film was analyzed by SIMS using Cs^+ ions at 5 keV and 60 ˚off-normal incidence. The SIMS film was first capped with 100 nm amorphous Si. Depth profiles for Ge and Mn were obtained by sputtering through the Si cap, Ge_{1-}QD layer and well into the Si buffer. The Mn signal was calibrated versus a Mn^+ implanted Si wafer standard. The total Ge integrated over depth was 4.96×10^{15} at/cm^2 while Mn was 1.05×10^{14} at/cm^2, which gives a nominal composition of 2.1 at% Mn in Ge (but we show below that Mn partitions into the Si as well). Surface morphology was characterized *ex situ* using atomic force microscopy (AFM) in tapping mode. BF TEM, STEM and HAADF were employed for high-resolution spatial imaging and compositional analysis using EDX. Samples for TEM and STEM were prepared by standard wedge polishing techniques followed by Ar ion milling. An FEI Titan 80-300 kV S/TEM operating at 300 kV was used for STEM and high resolution TEM (HRTEM) imaging. Magnetic properties were measured using a superconducting quantum interference device (SQUID) with an external field parallel to the film plane. Again, the samples were cooled in maximum field (MFC) for the field dependent magnetization loops. Zero field cooled and field cooled (ZFC-FC) measurements were conducted. The sample is cooled down to 5 T without magnetic field followed by a weak field (0.02 T) is applied. The samples were carefully handled and stored to prevent spurious magnetic contamination.

4.3 Results

Morphology

Even with a 2% Mn flux during Ge growth, we still observe self-assembly of the standard quantum dot morphologies ubiquitous to the Ge/Si (001) system as shown in Figure 4-1 “hut cluster” islands bound by pyramidal {105} [92] facets (“H”), dome clusters (“D”) bound by higher-angle [88] facets and larger superdomes (“SD”) [94], which are ostensibly semi-coherent due to the introduction of interfacial misfit dislocations. No other atypical island morphologies are observed, suggesting that copious second phase formation has not occurred yet. Second phase formation does become readily obvious in AFM for $Ge_{0.95}Ge_{0.05}$ films, where small protrusions emerge from Ge SD and D dots [Chapter 4] and for $Ge_{0.9}Ge_{0.1}$ films, second phase precipitates dominate the overall surface morphology [Chapter 5]. Hence it is of great interest here to understand where the Mn is located, in the absence of obvious precipitates.

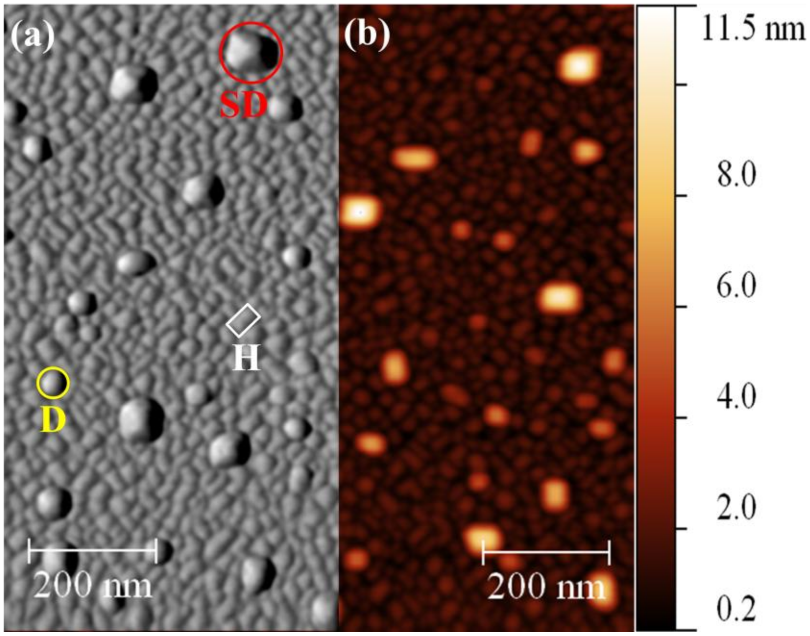

Figure 4-1. Morphology of 7.5 ML $Ge_{0.98}Mn_{0.02}$ QD's from AFM. (a) Phase image elucidating faceting; (b) topography scan.

SIMS analysis

Figure 4-2 shows the distribution of Mn and Ge with depth in the film obtained from SIMS. From this data, we estimate that 69 - 75% of the deposited Mn atoms reside in the 7.5 ML Ge layer, i.e., *the average composition of the Ge layer is about 1.5* ± 0.1 *at.% Mn*, assuming the Mn is equally distributed in all the dots and the Ge wetting layer. The remaining 0.5 at% Mn segregates into the underlying Si, as shown below. Since this is an important and non-trivial conclusion, some discussion of the interpretation of the

SIMS data is in order. First, note that the Ge peak width (full-width half-maximum) in Figure 4-2 (b) is 8 nm. Although the mass equivalent Ge film thickness is only 1 nm, the quantum dots range in height, with SD islands typically being 10-14 nm high. While ion mixing occurs during SIMS, thereby broadening the profiles, Mn will experience a longer recoil path into the Si substrate than Ge, which actually implies that our estimate of a 1.5% Mn in Ge solution concentration is a lower bound.

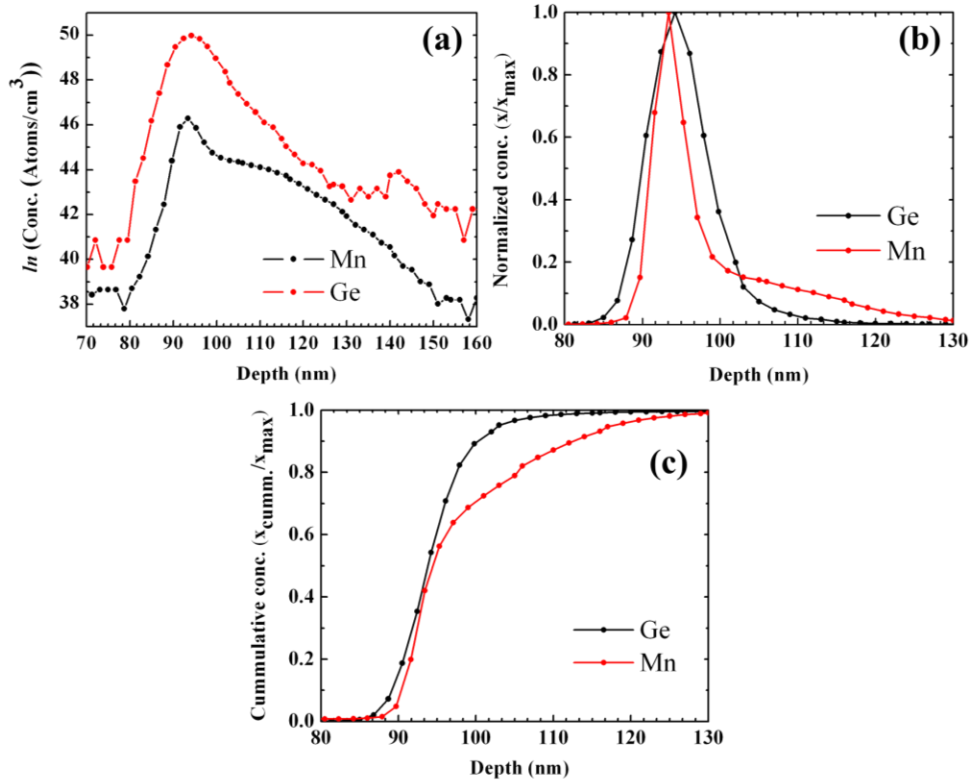

Figure 4-2. SIMS depth distribution profiles of Ge and Mn in the $Ge_{0.98}Mn_{0.02}$ QD's. (a) Raw data on a log scale; (b) normalized linear profiles; (b) cumulative profiles.

The long tail of the Mn profile to deeper depths into the Si substrate is partly due to diffusion of Mn into Si during growth, and partly due to ion mixing during SIMS analysis. In our estimation, the shoulder region in the Mn profile of Figure 4-2 (a) (below 115 nm depth) primarily results from Mn incorporation in the Si.

Structure

Figure 4-3 (a) and (b) show cross-section BF TEM micrographs exhibiting typical Ge dome and superdome islands, with diamond cubic crystal structure and either coherent or dislocated interfaces with the Si.

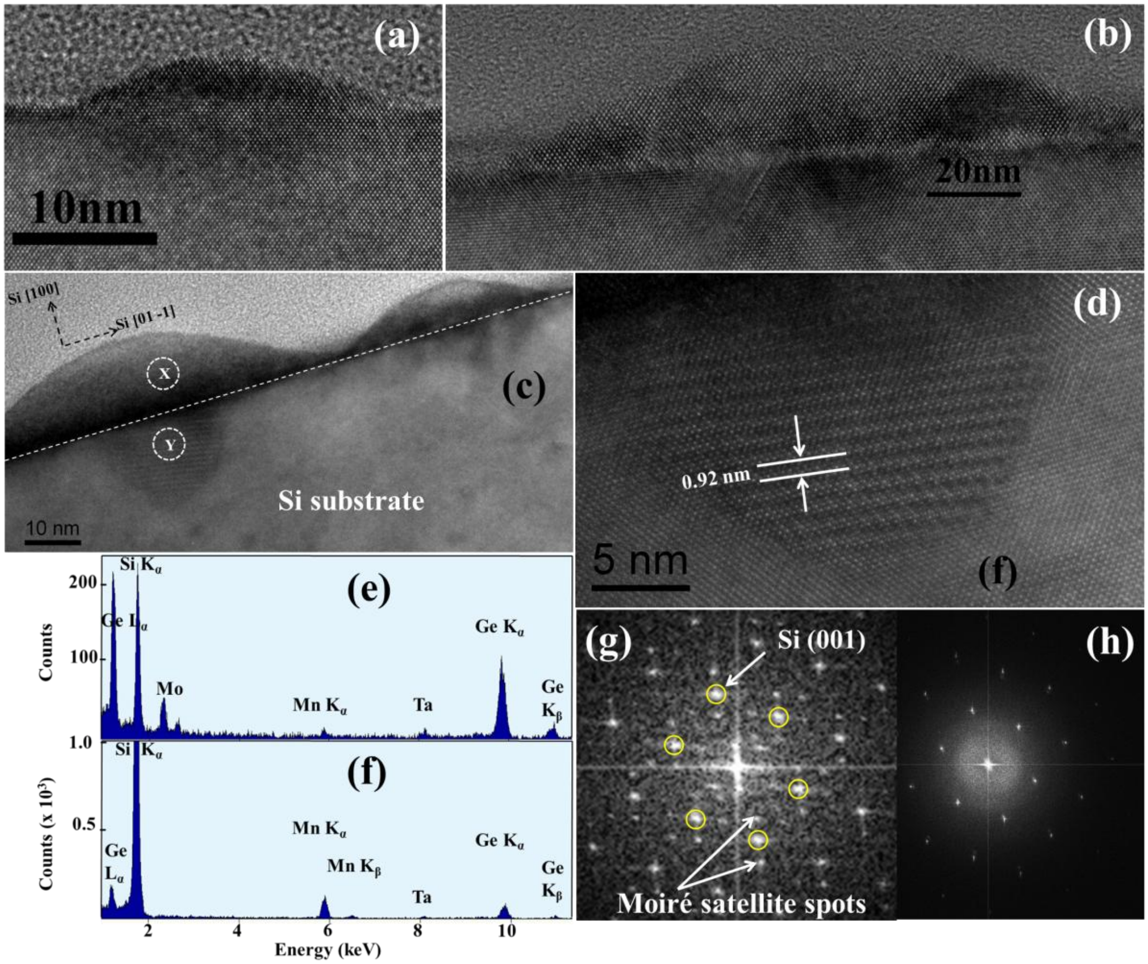

Figure 4-3. BF TEM micrographs along Si [1-10] of $Ge_{0.98}Mn_{0.02}$ QD's showing (a) and (b) coherent Ge QD island with excellent lattice coherence with the Si substrate; (c) buried structures below a fraction of the QD's; (d) HR image of the buried structure; (e) and (f) EDX point scans corresponding to point X and Y in part (c) respectively; FFT analysis of the (g) buried structure and (h) Si substrate.

Since SIMS indicates a mean content of 1.5 at. % Mn in the Ge layer, the Mn incorporated in the islands must be in solution, either substitutional or interstitial. As shown in the figures, we also observe buried structures in the Si substrate directly underneath Ge superdomes, which were not detected by AFM. These structures typically have a roughly equiaxed cross-section and display sharp interfaces and highly regular Moiré fringes with spacings of order 1 nm. These buried regions therefore must be crystalline but not isostructural to Si. However, their crystal structure has not been indexed, and, based on the Moiré patterns observed from different structures; they exhibit a range of lattice orientations and/or crystal structures.

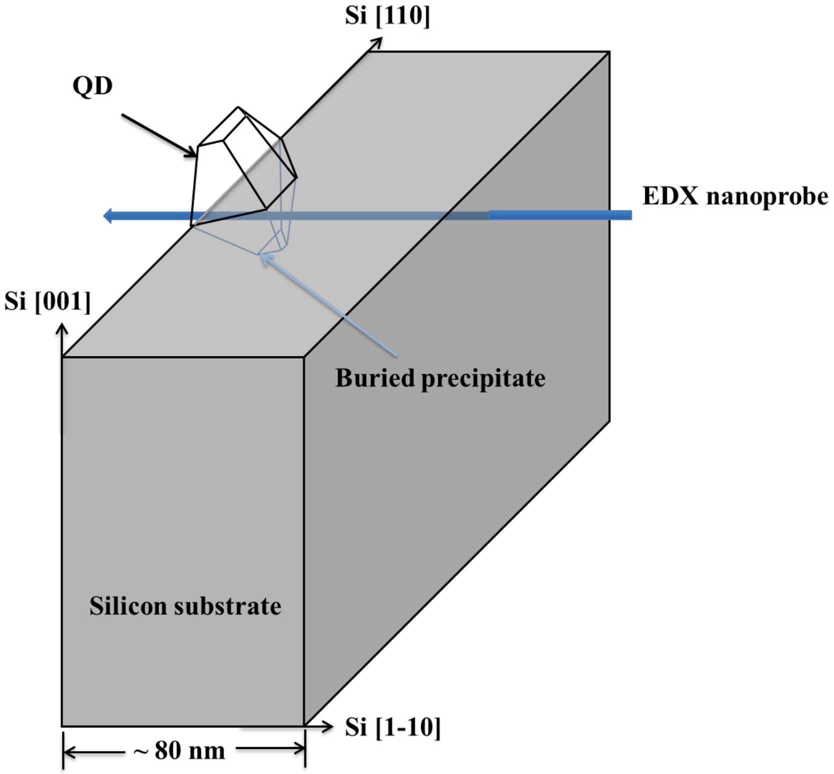

Figure 4-4. Illustration of a ~10nm wide precipitate buried in the Si substrate.

EDX point analysis at points (X) and (Y) in Figure 4-3 using a 2 nm probe were performed, Figure 4-3 (e) and (f). Mn was detected both in the Ge SD and in the buried precipitate, but the K_α peak intensity was 10x larger in the precipitate. Since the precipitate is also smaller in cross-section than the superdome, the precipitate must contain a minimum of 10x more Mn atoms per volume than the quantum dot.

Ge is detected in the buried precipitate, while Si is found in the QD, indicating significant intermixing. Since the precipitate is immersed in Si, we cannot provide a direct measure of the overall stoichiometry, but a lower bound is estimated as 20 at.% Mn. This was achieved by estimating the thickness of the buried precipitate and the Si matrix surrounding it. Using the ratio between these two thicknesses, we then scale the Si peak obtained by the EDX accordingly. However, since the lowest Mn content of any equilibrium phase is 36%, it is likely that the QD and precipitate in Figure 4-3 (c) are truncated by the specimen edge, as shown in Figure 4-4, which would artificially reduce the apparent Mn:Si ratio. The composition of the QD can be directly determined as $Mn_{0.01}(Ge_{0.45}Si_{0.54})$ using the integrated K_α peaks.

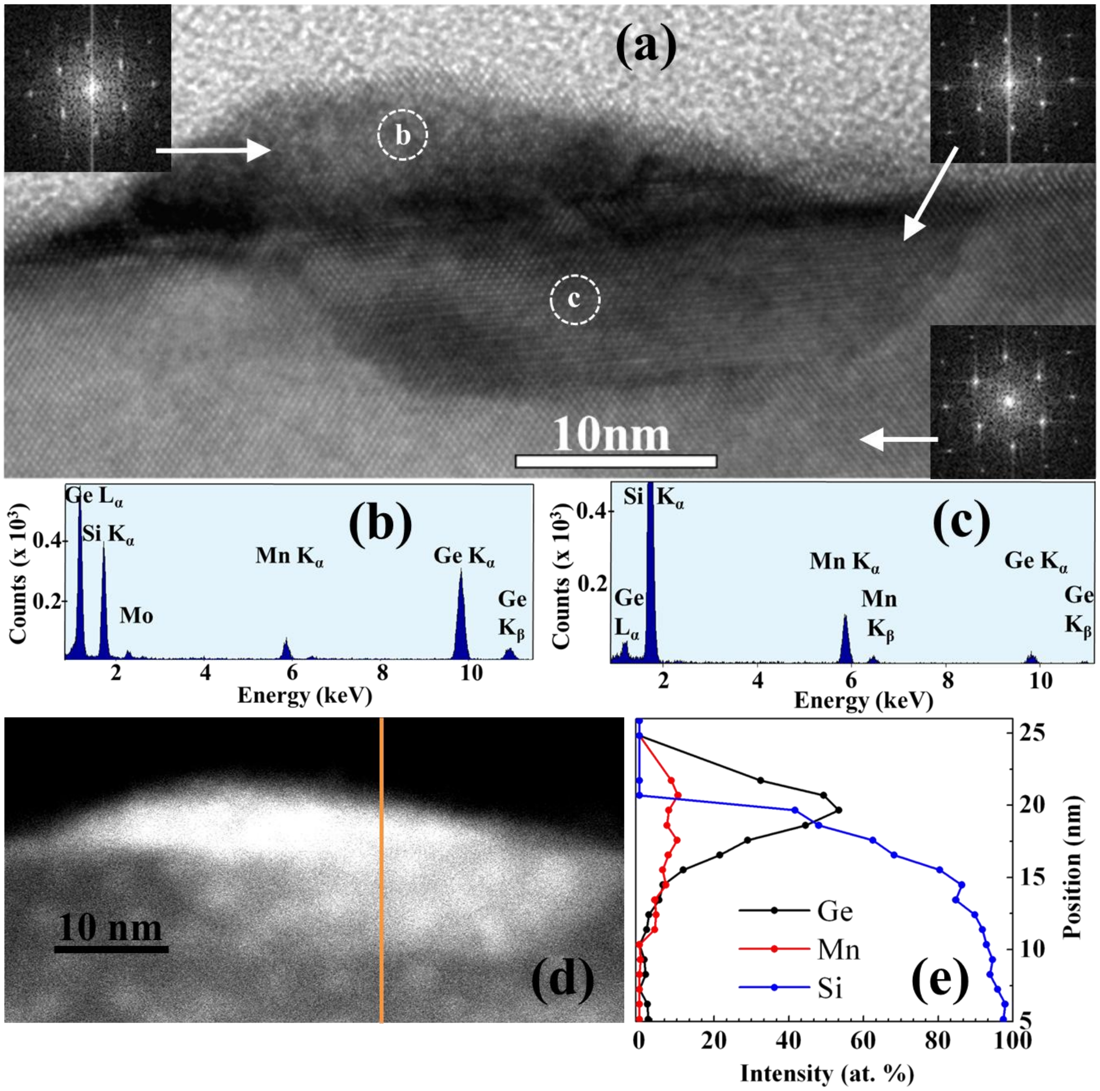

Figure 4-5. (a) BF TEM micrograph, along a [1-10] zone axis, of a dome and a solution phase cluster. Inset: FFT patterns of the Ge island, cluster and Si matrix. The 3 FFT patterns show diamond cubic crystal structure; (b) and (c) EDX point scans corresponding to point b and c in part (a) respectively; (d) HAADF-STEM micrographs with EDX line scan trace (orange line) quantified in (e).

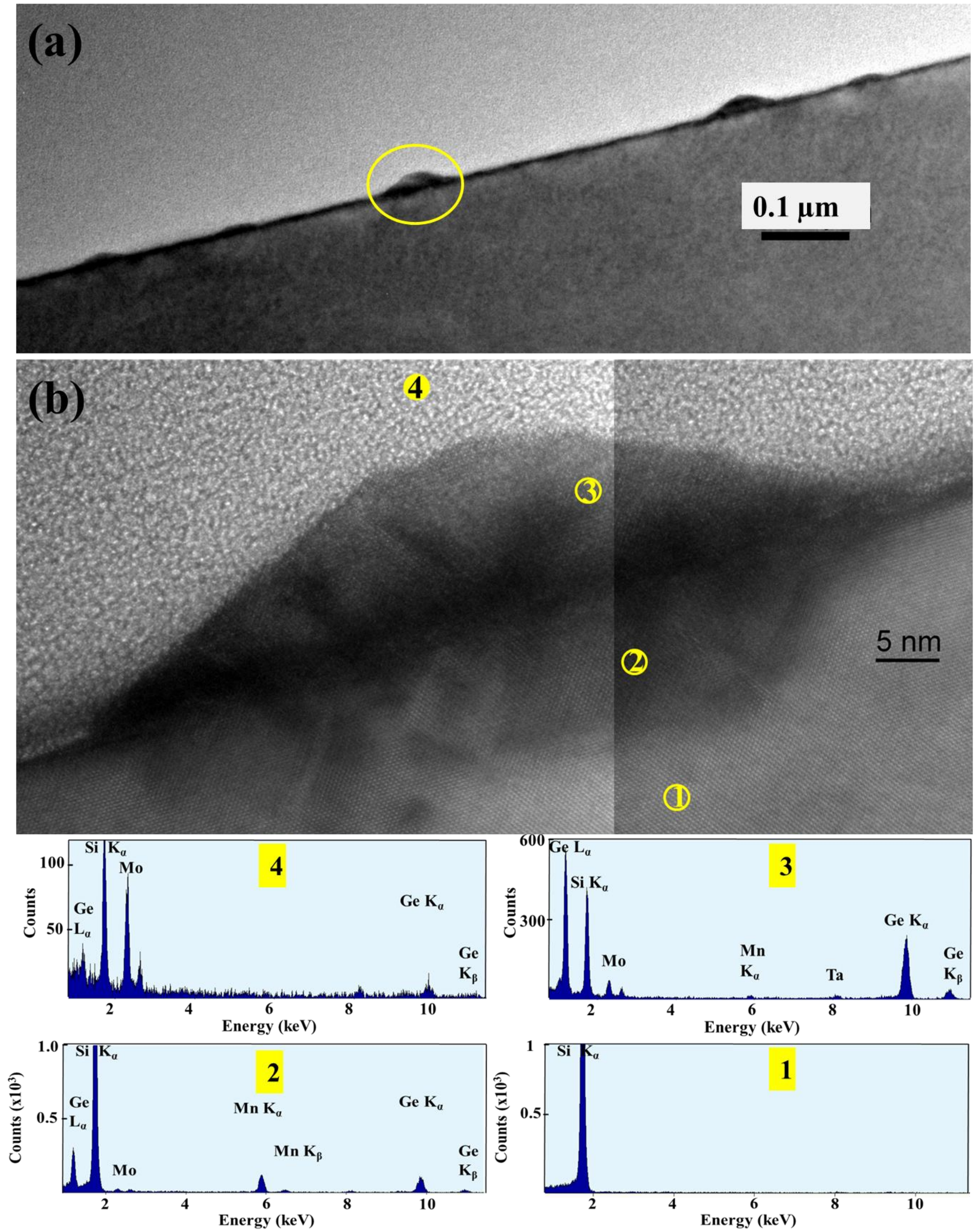

Figure 4-6. BF TEM (a) low magnification and (b) high resolution micrographs, along a [1-10] zone axis, of a dome and a solution phase cluster and EDX point scans corresponding to point 1, 2, 3 and 4 in the top image respectively.

A different class of buried structure is shown in Figure 4-5 and Figure 4-6 , where the cross-sectional shape typically presents as trapezoidal. The boundary between these structures and the Si matrix is more diffuse than the silicide precipitates. There is no evidence from TEM that these structures are anything other than diamond cubic, so we take these to be solution-phase clusters. We have examined 7 clusters in cross-section; 2 ± 1 second phase clusters and 4 ± 1 solution phase clusters). Although the statistics are poor, the solution-phase clusters are more prevalent than the precipitate clusters in this film. Composition was measured in this structure using high angle annular dark field microscopy-scanning transmission electron microscopy (HAADF-STEM, Figure 4-5 (d)), EDX point scans in TEM mode (Figure 4-5 (b) and (c)), and EDX line scans in scanning TEM mode (not shown). HAADF-STEM micrographs exhibit z-contrast, both the Ge QD and the buried solution cluster show enhanced intensities (note that the bright cluster-like features in Figure 4-5 (d) are artifacts). EDX point scans again show that the buried cluster has ≈ 3x larger Mn atom density than the dome. The latter has a point composition measured as $Mn_{0.05}(Ge_{0.54}Si_{0.41})_{0.95}$. Similar to the second phase clusters, we estimate the composition of the solution phase by scaling the Si peak using the ratio between the Si substrate and the Mn solution phase thicknesses. We estimate the an upper bound concentration of $Mn_{0.20}(Ge_{0.15}Si_{0.85})_{0.80}$.

A self-consistent picture begins to emerge with regard to the partitioning of Mn during Ge QD self-assembly on Si (001) via MBE co-deposition. At the 450 ºC growth temperature required to provide sufficient Ge mobility for QD formation, Mn is extremely mobile, both on the surface and in the bulk [116]. The inhomogeneous Ge layer is able to metastably dissolve 1.5% Mn in solution on average. The partitioning of

Mn amongst the various types of QDs and the Ge wetting layer has not been determined here, but the Mn content of the dots does not appear to be significantly higher than the average, suggesting a relatively homogenous distribution within the Ge layer. This is surprising given a strong tendency for Mn to undergo a spinodal-like decomposition on the 3-5 nm scale in Ge at much lower growth temperatures, forming highly-enriched nanoclusters [43], [45], [114]. Under the SD islands (only) we find buried structures that are highly enriched in Mn, suggesting the superdomes act to pump Mn into the substrate. The tendency for SD dots to provide a kinetic pathway for Mn entry into Si may arise from the highly inhomogeneous strain field, misfit dislocations, or the formation of exposed Si trenches around the dot perimeters [117]. In Figure 4-7 (a) and (b), HAADF STEM elucidate buried cluster growing into the SD. We observe fringing in the clusters in the BF micrographs, (a') and (b'), indicating that these are precipitates.

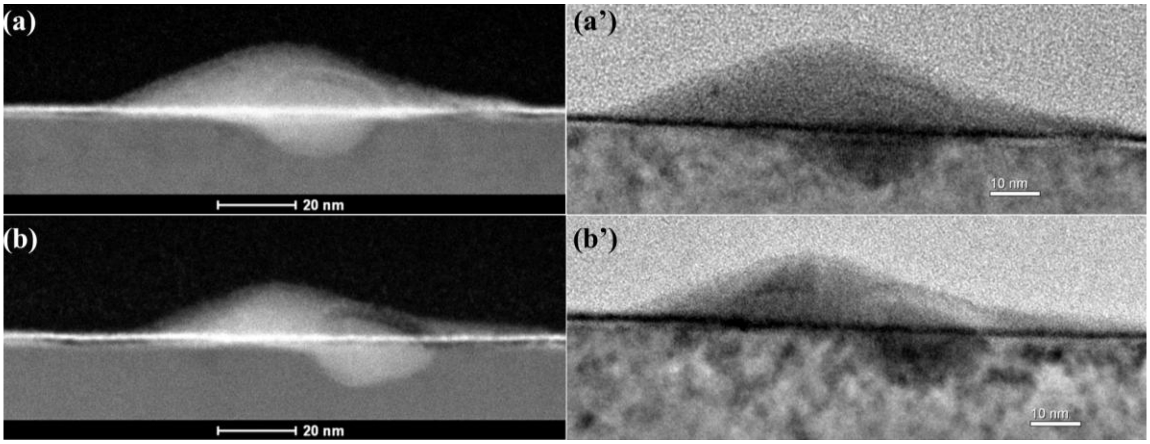

Figure 4-7. (a) and (b) HAADF – STEM images of islands with buried structures; (a') and (b') Corresponding BF TEM micrographs of (a) and (b) respectively.

Diamond cubic Mn-Si solution phases presumably form initially. These Mn enriched regions (of order 15% Mn) have interfaces that are diffuse on the atomic scale but are still much sharper than a simple diffusion source profile. In this regard, the formation of metastable, Mn-rich Si solutions does suggest a phase-separation process akin to spinodal decomposition. Then, when some critical local concentration is attained, nucleation of a crystallographically-distinct silicide phase can occur. Our experiments with similar Ge films having higher Mn contents than used here, reported in chapter 5, show that higher supersaturation drives copious silicide nucleation, followed by rapid precipitate growth both above and below the Si substrate. The precipitates quickly emerge from their host quantum dots to become relatively large rod-shaped or equiaxed silicide precipitates, while scavenging all the available Mn due to their lower chemical potential vis-à-vis the metastable solutions.

Magnetism

The total magnetic signal measured by the SQUID is the sum of the diamagnetic signal from the substrate, the ferromagnetic signal from (Ge,Mn) nanostructures and finally the paramagnetic signal from diluted Mn atoms. In order to obtain the magnetization curves due to the Mn, we perform the subtractions as discussed in chapter 3 (removing (a) a line of negative slope representing the Si diamagnetic susceptibility (b) Si paramagnetic signal at low temperatures), see Figure 3-9 (a).

Field dependent magnetization loops measured from 5 K to 300 K are shown in Figure 3-9 (b). For M(H) loops at 5 K, the best Langevin fit is obtained for moment per Bohr magneton, $\mu = 4.1 \pm 0.1\ \mu_B$, Figure 3-9 (b). Using the $M_s = 7.3\text{x}10^{-6}$ emu value obtained from Langevin fitting parameters, an average moment per Mn atom of 3 μ_B, and the area of the sample, we calculate the areal area density of the Mn atoms, n = 1.3 x 10^{15}

atoms/cm^2. This value is the 10x higher than that the areal density obtained via SIMS, 1.05 x 10^{-14} atoms/cm^2.

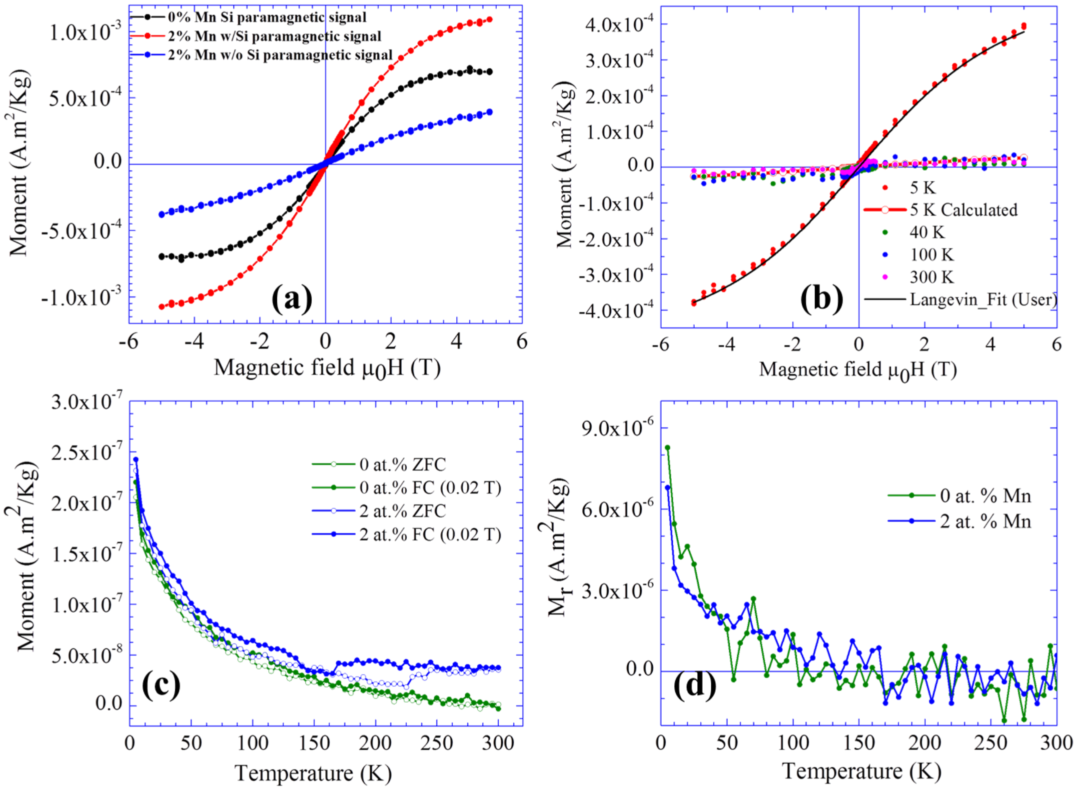

Figure 4-8. SQUID magnetism data. (a) M(H) curve showing the resultant 5K curve before and after Si paramagnetism subtraction (Si diamagnetism has already been subtracted in these curves); (b) M(H) from 5 to 300K. The 5K curve is fitted to a Langevin function (black line). Calculated M(H) loop expected at 5 K assuming that Mn atoms are all active with a 3 μ_B moment and are substitutionally incorporated in the matrix is also shown; (c) ZFCFC showing comparison between the 2% sample and the reference sample; (d) Remnant field at zero applied field showing a comparison between the 2% and reference sample.

This discrepancy may be due to substrate subtraction issues, associated with small sample-to-sample variability in the parasitic magnetism. We do not believe the issue arises from spurious magnetic contamination of the Ge:Mn films, since the impurity concentration would have to be ~ 7x that of Mn. EDX measurements did not detect any magnetic impurities at these levels in any of our measurements. Unfortunately, however, this issue precludes any detailed interpretation of the data in terms of magnetic response intrinsic to the Mn incorporation.

Figure 3-9 (c) shows the ZFC-FC plot of the 2% sample compared to the 0% reference sample. The 2% data is well-superimposed on the reference sample, suggesting any behavior intrinsic to the Mn is too weak to be observable (note that the superposition of the ZFC-FC curves in both samples suggests the absence of superparamagnetic phases, unless the blocking temperature is below 5 K). The only clear conclusion is that there is no high-temperature ferromagnetism, despite the presence of a dominant solution phase in the QDs.

Our growth conditions are quite similar to those used by Xiu et al. [9], although they did not directly measure the overall Mn content. Our resultant films are also quite similar to theirs, where both groups observed Mn solutions in Ge QDs and buried in Si regions immediately below the QDs. A few potentially important differences in our films relative to Xiu, et al., that could impact the magnetic properties include: (1) somewhat more dilute, homogeneous Mn contents in our Ge QDs; (2) significant intermixing of Si and Ge, leading to Mn-doped superdomes with approximately equimolar Ge:Si contents; and (3) nascent transformation of the Mn-Si solutions to Mn silicide phases. Issue (2) may be particularly important. For example, comparisons of magnetic behavior in amorphous Ge:Mn and Si:Mn films films shows that Mn tends to occupy interstitial-like positions in the latter, leading to enhanced p-d hybridization that quenches the local Mn moment [49], [74]. The extensive intermixing of Ge and Si we observe is surprising given the relatively low growth temperature of 450 ºC – intermixing in Ge QDs is usually considered negligible below 550 ºC [118]. This suggests that Mn may act as a surfactant, enhancing surface transport of both Ge and Si during self-assembly. The lack of Mn_5Ge_3 formation, which occurs readily for 200 °C MBE growth of Ge:Mn/Ge, is interesting. We believe this stems primarily from the Si reservoir, which forms a chemically-favorable sink for excess Mn, ultimately leading to preferred formation of silicides rather than germanides.

This work suggests the existence of a critical threshold below which all the Mn atoms are incorporated in the Ge matrix in solution form.

In conclusion, we have synthesized epitaxial self-assembled heteroepitaxial QD's by MBE co-deposition of nominal $Ge_{0.98}Mn_{0.02}$ films. The 2 at.% Mn has no perceptible effect on the QD's morphology. We show that 72 ± 6 % of the total deposited Mn atoms reside throughout the Ge layer, and there is significant Ge/Si intermixing in the dots. The balance of the Mn partitions into a sparse array of buried, Mn-rich regions that form directly underneath a subpopulation of the Ge QDs, schematically illustrated in Figure 4-9. These are solution phases, although some of these begin to transform to intermetallic silicide phases. Hence this sample represents the initial stages of Mn phase separation that will progress further with additional Mn, as shown in the next chapter (and in the AFM data of Chapter 3). Although spurious substrate subtraction issues mask any weak contributions from Mn, there is clearly an absence of any room temperature ferromagnetism.

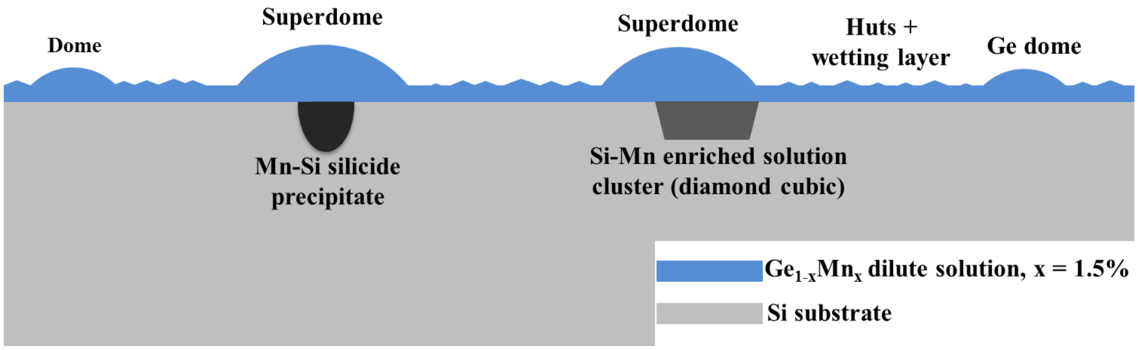

Figure 4-9. Schematic of the how Mn partitions in the Ge0.98Mn0.02 QD growth.

Chapter 5: Structure and Magnetism of Ternary Intermetallics

5.1 Introduction

This chapter provides a detailed TEM investigation of the $Ge_{1-x}Mn_x$ sample grown with the highest average Mn content, 10 at.%. We show that a variety of second phase precipitates arise by heterogeneous nucleation on quantum dots, and then serve to scavenge the Mn from the surrounding film. Ferromagnetism that persists to 220 K is observed, believed to result from the second phase precipitates rather than a DMS phase.

5.2 Experiment

The7.5 ML $Ge_{0.9}Mn_{0.1}$/Si (001) QD's were grown by MBE using magneton co-sputtering at similar condition to those described in chapter 4. Global Mn content in the film was determined by SIMS using Cs^+ ions at 5 keV and 60 ˚off-normal incidence. As described in chapter 4, the SIMS film was first capped with a nominal 100 nm amorphous Si to create steady-state sputtering conditions. The total Ge integrated over depth was 4.42×10^{15} at/cm^2 while Mn was 4.68×10^{14} at/cm^2, which gives a nominal composition of 10.6 at% Mn in Ge (but we show below that Mn partitions into the Si as well). In addition two independent, high-resolution Rutherford backscattering spectroscopy (RBS) measurements were performed as a complementary method to determine Mn content and Ge film thickness. Surface morphology was characterized *ex situ* using atomic force microscopy (AFM) in tapping mode. BF TEM, STEM and HAADF were employed for high-resolution spatial imaging and compositional analysis using EDX. Samples for TEM and STEM were prepared by standard wedge polishing techniques followed by Ar ion milling. An FEI Titan 80-300 kV S/TEM operating at 300 kV was used for STEM and high resolution TEM (HRTEM) imaging. Magnetic properties were measured using a superconducting quantum interference device (SQUID) with an external field parallel to the film plane. Again, the samples were cooled in maximum field (MFC) for the field dependent magnetization loops. Zero field cooled and field cooled (ZFC-FC) measurements were conducted. The sample is cooled down to 5 T without magnetic field followed by a weak field (0.02 T) is applied. The samples were carefully handled and stored to prevent spurious magnetic contamination.

5.3 Morphology

Figure 5-1 (a) shows the morphology of a control sample where strain-induced Ge quantum dots (QDs), huts, domes and superdomes, were grown with no added Mn flux (0 at.% Mn). With the addition of a Mn flux to obtain a composition of 10 at. %, these Ge pyramid and dome QDs are still observed in a film with 7.5 ML Ge as determined by RBS, see Figure 5-1(b). The QD size and density is similar to the Ge:Mn-0% case, but the pyramid islands in particular appear less well formed, in agreement with a recent scanning tunneling microscopy study [93]. New morphological features are also clearly observed in the Ge:Mn-10% sample, including lateral nanorods and more equiaxed nanoclusters that can be discerned from QDs by their asymmetric shapes, as illustrated in Figure 5-1 (b). We show below that these are intermetallic phases. Inspection of the AFM images shows there is a tendency for the intermetallic particles to be conjoined with Ge dome clusters. Equiaxed intermetallic nanoclusters are more common than rods, but both are present over extended regions of the sample.

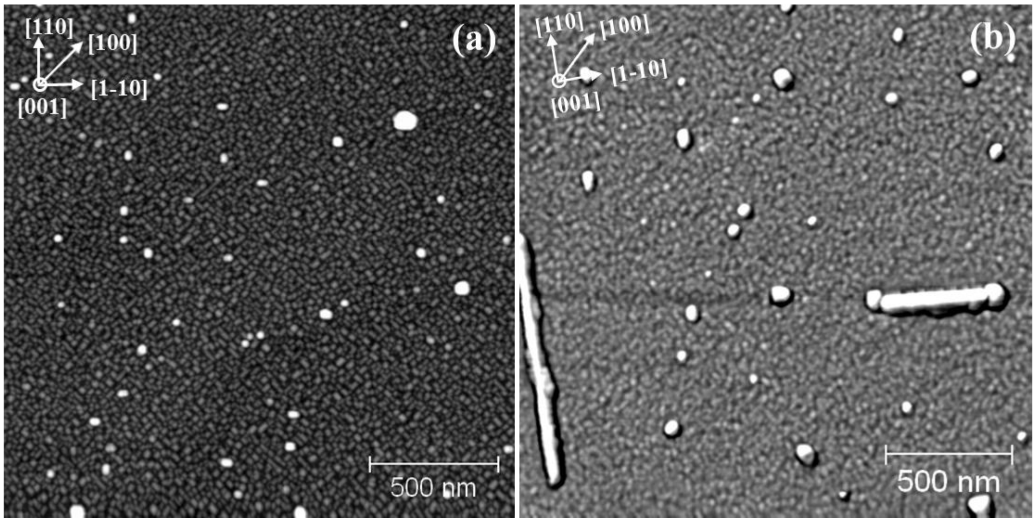

Figure 5-1. AFM images of 7.5 ML Mn_xGe_{1-x}/Si (001) grown at T_g = 450 ˚C. (a) x = 0. Scan shows the standard wetting layer-hut-dome-superdome dense array of ultra-small hut clusters with interspersed domes and superdomes; (b) x = 0.10. Scan shows nanorods and nanoclusters in addition to the standard QD morphology.

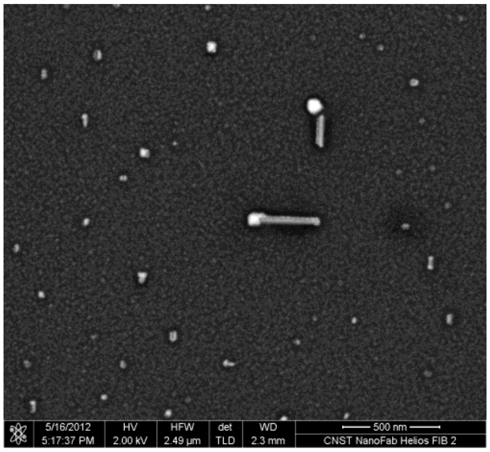

Figure 5-2. SEM showing denuded zones around the nanorods and nanoclusters. Image was image acquired at 2 keV, 100 pA using back scattered secondary electrons.

At larger AFM scan sizes, and SEM (Figure 5-2), it becomes apparent that the rods have a denuded zone about them where other intermetallic clusters do not form. The radius of these zones is of order 0.5 µm.

5.4 SIMS analysis

Figure 4-2 shows the distribution of Mn and Ge with depth in the film obtained from SIMS.

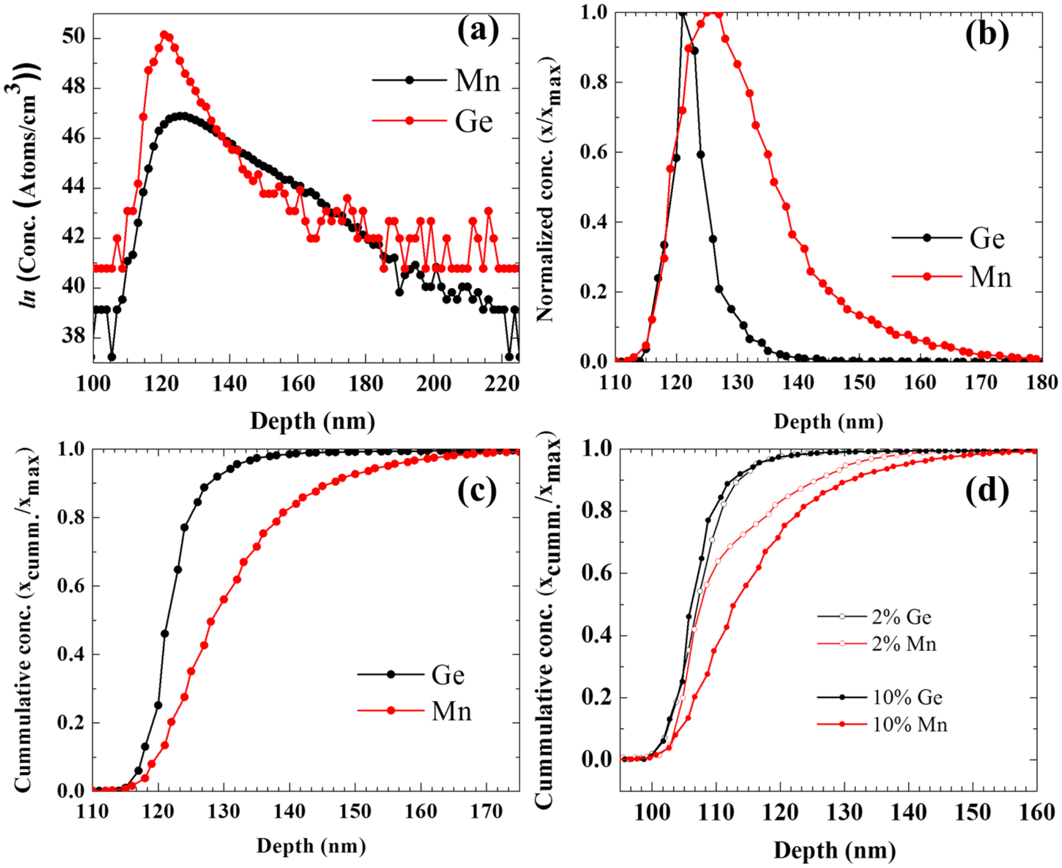

Figure 5-3. SIMS depth distribution profiles of Ge and Mn in the $Ge_{0.9}Mn_{0.1}$ QD's. (a) Raw data on a log scale; (b) normalized linear profiles; (c) cumulative profiles; (d) Comparison of the 2% and 10% cumulative profiles (the depth scale has been adjusted to simulated equal depths of Si capping layers).

From the Figure 4-2 b, we observe that the Mn peak is 5 nm deeper in the film than the Ge. In addition, the Ge and Mn peak widths (full-width half-maximum) in are 6 nm and 13 nm respectively. Applying the back of the Ge FWHM depth (~126 nm) on the cumulative plot (Figure 4-2 c), we clearly show that Mn extends well deep into the Si substrate. Moreover, this data indicates that 33% of the total Mn atoms are in the Ge layer. This represents a nominal concentration of 3.7% Mn in the Ge QD's. While this seems to suggest that the Mn is in the Ge QD's, we have many second phase particles protruding upwards to similar heights above the substrate. We will show later that most of the Mn actually resides in these second phase particles. Although the mass equivalent film thickness is only 1 nm, the quantum dots range in height, with SD islands typically being 10-14 nm high. Nanorods and nanocluster are 14 to 17 nm tall. The Mn profile extends further into the Si than Ge since it experiences a longer recoil path into the Si substrate in addition to the presence of buried Mn rich nanoclusters.

5.5 Structure

In Figure 5-4, cross-section transmission electron micrographs show typical Ge pyramid and dome islands. The islands are coherent to the substrate, and have sizes similar, but generally smaller, than those measured by AFM, indicating that tip convolution affects the AFM images.

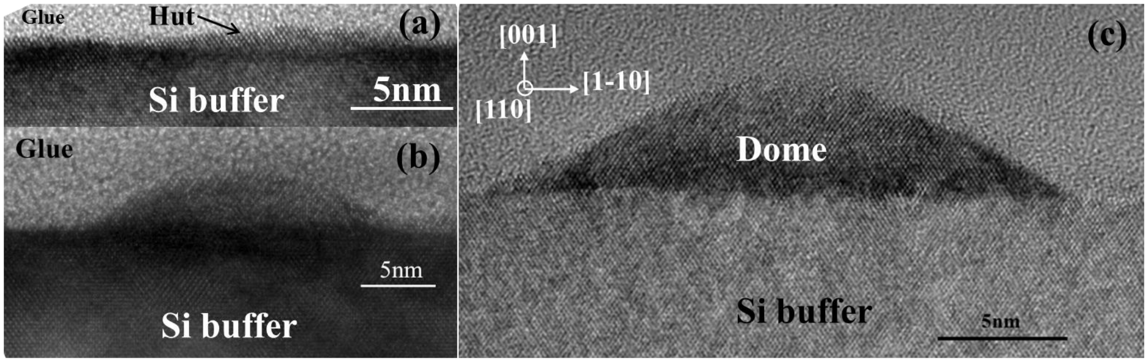

Figure 5-4. Bright field XHRTEM of the $Mn_{0.10}Ge_{0.90}$/Si (001), sample in the [1-10] zone axis showing typical huts (a) and coherent dome (b) and (c).

Figure 5-5 shows plan-view electron micrographs that elucidate the nanorod structure. In agreement with AFM, TEM confirms that nanorods can exhibit significant shape anisotropy, preferentially growing along the two <110> in-plane orientations of the

Si substrate. The nanorods have a typical 80 nm width, 15 nm height and 200 to 950 nm length. Moiré fringes along the axial direction of the rod are observed in Figure 5-5 (b), (c), (d) and in the high-resolution image Figure 5-5 (e). The broad Moiré fringes confirm that the Si substrate must still be present in the thinned specimen. Under appropriate imaging conditions, transverse Moiré fringes are also observed, but with a smaller spacing than the axial fringes, Figure 5-5 (d).

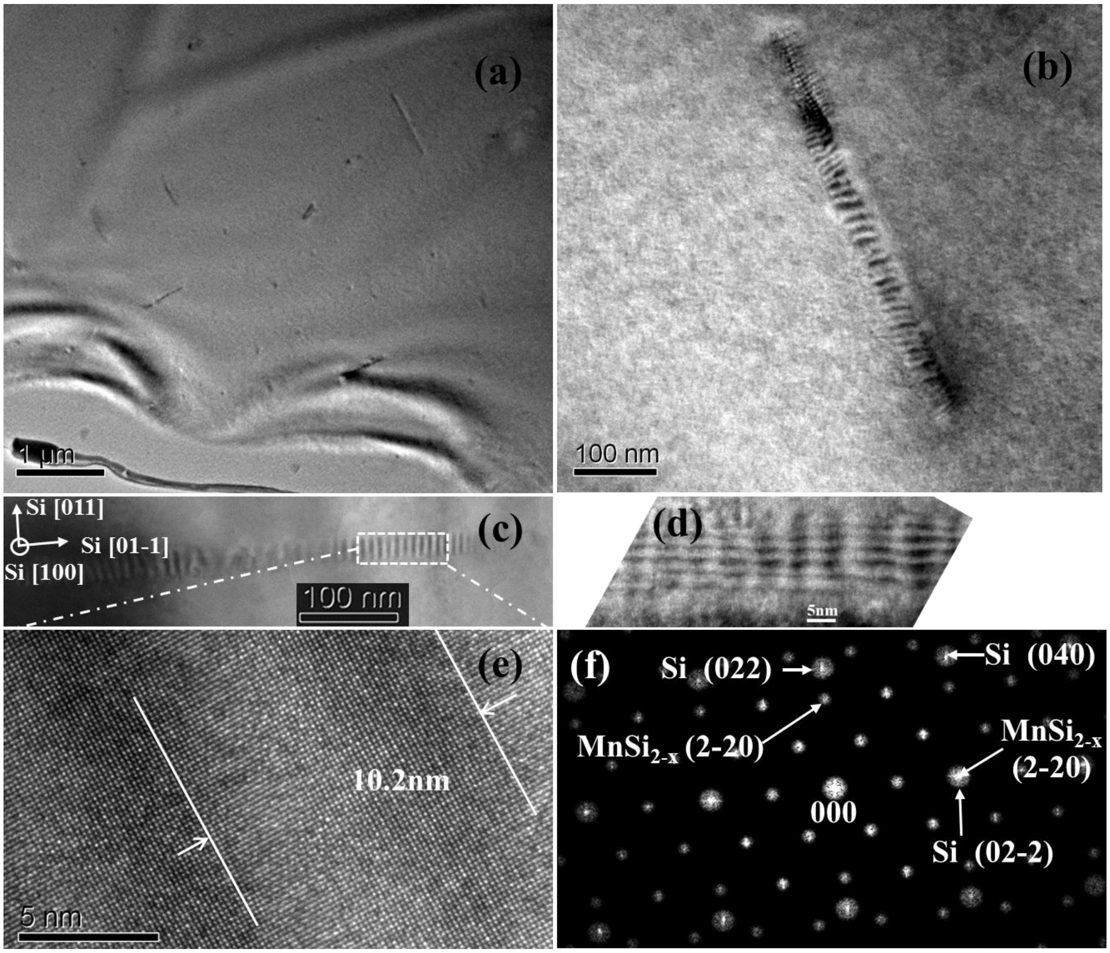

Figure 5-5. (a), (b), (c) and (d) Plan view BF TEM micrograph of nanorods in the Si [001] zone axis; (d) Micrograph showing a set of two orthogonal Moiré fringe; (e) High-resolution micrograph from the nanorod (c), where the Moiré spacing is indicated. (e) Corresponding FFT analysis of (e) with indexed reciprocal space of both Si and $MnSi_{2-x}$.

TEM demonstrates that the nanorods are monocrystalline and heteroepitaxial, supported by the fast fourier transform (FFT) shown in Figure 5-5 (f). Indexing of this pattern has proven to be challenging, and is discussed later in more detail.

EDX point scans along the rod indicate an apparent stoichiometry of about $Ge_{0.05}Mn_{0.95}$. The dichotomy between the structural assessment and the composition is likely accounted for by Si incorporation to form a Si-rich ternary silicide phase. In plan-view, it is difficult to quantify Si incorporation in the rod since signal from the Si substrate beneath the rod also contributes (we show below using cross-section below that ternaries do indeed form).

There are several morphological and structural variations of the equiaxed nanoclusters.

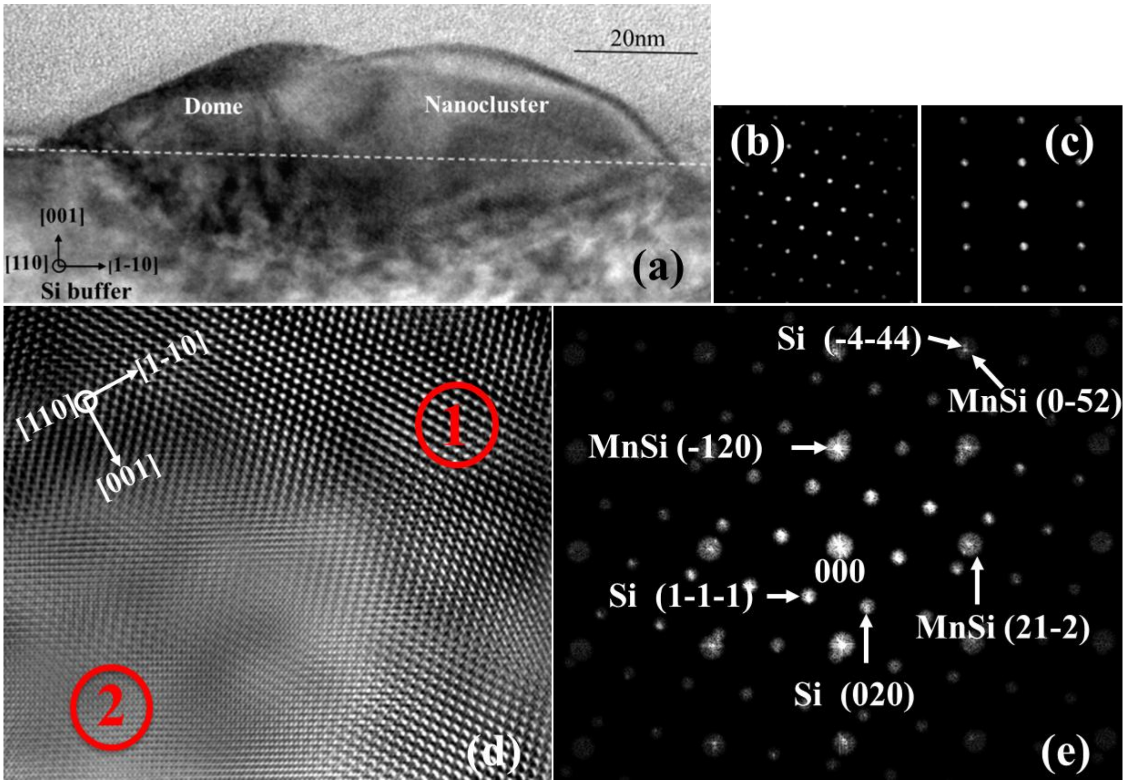

Figure 5-6. (a) Bright Field TEM micrograph of a nanocluster conjoined to a Ge dome; (b) FFT pattern of the dome area marked as 1 in (d), showing diamond cubic reciprocal space pattern

along a [1-10] zone axis; (c) FFT pattern of the B20 type nanocluster area marked as 1 in (d), along a [425] zone axis; (d) iFT of the boundary between the Ge dome and nanocluster from a central region in (a). Note the alignment of the axes when comparing to (a); (d) Indexing of the two superimposed reciprocal space patterns.

Figure 5-6 shows one example that has been analyzed in great detail. As shown in Figure 5-6 (a), the nanocluster extends into the Si subsurface region, and also is intimately conjoined with a Ge dome island. Figure 5-6 (b) shows the internal interface at high resolution between the Ge dome and the nanocluster. There is an abrupt interface termination between the diamond cubic structures and the nanocluster. The FFT of the high resolution image is shown in Figure 5-6 (c), and is well-matched by the MnSi cubic B20 structure with a P-213 (198) space group, viewed, along a [425] zone axis that is parallel to the Si [110] zone axis. The MnSi (0 -5 2) and Si (-4-44) are parallel with a 7% misfit, hence the orientation relation is MnSi (0 -5 2)/[425] || Si (-1-11)/[110].

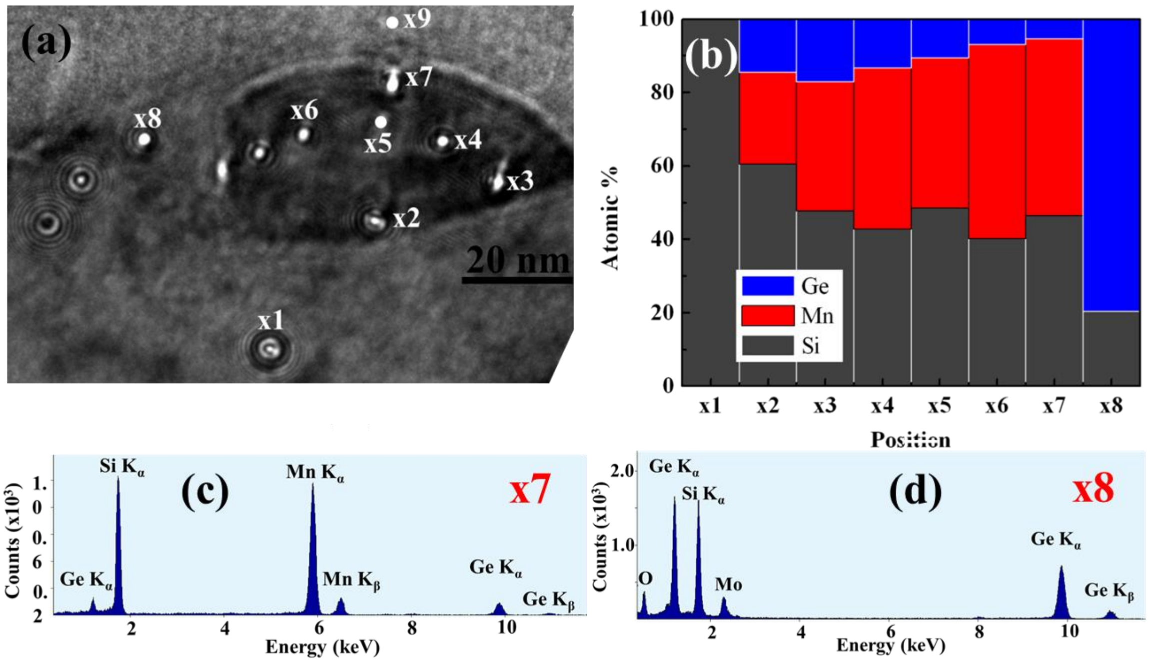

Figure 5-7. (a) BF TEM micrograph of B20 type nanocluster showing EDX nanoprobe locations; (b) Compound histogram summarizing the point concentration measurements across the nanocluster; (c) EDX point scan taken at point x7 in (a) indicating a ternary composition; (d) EDX point scan taken at point x8 (Ge dome); no Mn is detected.

EDX analysis was performed using a ~2 nm point probe mode at different locations on the conjoined feature, shown in Figure 5-7. EDX performed in the diamond cubic substrate region below the composite structure (point x1) detects only Si. Similarly, EDX point analysis in the region identified as a diamond cubic Ge dome-shaped QD (x8) detects Ge, but no Mn. Mn was clearly detected in the B29 nanocluster, as shown in Figure 5-7 (c). In the upper portion of the cluster that projects above the Si substrate, the Mn concentration ranges from 50 - 60 at.%, although the exact value is sensitive to background subtraction of Si that was sputter-redeposited on the glue surface during in milling of the TEM specimen. Hence EDX is consistent with identification of a B20 structure with a composition $Mn(Ge_xSi_{1-x})$, where $x = 0.30 \pm 0.03$.In the cluster region below the Si substrate surface, Mn is only 28%, inconsistent with the MnSi phase, but this suggests that the buried region does not extend throughout the thickness of the TEM specimen (i.e., there is pure Si along the beam path through the thinned specimen). To further confirm this hypothesis, we observe a constant Mn K_α count across the cluster from the glue to the Si substrate.

Figure 5-8 shows plan-view TEM micrographs of another cluster that exhibits extraordinary fringing, as highlighted in the high-resolution micrograph of Figure 5-8 (b). This fringing, both in form and spacing, is characteristic of the “Nowotny chimney ladder” (NCL) phases [119] associated with $MnSi_{2-x}$ compounds, in which the fringes arise from interference between the incommensurate Mn and Si sublattices. $MnSi_{2-x}$ is a tetragonal structure with a P-4c2 (116) space group. This phase will be discussed in further details in the discussion section. The corresponding FFT, obtained from the higher resolution image in Figure 5-8 (b), can be indexed to the Mn_4Si_7 phase with an orientation relation $Mn_4(Ge_ySi_{1-y})_7$ (11-8)/[110] || Si (022)/[001]. The $Mn_4(Ge_ySi_{1-y})_7$ (11-8) and Si (022) planes are parallel with a 1% misfit.

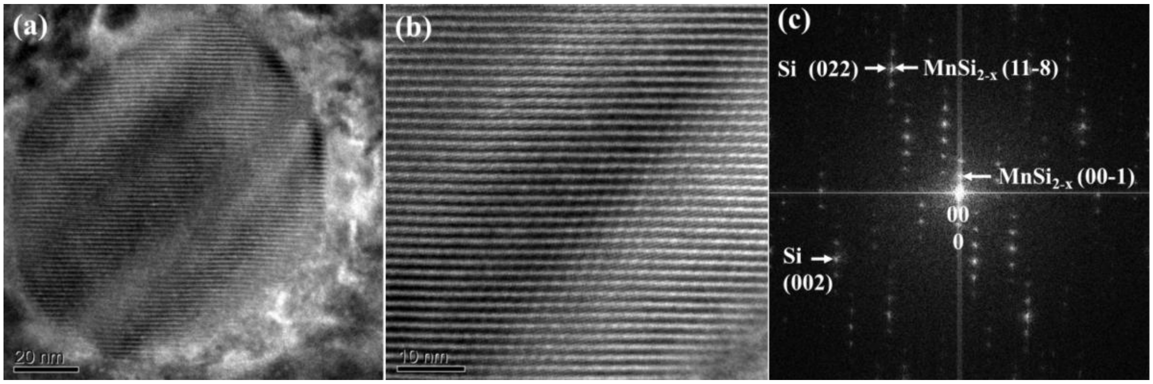

Figure 5-8. (a) Plan-view TEM micrograph of a $MnSi_{2-x}$ cluster showing strong fringing viewed on a Si [001] zone axis; (b) HRTEM of the nanocluster (fringe pitch of 1.62nm); (c) FFT pattern of (b).

Figure 5-9 show various second phase precipitate nanoclusters heterogeneously nucleated next to Ge domes. We propose that the Ge QDs nucleated before the nanoclusters as shall be highlighted in chapter 6.

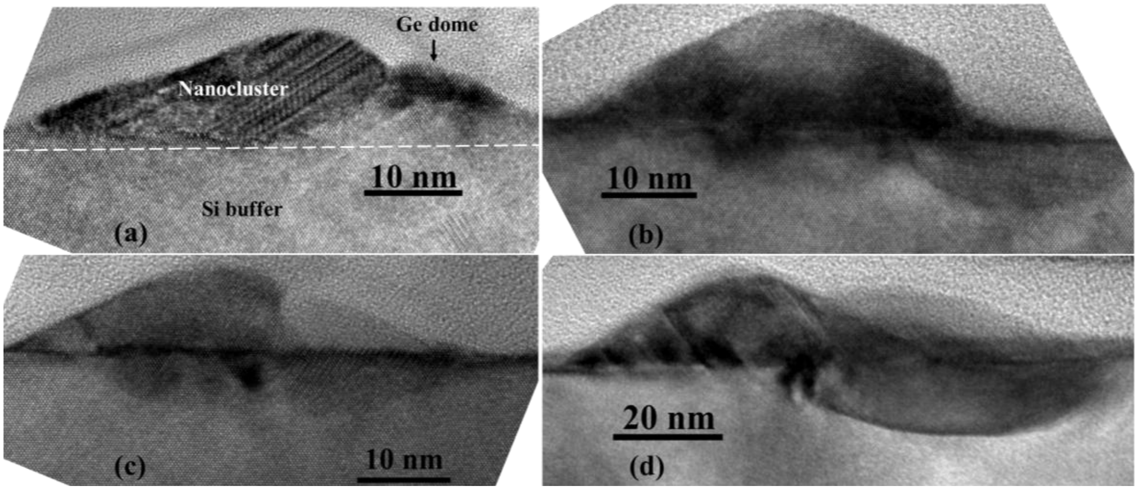

Figure 5-9. BF HRXTEM of nanoclusters heterogeneously nucleated next to a Ge islands in cross section along the Si [1-10] zone axis. Islands (b) and (d) are consistent with our interpretation of Mn partitions into buried Mn rich structures in the 2% sample (chapter 4).

5.6 Magnetism

Field dependent magnetization loops measured from 5 K to 300 K are shown in Figure 5-10 (a) to (d). Figure 5-10 (a) demonstrates the subtraction as described the Eqn. 3-1. Figure 5-10 (b) shows a ferromagnetic signal that persists beyond 300 K. We proceed and subtract this ferromagnetic signal from all the data (5 K – 300 K) in order to observe the resultant magnetic signal due to other phase that may be in the film, Figure 5-10 (c). The satutation moment in Bohr magneton is calculated to be equal to 6.7 ± 0.1 at 5K using the Langevin function, Figure 5-10 (c). In addition, we calculate the Mn level to be equal to 2.1 x 10^{15} atoms/cm^2. This Mn levels is 4x higher than that reported by SIMS. Figure 5-10 (b), (c) and (d) show the calculated M(H) loop expected at 5 K assuming that Mn atoms are all active with a 3 μ_B moment and are substitutionally incorporated in the matrix is also shown.

The 4x higher moment observed in the SQUID data may be super-moments due to Mn superparamagnetic particles that have a blocking temperature below our minimum measured temperature, 5 K.

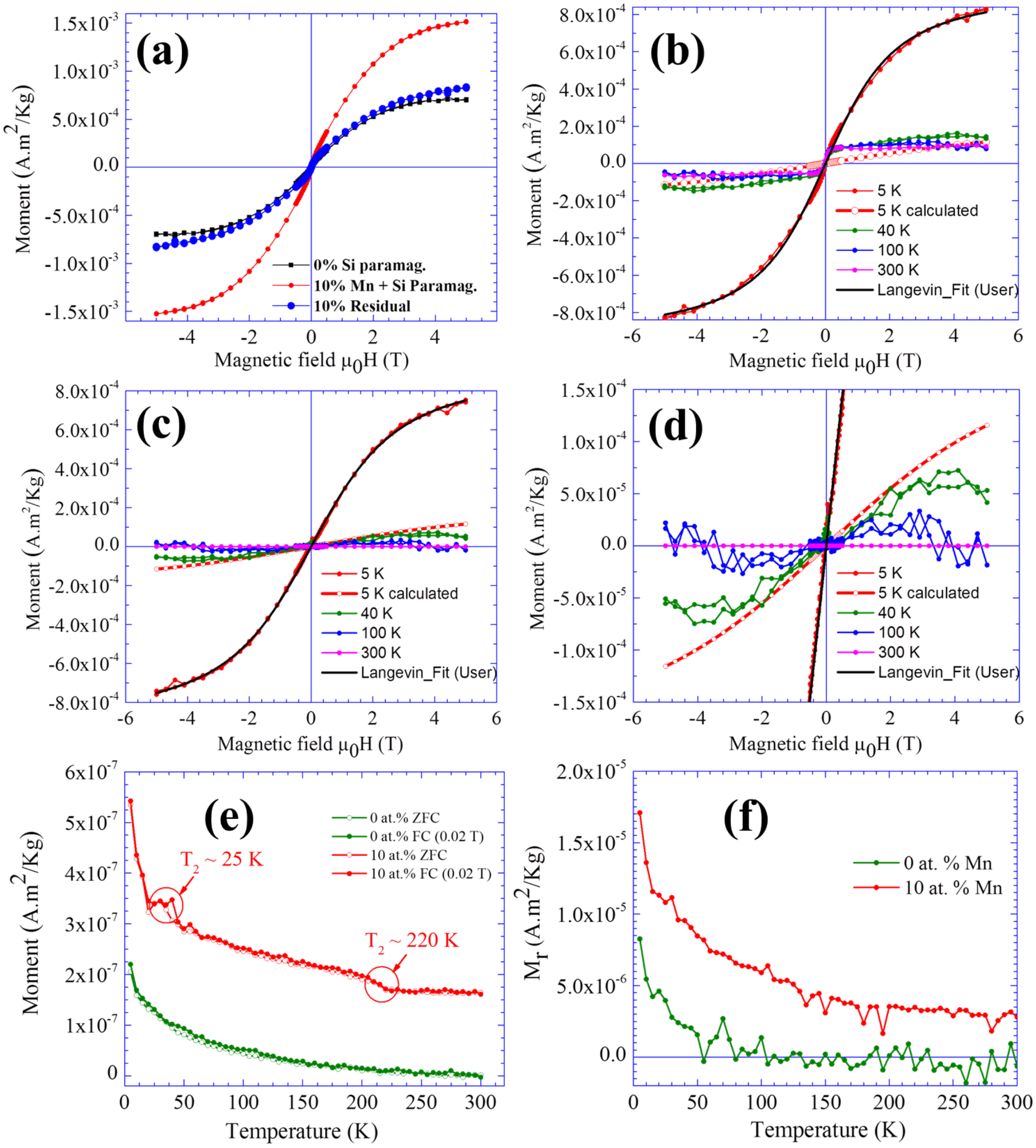

Figure 5-10. (a) M(H) curve showing the resultant 5K curve before and after Si paramagnetism subtraction (Si diamagnetism has already been subtracted) ; (b) M(H) from 5 to 300 K showing a ferromagnetic signal persistent to 300 K. (c) M(H) from 5 to 300 K after subtraction of the 300 K ferromagnetic signal. The 5 K curve is fitted to a Langevin function (black line); (d) High resolution of (c); (e) Contrast between the ZFC-FC curves of the 10% and the reference sample. Two characteristic temperatures at 25 K and 220 K are evident; (d) Remnant field curves of the vs T for the 0, 2, and 10% and reference sample.

Figure 5-10 (e) shows ZFC-FC curves obtained at 200 Oe. The ZFC and FC curves superimpose down to 5 K. There is clear evidence of two magnetic phases, a paramagnetic phase with T_c at 25 K and a ferromagnetic phase with a T_c at 220 K. Similar behavior is observed in $M_r(T)$, which additionally is consistent with this phase being ferromagnetic. There could be a third phase responsible for the > 300 K magnetization. With the current data set, we have no way to conclusively establish the origin of this signal. It may be an intrinsic signal due to Mn second phase, spurious contamination, or large nanoparticles in the substrate. If this were a third phase, we observe above room temperature ferromagnetic. This is speculative at best. As will be mentioned in the future work, better subtraction techniques will help us understand this data better.

5.7 Discussion

We grew strained heteroepitaxial Ge-10%Mn films by co-deposition on Si (001) at 450 ^{o}C, conditions that produce Ge quantum dots in the absence of Mn. Indeed it is observed that QD morphologies typical for pure Ge on Si are still obtained in the presence of 10% Mn. However, the large relative Mn flux leads to a significant areal density of additional structures that are second phase precipitates as identified by TEM imaging plus diffraction, and local chemical analysis.

Comparisons of the crystal structures obtained vs. the nominal Mn:Ge ratio indicate that the films are actually ternary alloys, with considerably more Si than Ge in the compound, i.e., the compounds are dominantly silicides. This is supported both by direct EDX measurement in cross-section, and by the observation that some intermetallic particles extend down into the Si substrate. In what follows, we discuss the alloying, the phases and epitaxial orientation relationships observed, the morphologies, and the magnetism.

Ternary Compound Formation: The formation of phases with ternary $Mn_x(Si_yGe_{1-y})_z$ compositions is driven by the chemical reactivity of Mn with both Ge and Si, the large Si reservoir, and the relatively elevated growth temperature that promotes high Mn mobility, both on the surface and in the bulk. The MnSi and $MnSi_{2-x}$ archetypal phases we observe are not present on the Ge-Mn phase diagram, but our results suggest a significant solubility of Ge on the Si sublattice, at least for the MnSi phase, where about 30% of the Si atoms are replaced by Ge. The hexagonal $D8_8$ phase is present on both the Ge-Mn and Ge-Si phase diagrams, and a full range of soluble pseudobinary $D8_8$ alloys have been synthesized in bulk [120]. However, we have not definitively observed this phase, despite its common occurrence during MBE growth of Ge:Mn/Ge (001). Perhaps over simplistically, this can be ascribed to a tendency to form the more Si rich phases first.

The prominent rods we observe in TEM and AFM have been difficult to index. The FFT diffractogram shown in Figure 5-5 (f) is well-resolved, and we have compared this FFT with zone axis patterns from all the know Mn-Si and Mn-Ge phases. Best correspondences are with the Mn_4Si_7-[311] zone axis, and Mn_5Si_3-[1121] zone axis. In the former case, the interplanar spacing match well, but the interplanar angles are off by 5º, whereas in the latter case, the interplanar angles match well, but the interplanar spacing are off by 10%. It seems unlikely that ternary incorporation of Ge and Si on a single sublattice can produce such large distortions in either the spacings or the angles; similarly, the distortions require epitaxial strains of 8-12%, which seem too large to be supported elastically in structures of this size. In this film we have not definitively identified a rod in cross-section for both structure and composition measurement, hence we cannot resolve the indexing at this time.

However, considerations of Mn capture during growth lend further insight into the rod structure and growth kinetics. For the large rod shown Figure 5-1 (b), we can estimate the size of the Mn capture zone required to provide the Mn atoms needed by any given phase, given the rod volume and amount of Mn deposited per area. The Mn fraction in the rod is given by

$$x_{Mn} = \frac{A_{CZ} N_{Mn}}{V_r N_{phase}} \qquad \text{5-2}$$

where the numerator represents the total Mn atoms in the capture zone while the denominator is the total number of atoms (Mn, Ge and Si) in the rod. A_{CZ} is the capture zone area, N_{Mn} is the deposited Mn atoms/area, V_r is the measured rod volume, and N_{phase} is the number of atoms per volume associated with the rod phase. For example, for the chimney ladder phase Mn_4Si_7, $N_{phase} = 82.5$ atoms/nm^3 (we assume here that Ge is substitution on the Si sublattice does not affect the lattice parameters much) and $x_{Mn} = 0.36$. For Mn_5Si_3, $N_{phase} = 80$ atoms/nm^3 and $x_{Mn} = 0.625$. From AFM, $V_r = 5.6 \times 10^5$ nm^3 and we know from SIMS that $N_{Mn} = 4.7 \times 10^{15}$ cm^{-2}. We then can solve Eq. (1) for A_{CZ}. We further assume a capture zone perimeter defined by a *constant normal distance* to the rod. Using rothis, we find that for an assumed $MnSi_{2-x}$ phase, the capture zone areas around neighboring rods barely overlap. On the other hand, for Mn_5Si_3, the required capture zone areas are 1.72x larger, and there is significant overlap between neighboring rods, which is unphysical. <u>This argues for the rods being $MnSi_{2-x}$, i.e., the</u>

most Mn-poor phase. This analysis also provides an estimate of the maximum diffusion length on the surface, 750 nm. It also suggests that the rods do not penetrate much into the underlying substrate, which would then require a larger Mn capture zone. In separate experiments under different growth conditions that will be reported in chapter 6, where extensive rod formation is observed, cross-section TEM of a rod has been obtained, showing a structure only above the Si substrate and indexed to $MnSi_{2-x}$.

At the same time, the rods clearly exhibit a surrounding area that is denuded of Ge dome islands, but not Ge huts. We presume that the missing Ge is taken up by the rod in its ternary composition. To verify this, for the same rod analyzed above, we can identify and measure the area of an elliptical denuded zone, and an analysis similar to Eq. 1 is then performed:

$$x_{Ge} = \frac{A_{DZ}\Delta N_{Ge}}{V_r N_{phase}} \qquad \text{5-3}$$

where the terms are as defined above, except that ΔN_{Ge} represents the effective amount of Ge in the denuded zone (DZ) scavenged by the rod. Although our plan-view EDX measurements cannot quantify the Si in the rod, they do reliably show that the ratio of Mn:Ge along the rod is about 24. Hence, if $x_{Mn} = 0.36$ for the chimney ladder phase, then $x_{Ge} = 0.015$. Measuring $A_{DZ} = 1.5E6\ nm^2$ for the large rod under discussion, we can solve for N_{Ge} , which gives $N_{Ge} = 0.07$ ML, that is, over the denuded zone area, only 7% of a single Ge monolayer has been scavenged into the nanorod. This is much too small to produce the complete suppression of domes and superdomes, which would require scavenging 1-2 ML of the 7.3 ML thick Ge film. This then motivates the question of why Ge dome formation is suppressed over such a large area surrounding the rods and clusters.

The answer to this question may be tied to an additional question: where does the Si come from to supply the formation of the rod? For the $MnSi_{2-x}$ NCL phase, the Si *cannot come from below*. The reasoning is as follows: the density of Si atoms in the NCL crystal structure is 51 Si atoms/nm^3. The density of Si in diamond cubic Si is 50 Si/nm^3. If the Si comes from below, the rod would end up perfectly buried in the Si substrate, with no protruding region! Hence the Si must come from regions beyond the rod perimeter. We suggest that the high concentration of Mn flowing to the rod to support its growth also must liberate Si from underneath the Ge wetting layer to provide an equivalent, but twice as large, flow, to support the rod stoichiometry. As a result, local intermixing of Ge and Si is occurring that reduces the strain in the regions adjacent to the rods by forming a SiGe alloy, thereby reducing the elastic driving force for dome formation.

Consistent with this view, for the MnSi precipitate shown in Figure 5-7, XTEM more clearly shows the distribution of Mn, Ge and Si through the depth of the feature. The profile across the depth of the structure shows that Mn, Ge and Si are dispersed across the entire structure, which suggests there is not only mobility of Mn itself, but that Ge and Si are intermixing as well.

The conjoined nature of both the nanorods and nanoclusters to Ge domes suggest a heterogeneous nucleation mechanism. As pointed out in Chapter 4, it is not clear whether Ge domes nucleate on buried Si-rich region or vice versa. It is clear that when these regions transform to the monosilicide MnSi, they can then grow up and out of the Ge dome to become exposed on the free surface, in the process taking up Ge into the Si sublattice. On the other hand, the tendency of rods to suppress dome formation locally while at the same time being attached to a dome, suggests that the dome formed first, then the rod nucleated on the dome and proceeded to grow out laterally across the surface.

<u>Epitaxial Orientations and Precipitate Morphologies</u>: The nanorod structures are clearly epitaxial with respect to the substrate, elongating along either the [110] or [1-10] in-plane directions of the Si. It has been argued here that these rods are the $MnSi_{2-x}$ Nowotny chimney ladder (NCL) archetype, although the FFT diffraction pattern match is not exact. In this case, the epitaxial orientation relation (OR) is $Mn(Ge_ySi_{1-y})_{2-x}$ (01-1)/[311] || Si (01-1)/[001]. The ~ 2% mismatch between Si (02-2) and Mn_4Si_7 (2-20), gives rise to a set of translational Moiré fringes as shown in Figure 5-5 (b). The spacing between translational Moiré, D, is given by

$$D = \frac{d_1 d_2}{|d_1 - d_2|} \qquad 5\text{-}4$$

where d_1 and d_2 are the spacing between the Si and nanorod respectively. Using the known $Si_{(022)}$ d spacing of 1.92 Å and the know D value form the plan view micrograph obtained by averaging ten Moiré spacing, the nanorod should have a d spacing of 1.955Å. This is in good agreement with $d_{(2\text{-}20)}$ of Mn_4Si_7 = 1.954 Å. Nanorods exhibit a remarkable shape anisotropy and preferential growth along the two <110> in-plane orientations of the Si substrate. This growth anisotropy has been ascribed previously to anisotropy in the lattice misfit in different directions within the heterointerface [22]. We calculate there is a 2% misfit along the length of the rod and a 10% misfit in the orthogonal direction (between Si (066) and Mn_4Si_7 (44-24). To minimize the strain energy, the rod experiences a rapid growth in the less strained axis and limited growth in the more strain axis.

$MnSi_{2-x}$

$MnSi_{2-x}$, with x ~0.25, also known as the Nowotny chimney ladder (NCL) phase, represents a group of manganese silicides, Mn_nSi_m, with m/n 1.73 - 1.75 (see Figure 5-11). The $MnSi_{2-x}$ has several phases with slightly different stoichiometry that are all characterized by unusually long c lattice parameter that varies widely with the composition. The corresponding unit cells of two NCL variants are shown in Figure 5-11 below. These structures comprise of Mn and Si sub-lattices that are generally incommensurate. The Mn atoms form chimneys within which Si atoms rise in a spiral ladder pattern. The long c axis is due to the mismatch between the Mn and Si sub-lattices in the c-axis of the unit cell.

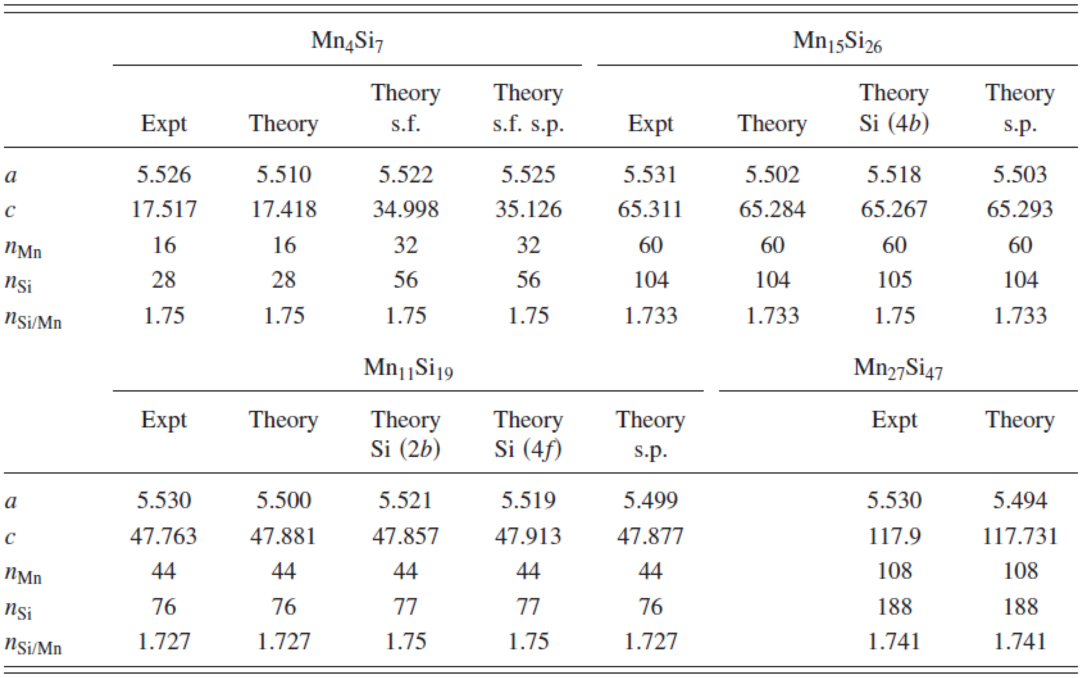

	Mn_4Si_7				$Mn_{15}Si_{26}$			
	Expt	Theory	Theory s.f.	Theory s.f. s.p.	Expt	Theory	Theory Si (4*b*)	Theory s.p.
a	5.526	5.510	5.522	5.525	5.531	5.502	5.518	5.503
c	17.517	17.418	34.998	35.126	65.311	65.284	65.267	65.293
n_{Mn}	16	16	32	32	60	60	60	60
n_{Si}	28	28	56	56	104	104	105	104
$n_{Si/Mn}$	1.75	1.75	1.75	1.75	1.733	1.733	1.75	1.733

	$Mn_{11}Si_{19}$					$Mn_{27}Si_{47}$	
	Expt	Theory	Theory Si (2*b*)	Theory Si (4*f*)	Theory s.p.	Expt	Theory
a	5.530	5.500	5.521	5.519	5.499	5.530	5.494
c	47.763	47.881	47.857	47.913	47.877	117.9	117.731
n_{Mn}	44	44	44	44	44	108	108
n_{Si}	76	76	77	77	76	188	188
$n_{Si/Mn}$	1.727	1.727	1.75	1.75	1.727	1.741	1.741

Figure 5-11: Experimental and theoretical lattice parameters a and c in Å, the number of Mn (n_{Mn}) and Si (n_{Si}) atoms in the unit cell, and the stoichiometry ($n_{Si/Mn}$) of different phases of HMS. The s.f. and s.p. stand for the stacking fault and spin-polarized cases, while 2b, 4f, and 4b indicate the Wyckoff position of the Si adatom in the unit cell.

One can obtain the c lattice parameter using $c = nc_{Mn}$, where n is an integer representing the number of Mn subcells in the unit cell and c_{Mn} is the Mn subcell length in the c-direction = 4.37 Å. It is hard to experimentally distinguish between different NCL phases [121]. Since the unit cell is the smallest unit for the structures, Mn_4Si_7 is often taken as a reasonable representation for the structures of $MnSi_{1.75}$

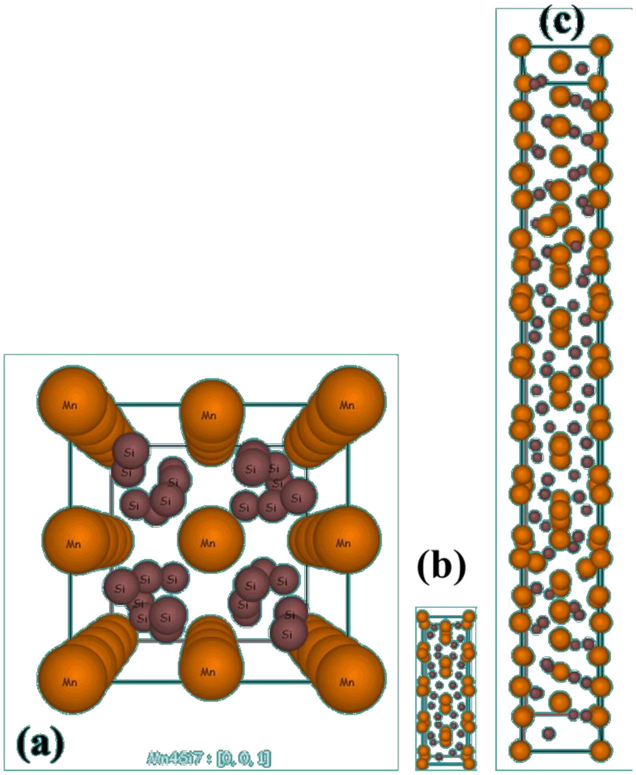

Figure 5-12. Unit cell structures of two of the $MnSi_{1.75}$ phases. Mn_4Si_7 viewed along (a) [001] and (b) [100]; (c) $Mn_{11}Si_{19}$ viewed along [100].

<u>Magnetism of phases observed:</u>

Bulk **Mn_4Si_7** was reported to be a weak itinerant magnetic system displaying the saturation magnetization of 0.012 μB/Mn below $T_c = 40$ K . Recently, it has been suggested that manganese silicide $MnSi_{1.75}$ nanoparticles synthesized by Mn implantation on Si (001) followed by rapid thermal annealing at 800 ˚C for 5 minutes showed ferromagnetism with a relatively large magnetic moment of 0.21μ_B [122], much larger than the bulk counterpart [123]. Moreover, Yabuuchi et al. also reported a saturation magnetization of the order of 0.1 μ_B [124] observed in Mn^+ ions implanted into a p-type Si (100) wafer and annealed at 700 to 800 ˚C. They attribute this moment to presumably be due to $MnSi_{1.75}$ nanoparticles. It has been argued in detail that local bond disorder can explain this variation in saturation magnetization between bulk and nanoparticle [125].

MnSi is an intermetallic compound with a B20 structure and P213 space group (198). Its cubic unit cell has a lattice parameter of a = 4.556 Å with four Mn and four Si atoms.

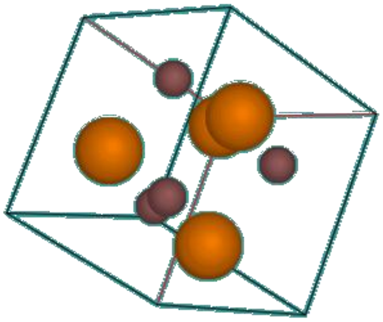

Figure 5-13: Unit cell of a MnSi. It's a B20 structure with a lattice parameter of a = 4.556 Å. The large spheres represent Mn atoms and the small ones represent Si atoms.

MnSi has been reported MnSi to be a weak itinerant ferromagnet with a $T_c = 29.1$ K, where there is a paramagnetic to helicoidal order transition [126]. This critical temperature was shown to be decrease with pressure. At pressures greater than 15 Kbar, there was no magnetic ordering observed [127]. In its paramagnetic state, MnSi has a saturation moment of 0.4 μ_B/Mn at 4.2 K [128].

The ferromagnetic transition we observe in the 10% Mn sample at 220 K does not have a simple correspondence to either $MnSi_{2-x}$ or MnSi. However, bond disorder (which affects hybridization and localization), the Ge substitution (which tends to favor ferromagnetic coupling), and strain (which affects exchange coupling) could play a significant role is promoting the higher Curie temperature. As discussed in Chapter 3, there is great variability reported in the literature of Mn-Ge and Mn-Si magnetic properties.

Conclusion

In conclusion, we successfully synthesized epitaxial self-assembled $Mn_{0.10}Ge_{0.90}$ /Si (001) QD's in our MBE. At this large Mn flux (relative to Ge), we showed, using detailed TEM/EDX analysis, along with SIMS, that Mn resides primarily in copiously nucleated nanorods and nanoclusters that are silicide phases with varying degrees of Ge substitution. Paramagnetism due to the Mn in a dilute phase is observed with a $T_c \sim 25$ K. In addition, Ferromagnetism is observed with $T_c = 220$ K, presumed to be related to the silicide structures rather than a dilute solution phase. Simple analyses of capture and denuded zones provides a complex but fascinating, albeit qualitative, picture with regard to the kinetics of Mn, Ge and Si diffusion to form the rod structures.

Chapter 6: $Ge_{1-x}Mn_x$ QD's and ternary structures grown using evaporation technique

6.1 Introduction

As part of collaborative work with colleagues at UVa, Christopher Nolph and Petra Reinke, we conducted a study at the Center for Fuctional Nanomaterials at Brookhaven National Laborartory. Mn was intentionally incorporated in Ge QD's in different doses by MBE growth in situ in a scanning Auger microscope. These experiments were aimed at establishing the Mn residence in the QD's, and the evolution of surface morphology and structure. Growth conditions nominally similar to those used in the previous chapters (growth rate and temperature) were employed, albeit in a much different growth chamber. In this section the morphology, structure and chemical composition are reported.

6.2 Procedure/Experiment

The growth of $Ge_{1-x}Mn_x$ QD's, on B^{++} Si (001) wafers (~1.2E17/cm^3), was conducted in a UHV chamber fitted to an Omicron Scanning Auger Microscope at Brookhaven National Lab (BNL), with x = 0 to ≈ 20.5 at.% Mn and a base pressure of 1.0 x 10^{-9} T. The growth and *in situ* SEM work at BNL were performed with the assistance of CFN staff scientists Eli Sutter and Peter Sutter. The samples reported here were all grown at T_g = 450 ˚C. Co-deposition of $Ge_{1-x}Mn_x$ was achieved through using an electron beam evaporator and a Knudsen cell (thermal evaporation) as Ge and Mn sources respectively. Due to lack of a quartz crystal rate monitor, the Ge deposition rate had to be estimated from a post-growth volumetric analysis of the AFM data, combined with an assumption that the wetting layer is 3 ML thick. This gives a rate Ge deposition rate of 0.12 Å/s. Three different Ge:Mn flux ratios were examined, based on three different effusion cell temperatures. It is much more difficult to estimate the Mn content from morphological measurements, and ex situ analysis has not been performed. As a result, we first quote the relative compositions based on a factor "Q" that relates to the Mn flux obtained at the three effusion cell temperature; Q is known for the UVa system geometry but not for the BNL geometry. The three compositions studied were 0.2Q, Q, and 4.4Q. An estimate of Q was obtained from using a combination of AFM flooding analysis and second phase stoichiometry. The following assumptions were made in this back of envelope calculation:

- As shall be discussed later in the results, the nanorods and nanoclusers contain 36 and 50 at.% Mn respectively.
- While partitioning the volume of the nanoclusters into respective Mn and Si volumes, we assume that these species have similar densities.
- The nanorods are epitaxial
- Nanoclusters are endotaxial. The section buried into the Si substrate and that above the Si substrate have equal volumes.
- Ge QD structures consist of a 3 MLwetting layer, with huts, domes and superdomes.

From this analysis, we estimate that 4.4Q sample is 16 at.% Mn. Using the known Ge deposition rate of 0.12 Å/s, we calculate 4.4Q to be equal to 0.0126 Å/s. Therefore Q = 0.003 Å/s, and the resulting doping levels in the 0.2Q, Q, and 4.4Q are 1, 4 and 16 at.% Mn. The error bar in these values is estimated to be ± 2%.

The wafer underwent an overnight thermal cleaning at T_s = 600 ˚C followed by a 1250 ˚C flash before growth. The FEI Titan 80-300 kV TEM microscope was employed for high-resolution spatial imaging and compositional analysis using EDX. A single XTEM sample from the 16 at.% Mn sample was prepared by standard wedge polishing techniques followed by Ar ion milling.

6.3 Morphology evolution

Figure 6-1shows the island morphology as a function of Mn content and Ge:Mn QD film thickness. The standard quantum dot morphologies ubiquitous to the Ge/Si (001) system are observed in all cases: huts, domes and superdomes. In addition to the QD's, we observe second phase nucleation and formation in Mn doped samples,

Figure 6-1. At low Mn content and low thickness (1% Mn, 8.5 Å), we observe sparsely distributed, irregular shaped nanoclusters that are likely to be second phases, based on our experiences with samples discussed in the previous chapters. Note that in Figure 6-1 (d), only one of the three particles (the elongated structure shown magnified) is a precipitate. The other two large structures are superdomes. One of these, however, has a protruding precipitate (also shown magnified). The nanocluster and superdomes have a Ge island denuded zone around them. The 4% Mn, 9.6 Å sample looks only slightly different, with 2-3x more second phase nanoclusters per area (but still very sparse), and both the QDs and nanoclusters appear smaller than in the thinner sample. The latter may relate more to difficulties in absolute temperature reproducibility than to the physics of growth. For 14 Å thick samples with 1% Mn, nanoclusters are very large and some asymmetry is apparent, but true nanorods have not formed at this Mn level. However, at 14 Å with 16% Mn, nanorods dominate the landscape, along with numerous more equiaxed precipitate clusters.

For the 1% Mn, 8.5 Å film, the superdomes have trenches around their perimeter as shown by AFM line scans in Figure 6-2 (a). Chaparro et al. reported the formation of trenches around large Ge/Si (001) islands to be a mechanism for stain relaxation prior to dislocation at T > 600 ˚C [129]. For T < 550 ˚C, trenches formed after islands have diameters > 200 nm and were dislocated. Our data suggests that Mn in superdomes Figure 6-2 (a) enhances diffusion kinetic that are responsible for trenches formation.

Trenches may also be important as a means of providing Si to nucleating silicide particles. Figure 6-3 highlights the role of thickness at constant Mn content (1%). There is an increased hut density at higher thickness, which is not expected, and again may suggest the thicker film was grown at lower temperature. Despite this, the size of the nanoclusters clearly increases and their denuded zone area also increases, as the film gets thicker. A nascent precipitate protruding from a Ge superdome is evident in the magnified view. Even at 14 Å, true nanorods are absent at the 1% Mn doping level.

However, at 14 Å thickness and 16% Mn, highly anisotropic nanorods appear, along with copious nanoclusters. Nanorods are typically 1 µm long, 85 nm wide, and 16 nm tall, see Figure 6-4. They exhibit faceted side walls that make ~54 ˚ angles with Si (001) plane and are flat topped. These nanorods are preferentially oriented along the two equivalent Si [110] directions, indicating that they are epitaxial. The appearance of rods only at large Mn supersaturation suggests that nucleation of the rod structure, and its highly anisotropic growth, may be kinetically limited.

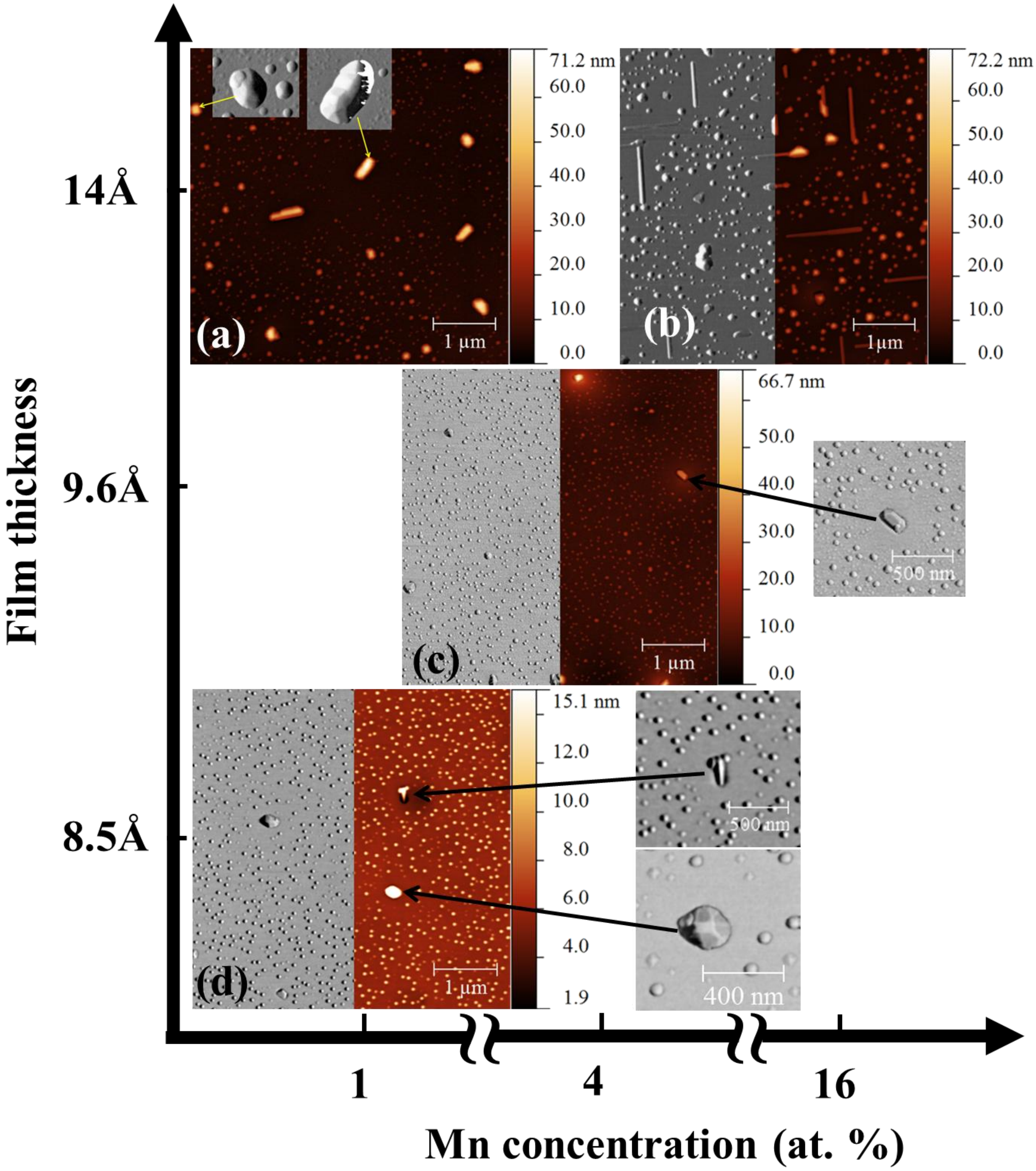

Figure 6-1. 25 µm^2 AFM scans showing the morphological evolution of $Ge_{1-x}Mn_x$ QD's vs. Mn content and film thickness. x = 1 at.% Mn in both (a) and (d), 4 at. % in (c) and 16 at.% Mn in (b). The insets provide a magnified view of different morphological species.

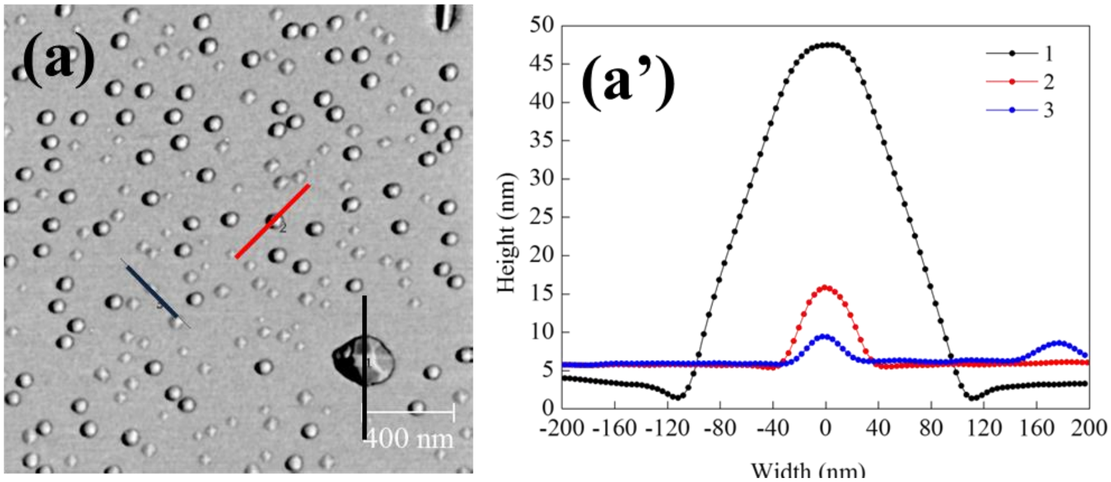

Figure 6-2. (a) AFM scan of 6.3 ML Ge$_{0.99}$Mn$_{0.01}$ film; (b) Corresponding line scans of marked QD's. 1% Mn showing a 45 nm tall superdome with {15 3 23} facets that make 33˚with Si (001). From the lines scans, we observe a trench around the perimeter of the superdome.

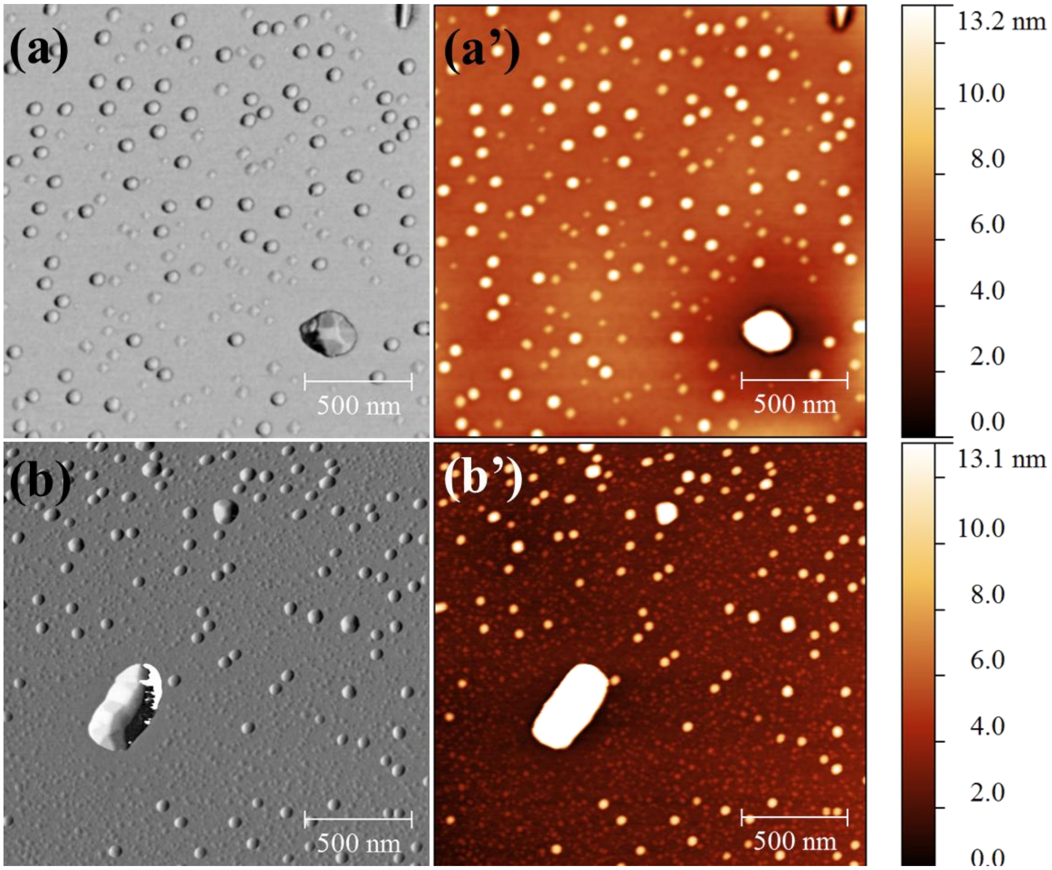

Figure 6-3. Phase and topography AFM scans elucidating the effect of film thickness QD's grown 450 ˚C. (a) 6.3 ML Ge$_{0.99}$Mn$_{0.01}$ film; (b) 10.3 ML Ge$_{0.99}$Mn$_{0.01}$ film.

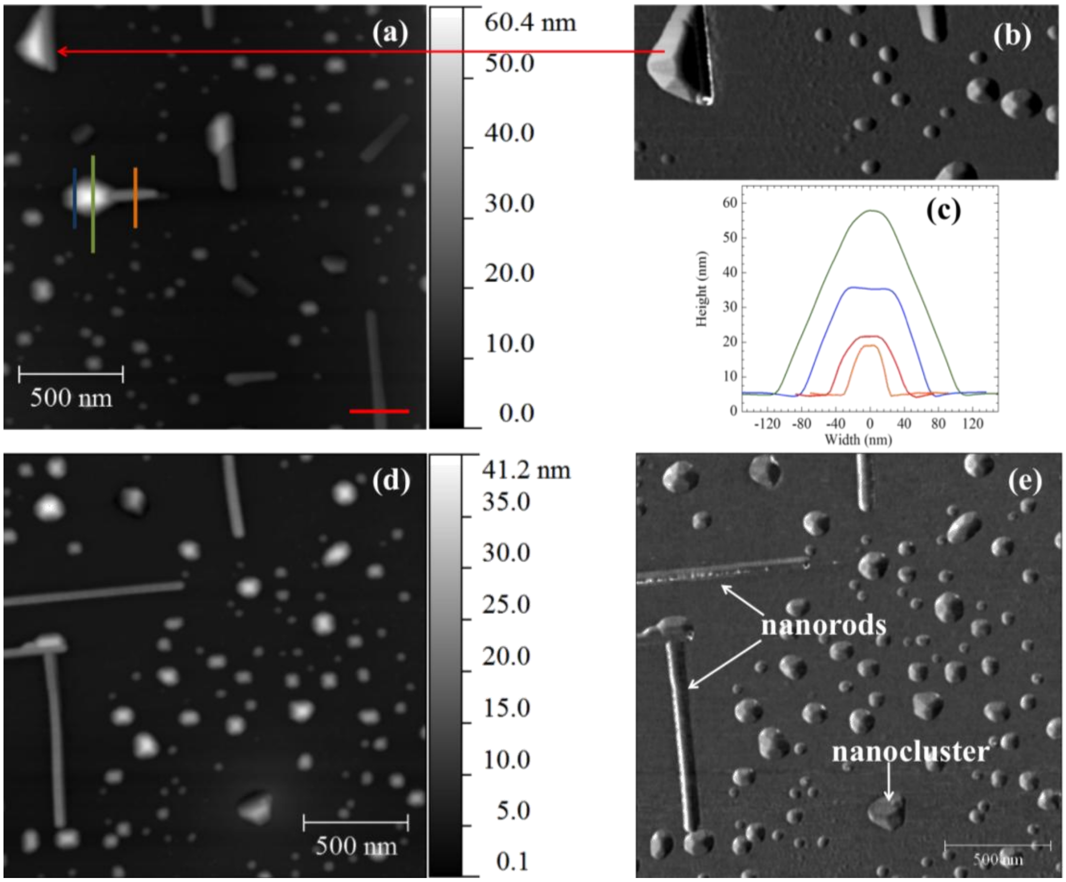

Figure 6-4. 4 μm^2 topography (a) and phase (b) AFM scans of the 16% Mn sample. (c) AFM line scan along the marked structures in (a). Different area scans on the same sample, topography (d) and corresponding phase (e).

Figure 6-5 is an example of an in situ SEM image obtained from the 16% Mn sample after growth, without breaking vacuum. Consistent with the AFM scans, nanorods are preferentially oriented along the two equivalent Si [110] directions. Auger spectroscopy detected Mn only in the nanorods [93].

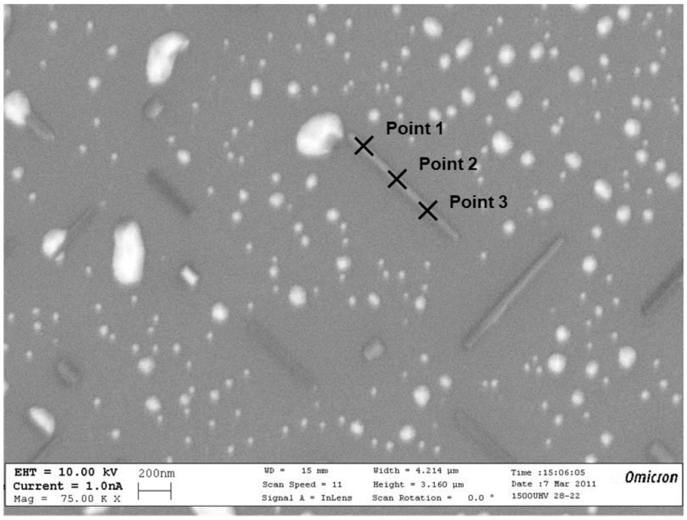

Figure 6-5. SEM image acquired at 10 kV with a probe current of 1.0 nA on the 20.5 at.% Mn sample.

6.4 Structure and Chemical characterization

TEM analysis was performed on the 16% Mn sample. Unfortunately, the results are somewhat limited since the cross-section specimen was too thick in most regions, and the sample was then destroyed in subsequent thinning. Nonetheless, we are able to positively identify the rod crystal structure, and we show evidence for endotaxial clusters as well. Endotaxy is the oriented growth of a crystal inside another crystal, with internal interfaces establishing epitaxy that differ from the substrate plane (in this case, the Si (001)) [130]. Figure 6-6 shows BF TEM micrographs of a nanorod in cross section imaged in the Si <110> zone axis. The dark contrast of the nanorods makes it difficult to image its interface with the Si substrate. Nonetheless, it clear that the nanorods interface terminates right at the Si substrate as seen in Figure 6-6 (c). EDX analysis was performed using a nanoprobe at different points, as shown in Figure 6-6 (d) and (e). Analysis of EDX in Figure 6-6 (d) yields Mn:Si:Ge = 34.9: 64:1.1, for a composition of

$Mn(GeSi)_{1.87}$. FFT analysis elucidates the Si diamond cubic lattice and an addition reciprocal space pattern resulting from the nanorod. The additional pattern was indexed to the $MnSi_{2-x}$ Nowotny chimney ladder (NCL) phase with x = 0.25 viewed along the [001] zone axis. Hence the FFT analysis is in good agreement with the stoichiometry obtained via EDX. Since Mn_4Si_7, $Mn_{15}Si_{26}$, and $Mn_{15}Si_{26}$ all have similar *a* lattice parameters (0.552 nm), we cannot identify which NCL phase this is from FFT analysis. $MnSi_{2-x}$ has a tetragonal crystal structure with space group P-4c2 and lattice parameters a =5.5295 Å and c = nc_{Mn}, where *n* is an integer representing the number of Mn subcells in the unit cell and c_{Mn} is the Mn subcell length in the c-direction = 4.37 Å. The Si (-220) is parallel to the rod (-2-20) [indices relative to the Mn_4Si_7] resulting in a 1.5% misfit strain. The orientation relation of the nanorods is $Mn(Ge_ySi_{1-y})_{2-x}$ (110)/[001] || Si (-1 1 0)/[011] where y = 1.7 at. % Ge. The c-axis of the nanorod is parallel to the Si [011].

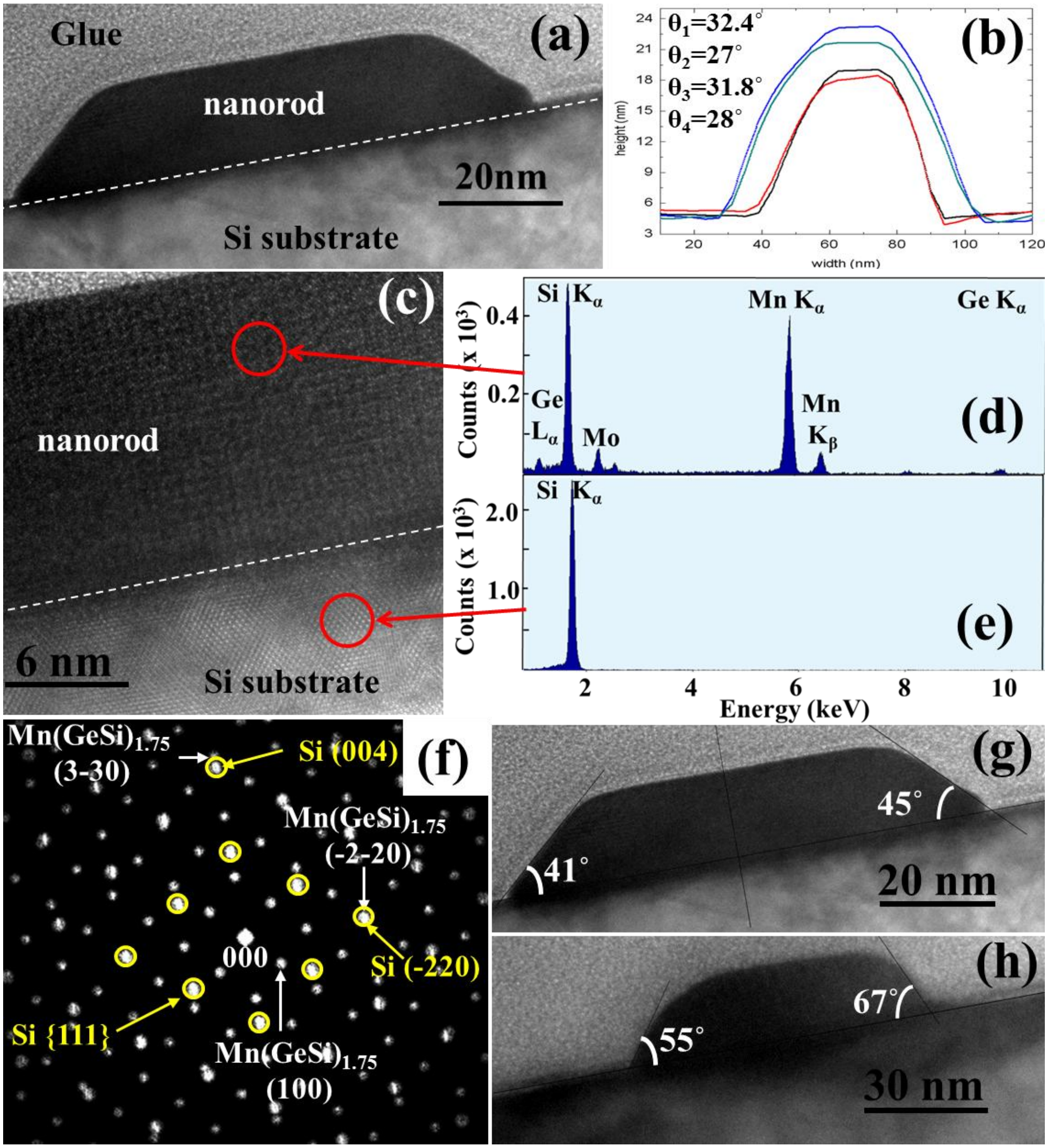

Figure 6-6. TEM micrographs obtained in the Si [1-10] zone axis (a) BF XTEM micrographs of a nanorods; (b) AFM linescans from a typical nanorods for comparison; (c) High resolution BF TEM of (a); (d) and (e) EDX point scan acquired on a rod and in the Si substrate respectively using a nanoprobe; (f) Indexing of the reciprocal space of the nanorods obtained from FFT of (c); (g) and (h) show typical facets angles of the rods.

Figure 6-7 (a) shows a BF TEM micrograph of an *endotaxial* nanocluster. We shall label the structure in Fig. 1-7 as a type A nanocluster. The shape, dimension and facet angles resemble those measured in the “plate like” quasi-triangular shaped nanoclusters, observed in AFM topography scan (inset of Figure 6-7 (a)). The structure was not determined because this region of the specimen was too thick for HRTEM imaging. Chemical analysis performed on the small type A nanocluster in Fig. 1-7(b) suggests a $Mn_{0.44}(Ge_ySi_{1-y})_{0.56}$ stoichiometry, with y = 2.4 at. % Ge. This estimate is close to MnSi clusters which we observed in MBE grown films (Chapter 5).

Figure 6-7 (c) and (d) show a type B cluster. It is endotaxial, over 38 nm tall and spans a width of 110 nm. It is highly faceted both above and below the Si surface. Structural analysis was again not possible due to the excessive specimen thickness. To help identify the type B cluster, AFM dimension analysis of 10 nanorods and 3 type A nanoclusters, along with numerous larger superdome clusters, were carried out. The tallest nanorod and type A nanocluster are found to be 17 nm and 8 nm respectively. Some of the larger free-standing superdomes have heights approaching that seen in Fig. 1-7 (d), but have the wrong shape. Hence, we tentatively eliminate these types of structures as candidates in the identification of type B clusters.

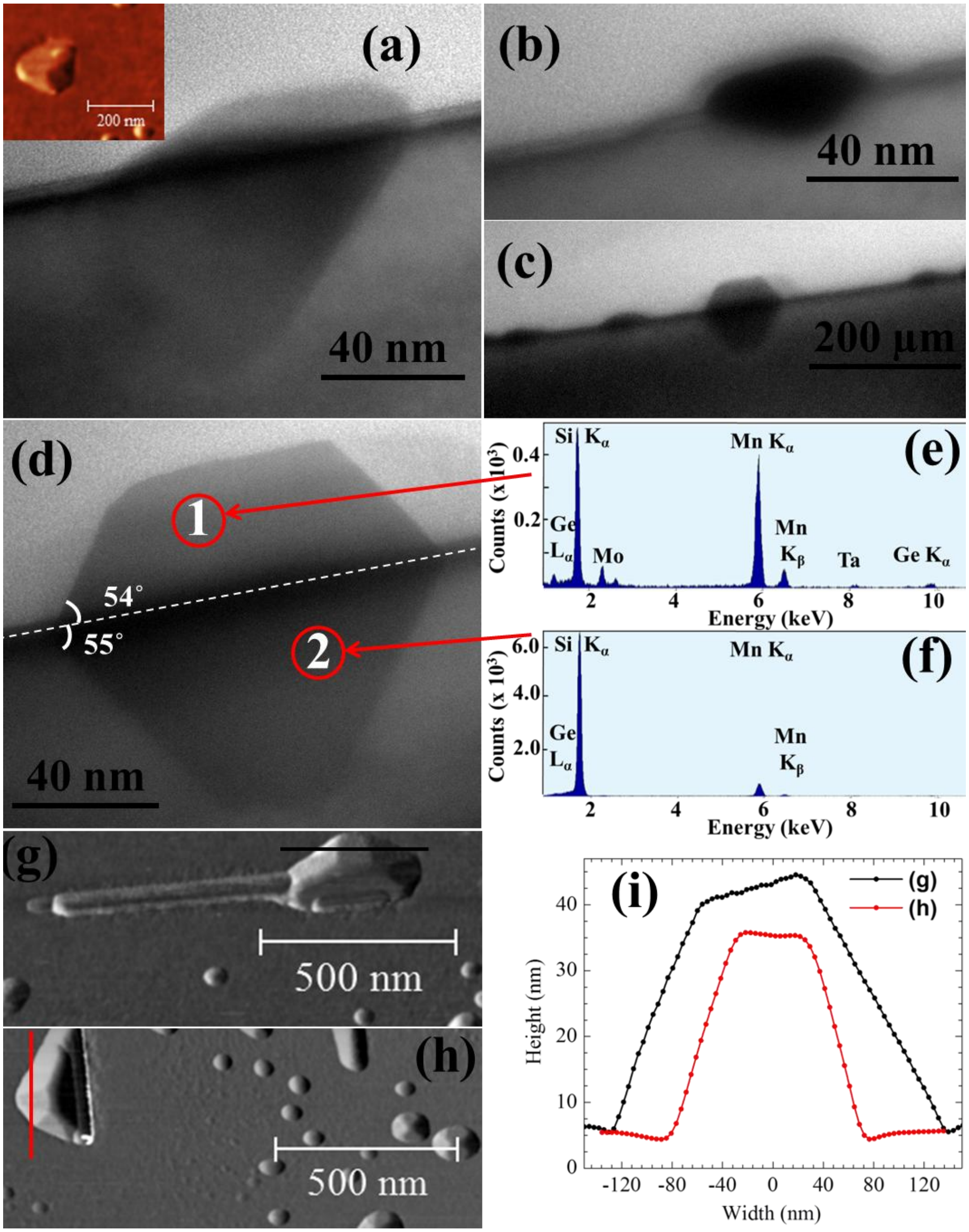

Figure 6-7. BF TEM micrographs of (a) Type A endotaxial nanocluster. Inset: AMF phase image of a typical 2nd phase that matches its shape and dimensions; (b) Endotaxial nanocluster in a thicker region of the specimen; (c) Highly faceted type B endotaxial structure (d) HRXTEM of (c); (e) EDX point scan corresponding to points 1 in (d); (f) EDX point scan corresponding to points 2 in (d); (i) Phase images from AFM scans of structure that match the shape of type B structure, (d); (g) AFM line scans of (g) and (h).

From AFM line scans we can identify only one type of structure that can match the size and shape of the Type B cluster – the "attached-superdome" structures that have a nanorod attached to them, see Figure 6-7 (g) and (h). EDX point scans done on the top section (above the Si substrate) of type B cluster averaged over three points indicate Mn concentration of 35 ± 1 at. % and a $Mn_{0.35}(Ge_ySi_{1-y})_{0.64}$ stoichiometry, where y = 3.4 at.% Ge, close to that expected for the NCL silicide phase. Note that EDX microanalysis of the buried portion of the cluster yields a composition of only 5% Mn in Si, not consistent with any intermetallic phase. Given the strong faceting that mimics the chimney ladder region above it, however, we believe this buried region cannot be a diamond cubic solution phase region but is also the NCL phase. The apparent composition can only be rationalized by assuming that the buried region is also truncated by the TEM specimen edge (similar to the discussion in Chapter 4), so that there EDX path is dominated by Si signal from the substrate. To further confirm this hypothesis, we observe the variation in Mn K_α counts across the cluster from the glue to the Si substrate. We find essentially constant Mn counts after surveying 7 EDX point scans. This implies that the cluster contains the same amount of Mn atom throughout its entirety. We therefore suggest that the large structures terminating the NCL rods, as shown in Figure 6-7 (g) and (h) are themselves the $Mn(GeSi)_{1.75}$ NCL structure, and possess an extended buried region.

There is a lack of appreciable Ge contained in the nanorods and nanoclusters investigated using EDX in the BNL sample, similar to what was observed in the rods discussed in chapter 5. At the same time, there is a zone denuded of Ge domes clusters about the precipitates. As discussed in Chapter 5, it is difficult to reconcile and understand this observation. We propose that when nanoclusters nucleate, the supersaturation of Mn at the nucleation sites enhance the Ge adatom mobility locally. Due to the high mobility, Ge islands nucleation and grow far beyond the clusters. This proposal is in agreement with the observed denuded zones around the cluster and the minimal Ge incorporation in all the three type of clusters discussed. To maintain the respective stoichiometry, the nanoclusters are supplied with the semiconductor atoms from the infinite reservoir of Si in the substrate. The cluster patches that decorate the superdome facets may be an onset of nanorod nucleation. The {15 3 23} facets of the superdomes offer low energy nucleation sites for the clusters.

Two phases, $MnSi_{2-x}$ (nanorods) and a Mn rich phase (concentration points to MnSi) were observed in the 16% BNL sample. The morphologies observed here agree quite well with in situ growth studies by Zou, et al., who deposited 3.7×10^{15} Mn/cm2 directly on Si (001) at 450 ºC, and observed formation of both rods and equiaxed precipitates remarkably similar to those observed here (but without the Ge QDs decorating the rods) [111]. TEM identified the rods as the NCL phase, in the identical orientation we observe, and the equiaxed precipitates as cubic MnSi. Rods were only observed for growth temperatures above 400 ºC, ostensibly due to the large Si flux from the substrate surroundings needed to permit rod growth. The Zou, et al., work indicates that Ge QDs are not necessary to the formation of the second phase precipitates. However, the Zou, et al., experiment did use about 5x more Mn than we deposited in the BNL "16% Mn" sample (and even more than in the 10% Mn MBE sample), suggesting that Ge may still foster easier nucleation of the rod NCL phase.

The differences between the 16% BNL and 10% MBE samples are also interesting. Contrasting with the MBE 10% sample from chapter 5, $MnSi_{2-x}$ (nanorods) were reported. Rods in the BNL sample are clearly the NCL phase, with c-axis in plane. Rods in the MBE sample were tentatively identified as NCL, although diffraction-pattern-matching was not exact. On the contrary, orientation with respect to the Si is much different between the two. The 10% MBE nanorods have a OR $Mn(Ge_ySi_{1-y})_{2-x}$ (01-1)/[331] || Si (01-1)/[001], with growth planes are nominally (331) and (001) for $Mn(Ge_ySi_{1-y})_{2-x}$ Si respectively. The 16% BNL nanorods have a OR $Mn(Ge_ySi_{1-y})_{2-x}$ (110)/[001] || Si (-1 1 0)/[011], with growth planes are (1-10) and (001) for $Mn(Ge_ySi_{1-y})_{2-x}$ and Si respectively. It's worth pointing out that the $Mn(Ge_ySi_{1-y})_{2-x}$ {110} and Si {001} are parallel in both cases. The difference in orientation may suggest that the 10% BNL nanorods are endotaxial as opposed to epitaxial as in the 16% BNL case. These differences may stem from the deposition process differences as well as growth parameter effects. Comparing the morphology of QD in low Mn content BNL versus MBE, we observe variations in hut cluster density and size. The BNL huts are less dense are larger in size, which is characteristic of a higher growth temperature. We therefore propose that difference between the 16% BNL and 10% MBE nanorods may be a result of concentration difference, growth temperature dissimilarity as well as disparity in MBE growth conditions (UHV pressure and deposition techniques).

6.5 Summary

$Mn_xGe_{(1-x)}$ QD samples of varying concentrations have been prepared and characterized in situ in a scanning Auger microscope. In all samples of varying concentrations, we were able to successfully grow Ge QDs. At the highest Mn concentration studied, copious secondary phases were observed. Using a combination of

FFT and chemical analysis, we identify two ternary phases, epitaxial $MnSi_{1.75}$ nanorods and endotaxial MnSi nanoclusters, each containing only small amounts of Ge.

Chapter 7: Conclusion

7.1 Summary

In this work, we set out to:

- Synthesize Mn_xGe_{1-x}/Si (001) self-assembled QDs and investigate the morphological effects (shape, size, density, distribution and strain state) of Mn incorporation on strained Ge surfaces.
- Investigate where Mn preferentially sits as a dopant in the Ge/Si QD's system.
- Investigate the magnetic properties of the Mn doped Ge QD's and explore which Mn configurations or phases are responsible for the observed magnetism

With these critical goals in mind and motivated by recent reports of above-room temperature dilute ferromagnetism in Mn-doped Ge, we successfully synthesized heteroepitaxial self-assembled heteroepitaxial QD's by MBE co-deposition of $Ge_{1-x}Mn_x$, $x = 0$ to 0.16 and at $T_g = 450$ ºC. At these growth conditions required for QD synthesis, the formation of Mn second phases is thermodynamically expected. We employ non-equilibrium growth processes to minimize second phase formation; low Mn concentration, low deposition rates and low growth temperature.

Surprisingly, we find that Mn flux weakly perturbs the Stranski-Krastanov (SK) epitaxial growth mode even at the highest Mn concentration of 16%. All our films show the typical quantum dot morphologies observed for Ge/Si (001) growth, including hut clusters, domes and superdomes. The effect of Mn on surface morphology is relatively benign when 2% Mn flux. Increasing Mn content does drive a clear decrease in D and SD areal density. Concurrently, mean D volume decreases while mean SD volume increases.

The mean lateral size of the huts is largely unperturbed. These observations indicate that Mn flux somehow assists superdome coarsening kinetics at the expense of domes. This could arise from Mn acting as a surfactant, enhancing the surface mobility of Ge, or reducing detachment barriers.

Using a combination of TEM, diffraction, and local chemical analysis, the 2% sample contains two structures that are highly enriched in Mn, buried under superdomes (SD) islands only. These Mn structures are the *Mn solution-phase* and *precipitate cluster,* Figure 7-1. The former is more prevalent and may be a precursor to the formation of the latter. Ge is detected in the buried precipitate, while Si is also found in the QD, indicating significant intermixing. A self-consistent picture begins to emerge with regard to the partitioning of Mn during Ge QD self-assembly on Si (001). The inhomogeneous Ge layer (wetting layer aka WL, domes aka D, and superdomes aka SD) is able to metastably dissolve 1.5% Mn in solution on average (72 ± 6 % of the total deposited Mn atoms). The remaining 0.5% is contained in the Mn solution-phase and precipitate cluster. This suggests the existence of a critical threshold below which all the Mn atoms are incorporated in the Ge matrix in solution form. We propose that the SD act to pump Mn into the substrate and provide a kinetic pathway for Mn entry into Si. This may arise from the highly inhomogeneous strain field, misfit dislocations, or the formation of exposed Si trenches around the dot perimeters. These Mn solution phase patches right below a sub-population of the SD's then transform into precipitate clusters when some critical local concentration is attained. Mn solution-phase and precipitate cluster represents the initial stages of Mn phase separation in this system.

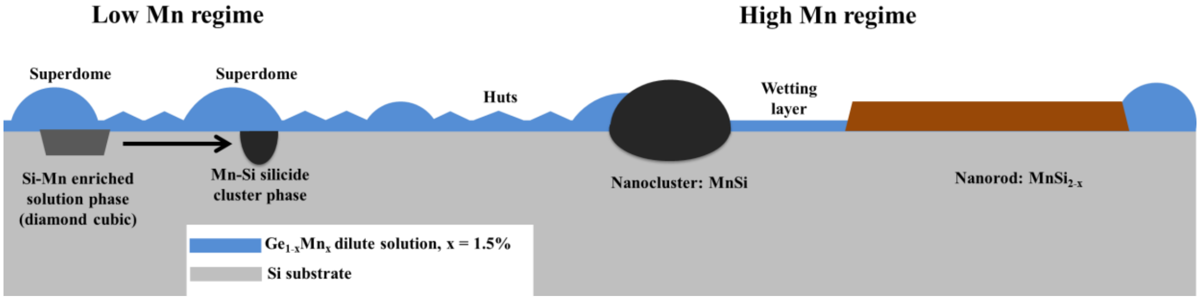

Figure 7-1. Schematic of the evolution of nanostructures during 7 ML $Ge_{1-x}Mn_x$/Si (001) QD film where $0.10 \leq x \geq 0.16$.

At ~ 5%, these precipitate clusters grow upward and out of the host Ge SD to become exposed on the free surface, in the process taking up Ge into the Si sublattice. They appear as small protrusions emerging from Ge SD. Higher Mn contents, $0.10 \leq x \geq 0.16$, results to higher supersaturation that drives copious nucleation of new silicide (nanorods) above the Si substrate. These nanorods heterogeneously nucleate next to SD and epitaxially grow out laterally. They experience a rapid growth compared to the pre-existing precipitate clusters. The protrusions that emerged from their host quantum dots to become relatively large equiaxed silicide precipitates are indexed as MnSi cubic B20 structure. The nanorods are the “Nowotny chimney ladder” (NCL) phases associated with $MnSi_{2-x}$ compounds.

Magnetic measurements indicate a clear evidence of two magnetic phases at 10% Mn, a paramagnetic phase with $T_c = 25$ K (Mn solution phase paramagnetism) and a ferromagnetic phase with a $T_c = 220$ K (second phase nanoclusters). We observe ferromagnetism at T > 300 K in the 10 % sample. We cannot resolve the origin of this FM with the current data due to challenges with the analysis of the magnetic data at such low signals.

7.2 Future work

Firstly, due to the nature of the magnetic signal of our ~ 1 nm films, it is critical to subtract the Si background and parasitic signal from the total moment measured. There is dire need for a robust subtraction method to account for the Si paramagnetic signals and any other parasitic signal present in the sample. In this dissertation, we dedicated a 0% Mn sample to be used as a Mn free reference standard. This method does not account for the variation in parasitic signal from wafer to wafer. It assumes that all the wafers used in all the $Ge_{1-x}Mn_x$ growths, x = 0 – 0.16, have the sample magnetic contamination. We clearly observed that this is not the case. To account for the wafer specific parasitic signal, we need to measure the parasitic signal in each sample individually. We propose a two-step magnetic measurement routine to account to the sample specific parasitic signal subtraction. The first step involves performing magnetic measurements on the sample (260 µm Si substrate with the 1nm $Ge_{1-x}Mn_x$/Si QD's film). Thereafter, a final magnetic measurement is done on just in the Si substrate. The film $Ge_{1-x}Mn_x$/Si QD's can be removed by either mechanical polishing (dimple grinder) or selective chemical etchant. Knowing that we Mn forms silicides 10 – 35 nm deep into the substrate, etching away ~ 1 µm of the substrate and the 1 nm $Ge_{1-x}Mn_x$/Si QD's film will be adequate. We can therefore determine the Si diamagnetic, paramagnetic and parasitic signal that will be subtracted to effectively obtain the residual magnetic signal solely due to Mn. This will provide an avenue for accurate interpretations of the magnetism data and consequently understanding the origin of ferromagnetism in our Mn doped Ge/Si QD's.

From the 10% sample, it is clear that we have magnetic signals from various species in the film. Using the proposed subtraction will help us understand the > 300 K ferromagnetism (Mn related or spurious). Moreover, if we identify all the phases using HRTEM we could consequently establish their magnetic contribution. This is possible by employing numerical calculations using the Brillouin and Langervin function.

Studying the formation of precipitate free Mn doped Ge:Mn QD's is still an avenue of research. There is more to be done in the growth studies, improving magnetic measurement techniques (better subtraction methods suggested above and possibly using alternative element sensitive magnetism measurement methods such as X-ray magnetic circular dichroism (XMCD)) and being able to identify the Mn residence in atomic resolution (EELS mapping or EFTEM). By utilizing different pathways to incorporate Mn may be successful in minimizing segregation. In this work, we have observed the tendency of Mn to react with Si and form Ge poor ternaries. By growing a Ge WL and QD's before depositing Mn would minimize Mn reacting with Si. A viable growth strategy would be depositing 6 ML of Ge domes only ($T_g < 550$ ˚C) followed by ~ 0.5 ML of Mn co-deposited at $T < 60$ ˚C. This growth temperature will eliminate the possibility of Ge and Si intermixing that we speculate may be responsible for quenching the local Mn moment in the QD's. Moreover, the Mn mobility will be reduced hence minimizing second phase formation.

Lastly, improving the $Ge_{1-x}Mn_x$ co-deposition growth process in the MB is a work in progress. Controlling and estimating the Mn deposition rates from the Knudsen cell has been a great challenge in this work. Improvements in the Mn source would be in order. We propose installing a 1" magneton source as a Mn doping source for steady and reliable Mn flux. The immediate challenge in this upgrade is having to grown GeMn film at the operation pressure of the 1” sputter gun (~ 20 mT). We need to ascertain whether we can have good epitaxy at this Ar ambient pressure.

Reference

[1] S. A. Wolf, D. D. Awschalom, R. A. Buhrman, J. M. Daughton, S. von Molnar, M. L. Roukes, A. Y. Chtchelkanova, and D. M. Treger, "Spintronics: A Spin-Based Electronics Vision for the Future," *Science*, vol. 294, no. 5546, pp. 1488–1495, Nov. 2001.

[2] F. Xiu, I. V. Ovchinnikov, P. Upadhyaya, K. Wong, X. Kou, Y. Zhou, and K. L. Wang, "Voltage-controlled ferromagnetic order in MnGe quantum dots," *Nanotechnology*, vol. 21, no. 37, p. 375606, Sep. 2010.

[3] I. Zcaronuticacute, J. Fabian, and S. Das Sarma, "Spintronics: Fundamentals and applications," *Rev. Mod. Phys.*, vol. 76, no. 2, p. 323, Apr. 2004.

[4] T. Dietl, "A ten-year perspective on dilute magnetic semiconductors and oxides," *Nature Materials*, vol. 9, no. 12, pp. 965–974, 2010.

[5] T. Dietl, H. Ohno, and F. Matsukura, "Ferromagnetic Semiconductor Heterostructures for Spintronics," *Electron Devices, IEEE Transactions on*, vol. 54, no. 5, pp. 945–954, 2007.

[6] I. Žutić, J. Fabian, and S. Das Sarma, "Spintronics: Fundamentals and applications," *Rev. Mod. Phys.*, vol. 76, no. 2, pp. 323–410, Apr. 2004.

[7] F. Xiu, "Magnetic Mn-Doped Ge Nanostructures," *ISRN Condensed Matter Physics*, vol. 2012, pp. 1–25, 2012.

[8] I. Appelbaum, B. Huang, and D. J. Monsma, "Electronic measurement and control of spin transport in silicon," *Nature*, vol. 447, no. 7142, pp. 295–298, May 2007.

[9] F. Xiu, Y. Wang, J. Kim, A. Hong, J. Tang, A. P. Jacob, J. Zou, and K. L. Wang, "Electric-field-controlled ferromagnetism in high-Curie-temperature Mn0.05Ge0.95 quantum dots," *Nat Mater*, vol. 9, no. 4, pp. 337–344, Apr. 2010.

[10] F. Xiu, Y. Wang, J. Kim, P. Upadhyaya, Y. Zhou, X. Kou, W. Han, R. K. Kawakami, J. Zou, and K. L. Wang, "Room-Temperature Electric-Field Controlled Ferromagnetism in Mn0.05Ge0.95 Quantum Dots," *ACS Nano*, vol. 4, no. 8, pp. 4948–4954, 2010.

[11] I. T. Yoon, C. J. Park, S. W. Lee, T. W. Kang, D. W. Koh, and D. J. Fu, "Ferromagnetism in self-assembled Ge quantum dots material followed by Mn-implantation and annealing," *Solid-State Electronics*, vol. 52, no. 6, pp. 871–876, Jun. 2008.

[12] J. van Bree, P. M. Koenraad, and J. Fernández-Rossier, "Single-exciton spectroscopy of single Mn doped InAs quantum dots," *Phys. Rev. B*, vol. 78, no. 16, p. 165414, Oct. 2008.

[13] S. Sapra, D. D. Sarma, S. Sanvito, and N. A. Hill, "Influence of Quantum Confinement on the Electronic and Magnetic Properties of (Ga,Mn)As Diluted Magnetic Semiconductor," *Nano Lett.*, vol. 2, no. 6, pp. 605–608, 2002.

[14] P. Lyu and K. Moon, "Ferromagnetism in diluted magnetic semiconductor quantum dot arrays embedded in semiconductors," *arXiv:cond-mat/0210643*, Oct. 2002.

[15] D. M. Hoffman, B. K. Meyer, A. I. Ekimov, I. A. Merkulov, A. L. Efros, M. Rosen, G. Couino, T. Gacoin, and J. P. Boilot, "Giant internal magnetic fields in

Mn doped nanocrystal quantum dots," *Solid State Communications*, vol. 114, no. 10, pp. 547–550, May 2000.

[16] R. Knobel, N. Samarth, S. A. Crooker, and D. D. Awschalom, "Spin-polarized quantum transport and magnetic field-dependent carrier density in magnetic two-dimensional electron gases," *Physica E: Low-dimensional Systems and Nanostructures*, vol. 6, no. 1–4, pp. 786–789, Feb. 2000.

[17] Y. D. Park, A. T. Hanbicki, S. C. Erwin, C. S. Hellberg, J. M. Sullivan, J. E. Mattson, T. F. Ambrose, A. Wilson, G. Spanos, and B. T. Jonker, "A Group-IV Ferromagnetic Semiconductor: MnxGe1-x," *Science*, vol. 295, no. 5555, pp. 651–654, Jan. 2002.

[18] Y. Ohno, D. K. Young, B. Beschoten, F. Matsukura, H. Ohno, and D. D. Awschalom, "Electrical spin injection in a ferromagnetic semiconductor heterostructure," *Nature*, vol. 402, no. 6763, pp. 790–792, Dec. 1999.

[19] H. Ohno, D. Chiba, F. Matsukura, T. Omiya, E. Abe, T. Dietl, Y. Ohno, and K. Ohtani, "Electric-field control of ferromagnetism," *Nature*, vol. 408, no. 6815, pp. 944–946, Dec. 2000.

[20] S. Cho, S. Choi, S. C. Hong, Y. Kim, J. B. Ketterson, B.-J. Kim, Y. C. Kim, and J.-H. Jung, "Ferromagnetism in Mn-doped Ge," *Phys. Rev. B*, vol. 66, no. 3, p. 033303, Jul. 2002.

[21] A. P. Li, J. F. Wendelken, J. Shen, L. C. Feldman, J. R. Thompson, and H. H. Weitering, "Magnetism in Mn_{x}Ge_{1-x} semiconductors mediated by impurity band carriers," *Phys. Rev. B*, vol. 72, no. 19, p. 195205, Nov. 2005.

[22] S. Ahlers, D. Bougeard, H. Riedl, G. Abstreiter, A. Trampert, W. Kipferl, M. Sperl, A. Bergmaier, and G. Dollinger, "Ferromagnetic Ge(Mn) nanostructures," *Physica E: Low-dimensional Systems and Nanostructures*, vol. 32, no. 1–2, pp. 422–425, May 2006.

[23] S. Ahlers, D. Bougeard, N. Sircar, G. Abstreiter, A. Trampert, M. Opel, and R. Gross, "Magnetic and structural properties of Ge_{x}Mn_{1-x} films: Precipitation of intermetallic nanomagnets," *Phys. Rev. B*, vol. 74, no. 21, p. 214411, Dec. 2006.

[24] P. De Padova, J.-P. Ayoub, I. Berbezier, P. Perfetti, C. Quaresima, A. M. Testa, D. Fiorani, B. Olivieri, J.-M. Mariot, A. Taleb-Ibrahimi, M. C. Richter, O. Heckmann, and K. Hricovini, "Mn_{0.06}Ge_{0.94} diluted magnetic semiconductor epitaxially grown on Ge(001): Influence of Mn_{5}Ge_{3} nanoscopic clusters on the electronic and magnetic properties," *Phys. Rev. B*, vol. 77, no. 4, p. 045203, Jan. 2008.

[25] F. Tsui, L. He, L. Ma, A. Tkachuk, Y. S. Chu, K. Nakajima, and T. Chikyow, "Novel Germanium-Based Magnetic Semiconductors," *Phys. Rev. Lett.*, vol. 91, no. 17, p. 177203, Oct. 2003.

[26] M. Jamet, A. Barski, T. Devillers, V. Poydenot, R. Dujardin, P. Bayle-Guillemaud, J. Rothman, E. Bellet-Amalric, A. Marty, J. Cibert, R. Mattana, and S. Tatarenko, "High-Curie-temperature ferromagnetism in self-organized Ge1||[minus]||xMnx nanocolumns," *Nature Materials*, vol. 5, no. 8, pp. 653–659, 2006.

[27] A. P. Li, C. Zeng, K. van Benthem, M. F. Chisholm, J. Shen, S. V. S. Nageswara Rao, S. K. Dixit, L. C. Feldman, A. G. Petukhov, M. Foygel, and H. H. Weitering,

"Dopant segregation and giant magnetoresistance in manganese-doped germanium," *Phys. Rev. B*, vol. 75, no. 20, p. 201201, May 2007.

[28] C. Bihler, C. Jaeger, T. Vallaitis, M. Gjukic, M. S. Brandt, E. Pippel, J. Woltersdorf, and U. Go□sele, "Structural and magnetic properties of Mn[sub 5]Ge[sub 3] clusters in a dilute magnetic germanium matrix," *Appl. Phys. Lett.*, vol. 88, no. 11, p. 112506, 2006.

[29] Y. D. Park, A. Wilson, A. T. Hanbicki, J. E. Mattson, T. Ambrose, G. Spanos, and B. T. Jonker, "Magnetoresistance of Mn:Ge ferromagnetic nanoclusters in a diluted magnetic semiconductor matrix," *Appl. Phys. Lett.*, vol. 78, no. 18, p. 2739, 2001.

[30] L. Ottaviano, A. Continenza, G. Profeta, G. Impellizzeri, A. Irrera, R. Gunnella, and O. Kazakova, "Room-temperature ferromagnetism in Mn-implanted amorphous Ge," *Phys. Rev. B*, vol. 83, no. 13, p. 134426, Apr. 2011.

[31] A. Verna, L. Ottaviano, M. Passacantando, S. Santucci, P. Picozzi, F. D'Orazio, F. Lucari, M. De Biase, R. Gunnella, M. Berti, A. Gasparotto, G. Impellizzeri, and F. Priolo, "Ferromagnetism in ion implanted amorphous and nanocrystalline Mn_{x}Ge_{1−x}," *Phys. Rev. B*, vol. 74, no. 8, p. 085204, 2006.

[32] E. S. Park, D. H. Kim, and W. T. Kim, "Parameter for glass forming ability of ternary alloy systems," *Applied Physics Letters*, vol. 86, no. 6, pp. 061907–061907–3, Feb. 2005.

[33] H.-T. Lin, W.-J. Huang, S.-H. Wang, H.-H. Lin, and T.-S. Chin, "Carrier-mediated ferromagnetism in p-Si(100) by sequential ion-implantation of B and Mn," *Journal of Physics: Condensed Matter*, vol. 20, no. 9, p. 095004, Mar. 2008.

[34] F. D'Orazio, F. Lucari, M. Passacantando, P. Picozzi, S. Santucci, and A. Verna, "Magnetooptical study of Mn ions implanted in Ge," *IEEE Transactions on Magnetics*, vol. 38, no. 5, pp. 2856 – 2858, Sep. 2002.

[35] L. Liu, N. Chen, Z. Yin, F. Yang, J. Zhou, and F. Zhang, "Investigation of Mn-implanted n-type Ge," *Journal of Crystal Growth*, vol. 265, no. 3–4, pp. 466–470, May 2004.

[36] L. Lf, C. Nf, C. Cl, L. Yl, Y. Zg, and Y. F, "Magnetic properties of Mn-implanted n-type Ge," *SEMI OpenIR*, vol. 273, no. 1–2, 2004.

[37] E. Biegger, L. Stäheli, M. Fonin, U. Rüdiger, and Y. S. Dedkov, "Intrinsic ferromagnetism versus phase segregation in Mn-doped Ge," *Journal of Applied Physics*, vol. 101, no. 10, pp. 103912–103912–5, May 2007.

[38] N. Pinto, L. Morresi, M. Ficcadenti, R. Murri, F. D'Orazio, F. Lucari, L. Boarino, and G. Amato, "Magnetic and electronic transport percolation in epitaxial Ge_{1−x}Mn_{x} films," *Phys. Rev. B*, vol. 72, no. 16, p. 165203, Oct. 2005.

[39] J.-P. Ayoub, L. Favre, I. Berbezier, A. Ronda, L. Morresi, and N. Pinto, "Morphological and structural evolutions of diluted Ge[sub 1−x]Mn[sub x] epitaxial films," *Appl. Phys. Lett.*, vol. 91, no. 14, p. 141920, 2007.

[40] S. Picozzi, L. Ottaviano, M. Passacantando, G. Profeta, A. Continenza, F. Priolo, M. Kim, and A. J. Freeman, "X-ray absorption spectroscopy in MnxGe1−x diluted magnetic semiconductor: Experiment and theory," *Applied Physics Letters*, vol. 86, no. 6, pp. 062501–062501–3, Jan. 2005.

[41] J.-S. Kang, G. Kim, S. C. Wi, S. S. Lee, S. Choi, S. Cho, S. W. Han, K. H. Kim, H. J. Song, H. J. Shin, A. Sekiyama, S. Kasai, S. Suga, and B. I. Min, "Spatial

Chemical Inhomogeneity and Local Electronic Structure of Mn-Doped Ge Ferromagnetic Semiconductors," *Phys. Rev. Lett.*, vol. 94, no. 14, p. 147202, Apr. 2005.

[42] A. P. Li, J. Shen, J. R. Thompson, and H. H. Weitering, "Ferromagnetic percolation in Mn[sub x]Ge[sub 1−x] dilute magnetic semiconductor," *Appl. Phys. Lett.*, vol. 86, no. 15, p. 152507, 2005.

[43] D. Bougeard, S. Ahlers, A. Trampert, N. Sircar, and G. Abstreiter, "Clustering in a Precipitate-Free GeMn Magnetic Semiconductor," *Phys. Rev. Lett.*, vol. 97, no. 23, p. 237202, Dec. 2006.

[44] J. Deng, Y. Tian, S. Yan, Q. Cao, G. Liu, Y. Chen, L. Mei, G. Ji, and Z. Zhang, "Magnetism of amorphous Ge1−xMnx magnetic semiconductor films," *Journal of Applied Physics*, vol. 104, no. 1, pp. 013905–013905–4, Jul. 2008.

[45] T. Devillers, M. Jamet, A. Barski, V. Poydenot, P. Bayle-Guillemaud, E. Bellet-Amalric, S. Cherifi, and J. Cibert, "Structure and magnetism of self-organized Ge_{1−x}Mn_{x} nanocolumns on Ge(001)," *Phys. Rev. B*, vol. 76, no. 20, p. 205306, Nov. 2007.

[46] A. Jain, M. Jamet, A. Barski, T. Devillers, I.-S. Yu, C. Porret, P. Bayle-Guillemaud, V. Favre-Nicolin, S. Gambarelli, V. Maurel, G. Desfonds, J. F. Jacquot, and S. Tardif, "Structure and magnetism of Ge3Mn5 clusters," *Journal of Applied Physics*, vol. 109, no. 1, pp. 013911–013911–4, Jan. 2011.

[47] L. Ottaviano, A. Continenza, G. Profeta, G. Impellizzeri, A. Irrera, R. Gunnella, and O. Kazakova, "Room-temperature ferromagnetism in Mn-implanted amorphous Ge," *Phys. Rev. B*, vol. 83, no. 13, p. 134426, Apr. 2011.

[48] S. Tardif, V. Favre-Nicolin, F. Lançon, E. Arras, M. Jamet, A. Barski, C. Porret, P. Bayle-Guillemaud, P. Pochet, T. Devillers, and M. Rovezzi, "Strain and correlation of self-organized Ge_{1−x}Mn_{x} nanocolumns embedded in Ge (001)," *Phys. Rev. B*, vol. 82, no. 10, p. 104101, 2010.

[49] L. Zeng, J. X. Cao, E. Helgren, J. Karel, E. Arenholz, L. Ouyang, D. J. Smith, R. Q. Wu, and F. Hellman, "Distinct local electronic structure and magnetism for Mn in amorphous Si and Ge," *Phys. Rev. B*, vol. 82, no. 16, p. 165202, Oct. 2010.

[50] M. Bolduc, C. Awo-Affouda, A. Stollenwerk, M. B. Huang, F. G. Ramos, G. Agnello, and V. P. LaBella, "Above room temperature ferromagnetism in Mn-ion implanted Si," *Phys. Rev. B*, vol. 71, no. 3, p. 033302, Jan. 2005.

[51] C. Zeng, Z. Zhang, K. van Benthem, M. F. Chisholm, and H. H. Weitering, "Optimal Doping Control of Magnetic Semiconductors via Subsurfactant Epitaxy," *Phys. Rev. Lett.*, vol. 100, no. 6, p. 066101, Feb. 2008.

[52] W. Zhu, H. H. Weitering, E. G. Wang, E. Kaxiras, and Z. Zhang, "Contrasting Growth Modes of Mn on Ge(100) and Ge(111) Surfaces: Subsurface Segregation versus Intermixing," *Phys. Rev. Lett.*, vol. 93, no. 12, p. 126102, 2004.

[53] A. B. Gokhale and R. Abbaschian, "The Ge-Mn (Germanium-Manganese) system," *Bulletin of Alloy Phase Diagrams*, vol. 11, no. 5, pp. 460–468, Oct. 1990.

[54] M. Jamet, A. Barski, T. Devillers, V. Poydenot, R. Dujardin, P. Bayle-Guillemaud, J. Rothman, E. Bellet-Amalric, A. Marty, J. Cibert, R. Mattana, and S. Tatarenko, "High-Curie-temperature ferromagnetism in self-organized Ge1-xMnx nanocolumns," *Nat Mater*, vol. 5, no. 8, pp. 653–659, 2006.

[55] C. Zeng, S. C. Erwin, L. C. Feldman, A. P. Li, R. Jin, Y. Song, J. R. Thompson, and H. H. Weitering, "Epitaxial ferromagnetic Mn[sub 5]Ge[sub 3] on Ge(111)," *Appl. Phys. Lett.*, vol. 83, no. 24, p. 5002, 2003.

[56] L. Morresi, J. P. Ayoub, N. Pinto, M. Ficcadenti, R. Murri, A. Ronda, and I. Berbezier, "Formation of Mn5Ge3 nanoclusters in highly diluted MnxGe1−x alloys," *Materials Science in Semiconductor Processing*, vol. 9, no. 4–5, pp. 836–840, Aug. 2006.

[57] "annurev.anthro.33.070203.143706 (application/pdf Object)." [Online]. Available: http://arjournals.annualreviews.org/doi/pdf/10.1146/annurev.anthro.33.070203.143706. [Accessed: 05-Mar-2009].

[58] J.-P. Ayoub, L. Favre, I. Berbezier, A. Ronda, L. Morresi, and N. Pinto, "Morphological and structural evolutions of diluted Ge1−xMnx epitaxial films," *Applied Physics Letters*, vol. 91, no. 14, pp. 141920–141920–3, Oct. 2007.

[59] "AIP Journal PDF." .

[60] H. Kim, G.-E. Jung, J.-H. Lim, K. H. Chung, S.-J. Kahng, W. Son, and S. Han, "Epitaxial Mn $_5$ Ge $_3$ nano-islands on a Ge(001) surface," *Nanotechnology*, vol. 19, no. 2, p. 025707, Jan. 2008.

[61] R. T. Lechner, V. Holý, S. Ahlers, D. Bougeard, J. Stangl, A. Trampert, A. Navarro-Quezada, and G. Bauer, "Self-assembled Mn5Ge3 nanomagnets close to the surface and deep inside a Ge1−xMnx epilayer," *Applied Physics Letters*, vol. 95, no. 2, pp. 023102–023102–3, Jul. 2009.

[62] A. Jain, M. Jamet, A. Barski, T. Devillers, C. Porret, P. Bayle-Guillemaud, S. Gambarelli, V. Maurel, and G. Desfonds, "Investigation of magnetic anisotropy of (Ge,Mn) nanocolumns," *Applied Physics Letters*, vol. 97, no. 20, pp. 202502–202502–3, Nov. 2010.

[63] K. Sato, H. Katayama-Yoshida, and P. H. Dederichs, "High Curie Temperature and Nano-Scale Spinodal Decomposition Phase in Dilute Magnetic Semiconductors," *Japanese Journal of Applied Physics*, vol. 44, no. 30, pp. L948–L951, 2005.

[64] M. Holub, S. Chakrabarti, S. Fathpour, P. Bhattacharya, Y. Lei, and S. Ghosh, "Mn-doped InAs self-organized diluted magnetic quantum-dot layers with Curie temperatures above 300 K," *Applied Physics Letters*, vol. 85, no. 6, pp. 973–975, Aug. 2004.

[65] Z. Yu-Hong, Z. Jian-Hua, B. Jing-Feng, W. Wei-Zhu, J. Yang, W. Xiao-Guang, and X. Jian-Bai, "Cr-Doped InAs Self-Organized Diluted Magnetic Quantum Dots with Room-Temperature Ferromagnetism," *Chinese Physics Letters*, vol. 24, no. 7, pp. 2118–2121, Jul. 2007.

[66] F. Matsukura, H. Ohno, A. Shen, and Y. Sugawara, "Transport properties and origin of ferromagnetism in (Ga,Mn)As," *Phys. Rev. B*, vol. 57, no. 4, p. R2037, Jan. 1998.

[67] Y.-J. Zhao, T. Shishidou, and A. J. Freeman, "Ruderman-Kittel-Kasuya-Yosida-like ferromagnetism in MnxGe1-x," *Phys. Rev. Lett.*, vol. 90, no. 4, p. 047204, Jan. 2003.

[68] T. Dietl, H. Ohno, F. Matsukura, J. Cibert, and D. Ferrand, "Zener Model Description of Ferromagnetism in Zinc-Blende Magnetic Semiconductors," *Science*, vol. 287, no. 5455, pp. 1019–1022, Feb. 2000.

[69] H. C. Jeon, K. J. Chung, K. J. Chung, T. W. Kang, and T. W. Kim, “Enhancement of the Ferromagnetic Transition Temperature in Self-Assembled (Ga1-xMnx)As Quantum Wires,” *Japanese Journal of Applied Physics*, vol. 43, p. 963, Jul. 2004.

[70] S. U. Yuldashev, Y. Shon, Y. H. Kwon, D. J. Fu, D. Y. Kim, H. J. Kim, T. W. Kang, and X. Fan, “Enhanced positive magnetoresistance effect in GaAs with nanoscale magnetic clusters,” *Journal of Applied Physics*, vol. 90, no. 6, pp. 3004–3006, Sep. 2001.

[71] A. Stroppa, S. Picozzi, A. Continenza, and A. J. Freeman, “Electronic structure and ferromagnetism of Mn-doped group-IV semiconductors,” *Phys. Rev. B*, vol. 68, no. 15, p. 155203, Oct. 2003.

[72] A. Kaminski and S. Das Sarma, “Magnetic and transport percolation in diluted magnetic semiconductors,” *Phys. Rev. B*, vol. 68, no. 23, p. 235210, Dec. 2003.

[73] A. Kaminski and S. Das Sarma, “Polaron Percolation in Diluted Magnetic Semiconductors,” *Phys. Rev. Lett.*, vol. 88, no. 24, p. 247202, May 2002.

[74] M. Shaughnessy, C. Y. Fong, R. Snow, L. H. Yang, X. S. Chen, and Z. M. Jiang, “Structural and magnetic properties of single dopants of Mn and Fe for Si-based spintronic materials,” *Phys. Rev. B*, vol. 82, no. 3, p. 035202, Jul. 2010.

[75] M. Bolduc, C. Awo-Affouda, A. Stollenwerk, M. B. Huang, F. G. Ramos, G. Agnello, and V. P. LaBella, “Above room temperature ferromagnetism in Mn-ion implanted Si,” *Phys. Rev. B*, vol. 71, no. 3, p. 033302, Jan. 2005.

[76] M. Shaughnessy, C. Y. Fong, R. Snow, K. Liu, J. E. Pask, and L. H. Yang, “Origin of large moments in MnxSi1−x at small x,” *Applied Physics Letters*, vol. 95, no. 2, pp. 022515–022515–3, Jul. 2009.

[77] K. Hricovini, P. De Padova, C. Quaresima, P. Perfetti, R. Brochier, C. Richter, V. Ilakovac, O. Heckmann, L. Lechevallier, P. Bencok, P. Le Fevre, and C. Teodorescu, “Atomic structure and magnetic properties of Mn on InAs(1 0 0),” *Applied Surface Science*, vol. 212–213, pp. 17–25, May 2003.

[78] C. Jaeger, C. Bihler, T. Vallaitis, S. T. B. Goennenwein, M. Opel, R. Gross, and M. S. Brandt, “Spin-glass-like behavior of Ge:Mn,” *Phys. Rev. B*, vol. 74, no. 4, p. 045330, Jul. 2006.

[79] J. Tersoff and F. K. LeGoues, “Competing relaxation mechanisms in strained layers,” *Phys. Rev. Lett.*, vol. 72, no. 22, p. 3570, May 1994.

[80] G. Medeiros-Ribeiro, A. M. Bratkovski, T. I. Kamins, D. A. �A. Ohlberg, and R. S. Williams, “Shape Transition of Germanium Nanocrystals on a Silicon (001) Surface from Pyramids to Domes,” *Science*, vol. 279, no. 5349, pp. 353–355, Jan. 1998.

[81] Y.-W. Mo, D. E. Savage, B. S. Swartzentruber, and M. G. Lagally, “Kinetic pathway in Stranski-Krastanov growth of Ge on Si(001),” *Phys. Rev. Lett.*, vol. 65, no. 8, p. 1020, 1990.

[82] H. Sunamura, N. Usami, Y. Shiraki, and S. Fukatsu, “Island formation during growth of Ge on Si(100): A study using photoluminescence spectroscopy,” *Appl. Phys. Lett.*, vol. 66, no. 22, p. 3024, 1995.

[83] M. Tomitori, K. Watanabe, M. Kobayashi, and O. Nishikawa, “STM study of the Ge growth mode on Si(001) substrates,” *Applied Surface Science*, vol. 76–77, pp. 322–328, Mar. 1994.

[84] M. Kästner and B. Voigtländer, “Kinetically Self-Limiting Growth of Ge Islands on Si(001),” *Phys. Rev. Lett.*, vol. 82, no. 13, pp. 2745–2748, Mar. 1999.

[85] G.-H. Lu and F. Liu, “Towards quantitative understanding of formation and stability of Ge hut islands on Si(001),” *Phys. Rev. Lett*, vol. 94, no. 17, p. 176103, May 2005.

[86] M. R. McKay, J. A. Venables, and J. Drucker, “Kinetic frustration of Ostwald ripening in Ge/Si(100) hut ensembles,” *Solid State Communications*, vol. 149, no. 35–36, pp. 1403–1409, Sep. 2009.

[87] J. A. Floro, G. A. Lucadamo, E. Chason, L. B. Freund, M. Sinclair, R. D. Twesten, and R. Q. Hwang, “SiGe Island Shape Transitions Induced by Elastic Repulsion,” *Phys. Rev. Lett.*, vol. 80, no. 21, p. 4717, May 1998.

[88] F. M. Ross, R. M. Tromp, and M. C. Reuter, “Transition States Between Pyramids and Domes During Ge/Si Island Growth,” *Science*, vol. 286, no. 5446, pp. 1931–1934, Dec. 1999.

[89] J. L. Gray, R. Hull, and J. A. Floro, “Periodic arrays of epitaxial self-assembled SiGe quantum dot molecules grown on patterned Si substrates,” *J. Appl. Phys.*, vol. 100, no. 8, p. 084312, 2006.

[90] Y. Tu and J. Tersoff, “Origin of Apparent Critical Thickness for Island Formation in Heteroepitaxy,” *Phys. Rev. Lett.*, vol. 93, no. 21, p. 216101, Nov. 2004.

[91] D. E. Jesson, K. M. Chen, S. J. Pennycook, T. Thundat, and R. J. Warmack, “Morphological Evolution of Strained Films by Cooperative Nucleation,” *Phys. Rev. Lett.*, vol. 77, no. 7, p. 1330, 1996.

[92] J. . Liu, Q. Gong, D. . Huang, J. . Li, D. . Sun, and M. . Kong, “Evolution of height distribution of Ge islands on Si(1 0 0),” *Journal of Crystal Growth*, vol. 200, no. 3–4, pp. 617–620, Apr. 1999.

[93] A. A. Shklyaev, M. Shibata, and M. Ichikawa, “Ge islands on Si(111) at coverages near the transition from two-dimensional to three-dimensional growth,” *Surface Science*, vol. 416, no. 1–2, pp. 192–199, Oct. 1998.

[94] F. M. Ross, J. Tersoff, and R. M. Tromp, “Coarsening of Self-Assembled Ge Quantum Dots on Si(001),” *Phys. Rev. Lett.*, vol. 80, no. 5, p. 984, Feb. 1998.

[95] J. L. Gray, R. Hull, C.-H. Lam, P. Sutter, J. Means, and J. A. Floro, “Beyond the heteroepitaxial quantum dot: Self-assembling complex nanostructures controlled by strain and growth kinetics,” *Phys. Rev. B*, vol. 72, no. 15, p. 155323, Oct. 2005.

[96] J.-H. Cho and M.-H. Kang, “Ge-Si intermixing at the Ge/Si(001) surface,” *Phys. Rev. B*, vol. 61, no. 3, p. 1688, Jan. 2000.

[97] O. Guise, J. T. Yates, J. Levy, J. Ahner, V. Vaithyanathan, and D. G. Schlom, “Patterning of sub-10-nm Ge islands on Si(100) by directed self-assembly,” *Appl. Phys. Lett.*, vol. 87, no. 17, p. 171902, 2005.

[98] H.-U. Danzebrink, L. Koenders, G. Wilkening, A. Yacoot, and H. Kunzmann, “Advances in Scanning Force Microscopy for Dimensional Metrology,” *CIRP Annals - Manufacturing Technology*, vol. 55, no. 2, pp. 841–878, 2006.

[99] J. Reyes-Gasga and R. García-García, “Analysis of the electron-beam radiation damage of TEM samples in the acceleration energy range from 0.1 to 2 MeV using the standard theory for fast electrons,” *Radiation Physics and Chemistry*, vol. 64, no. 5–6, pp. 359–367, Aug. 2002.

[100] B. D. Cullity and C. D. Graham, *Introduction to Magnetic Materials*. John Wiley & Sons, 2009.

[101] A. Cho and J. Arthur, “Molecular Beam Epitaxy,” *Prog. Solid-State Chem.*, vol. 10, pp. 157–192, 1975.

[102] Y. Kudriavtsev, A. Villegas, A. Godines, and R. Asomoza, “Calculation of the surface binding energy for ion sputtered particles,” *Applied Surface Science*, vol. 239, no. 3–4, pp. 273–278, Jan. 2005.

[103] M. Thompson, *Philosophical Magazine*, vol. 18, p. 377, 1968.

[104] Chris Petz, “Epitaxial nanotemplates for strain modulated carrier confinement in Silicon,” University of Virginia, 2012.

[105] Copeland Kell, “Synthesis of Amorphous Ge:Mn Thin Films and Position-Controlled Ge:Si Self-Assembled Nanostructures,” University of Virginia, 2009.

[106] M. Meuris, S. Arnauts, I. Cornelissen, K. Kenis, M. Lux, S. Degendt, P. Mertens, I. Teerlinck, R. Vos, L. Loewenstein, M. M. Heyns, and K. Wolke, “Implementation of the IMEC-Clean in advanced CMOS manufacturing,” in *Semiconductor Manufacturing Conference Proceedings, 1999 IEEE International Symposium on*, 1999, pp. 157–160.

[107] A. Ishizaka, “Low Temperature Surface Cleaning of Silicon and Its Application to Silicon MBE,” *J. Electrochem. Soc.*, vol. 133, no. 4, p. 666, 1986.

[108] Chris Nolph, “Incorporation of Mn into Ge Quantum Dots: Growth. Strategies to Control Structure and Magnetism,” University of Virginia, 2012.

[109] “Footnote 1: In reality, the net moment will be much less than this depending on the detailed coupling associated with the varying local environments that Mn atoms will find themselves in.,” .

[110] V. Holý, R. T. Lechner, S. Ahlers, L. Horák, T. H. Metzger, A. Navarro-Quezada, A. Trampert, D. Bougeard, and G. Bauer, “Diffuse x-ray scattering from inclusions in ferromagnetic Ge_{1−x}Mn_{x} layers,” *Phys. Rev. B*, vol. 78, no. 14, p. 144401, Oct. 2008.

[111] Z.-Q. Zou, W.-C. Li, J.-M. Liang, and D. Wang, “Self-organized growth of higher manganese silicide nanowires on Si(1 1 1), (1 1 0) and (0 0 1) surfaces,” *Acta Materialia*, vol. 59, no. 20, pp. 7473–7479, Dec. 2011.

[112] J. Deng, Y. Tian, S. Yan, Q. Cao, G. Liu, Y. Chen, L. Mei, G. Ji, and Z. Zhang, “Magnetism of amorphous Ge1−xMnx magnetic semiconductor films,” *Journal of Applied Physics*, vol. 104, no. 1, pp. 013905–013905–4, Jul. 2008.

[113] L. Zeng, J. X. Cao, E. Helgren, J. Karel, E. Arenholz, L. Ouyang, D. J. Smith, R. Q. Wu, and F. Hellman, “Distinct local electronic structure and magnetism for Mn in amorphous Si and Ge,” *Phys. Rev. B*, vol. 82, no. 16, p. 165202, Oct. 2010.

[114] D. Bougeard, N. Sircar, S. Ahlers, V. Lang, G. Abstreiter, A. Trampert, J. M. LeBeau, S. Stemmer, D. W. Saxey, and A. Cerezo, “Ge1-x Mnx Clusters: Central Structural and Magnetic Building Blocks of Nanoscale Wire-Like Self-Assembly in a Magnetic Semiconductor,” *Nano Letters*, vol. 9, no. 11, pp. 3743–3748, Nov. 2009.

[115] S. Sugahara, K. L. Lee, S. Yada, and M. Tanaka, “Precipitation of Amorphous Ferromagnetic Semiconductor Phase in Epitaxially Grown Mn-Doped Ge Thin Films,” *Jpn. J. Appl. Phys.*, vol. 44, no. No. 48, pp. L1426–L1429, Nov. 2005.

[116] E. R. Weber, “Transition metals in silicon,” *Applied Physics A: Materials Science & Processing*, vol. 30, no. 1, pp. 1–22, 1983.

[117] S. A. Chaparro, Y. Zhang, and J. Drucker, “Strain relief via trench formation in Ge/Si(100) islands,” *Applied Physics Letters*, vol. 76, no. 24, pp. 3534–3536, Jun. 2000.

[118] S. A. Chaparro, Y. Zhang, J. Drucker, D. Chandrasekhar, and D. J. Smith, “Evolution of Ge/Si(100) islands: Island size and temperature dependence,” *Journal of Applied Physics*, vol. 87, no. 5, pp. 2245–2254, Mar. 2000.

[119] H. Q. Ye and S. Amelinckx, “High-resolution electron microscopic study of manganese silicides MnSi2−x,” *Journal of Solid State Chemistry*, vol. 61, no. 1, pp. 8–39, Jan. 1986.

[120] G. Kappel, G. Fischer, and A. Jaéglé, “Magnetic investigation of the system Mn5Ge3□Mn5Si3,” *physica status solidi (a)*, vol. 34, no. 2, pp. 691–696, 1976.

[121] H. Q. Ye and S. Amelinckx, “High-resolution electron microscopic study of manganese silicides MnSi2−x,” *Journal of Solid State Chemistry*, vol. 61, no. 1, pp. 8–39, Jan. 1986.

[122] S. Zhou, K. Potzger, G. Zhang, A. Mücklich, F. Eichhorn, N. Schell, R. Grötzschel, B. Schmidt, W. Skorupa, M. Helm, J. Fassbender, and D. Geiger, “Structural and magnetic properties of Mn-implanted Si,” *Phys. Rev. B*, vol. 75, no. 8, p. 085203, Feb. 2007.

[123] U. Gottlieb, A. Sulpice, B. Lambert-Andron, and O. Laborde, “Magnetic properties of single crystalline Mn4Si7,” *Journal of Alloys and Compounds*, vol. 361, no. 1–2, pp. 13–18, Oct. 2003.

[124] S. Yabuuchi, Y. Ono, M. Nagase, H. Kageshima, A. Fujiwara, and E. Ohta, “Ferromagnetism of Manganese–Silicide Nanopariticles in Silicon,” *Jpn. J. Appl. Phys.*, vol. 47, pp. 4487–4490, 2008.

[125] V. N. Men’shov, V. V. Tugushev, S. Caprara, and E. V. Chulkov, “High-temperature ferromagnetism in Si:Mn alloys,” *Phys. Rev. B*, vol. 83, no. 3, p. 035201, Jan. 2011.

[126] C. Thessieu, J. Flouquet, G. Lapertot, A. . Stepanov, and D. Jaccard, “Magnetism and spin fluctuations in a weak itinerant ferromagnet: MnSi,” *Solid State Communications*, vol. 95, no. 10, pp. 707–712, Sep. 1995.

[127] C. Pfleiderer, G. J. McMullan, S. R. Julian, and G. G. Lonzarich, “Magnetic quantum phase transition in MnSi under hydrostatic pressure,” *Phys. Rev. B*, vol. 55, no. 13, pp. 8330–8338, Apr. 1997.

[128] S. Kusaka, K. Yamamoto, T. Komatsubara, and Y. Ishikawa, “Ultrasonic study of magnetic phase diagram of MnSi,” *Solid State Communications*, vol. 20, no. 9, pp. 925–927, Dec. 1976.

[129] S. A. Chaparro, Y. Zhang, and J. Drucker, “Strain relief via trench formation in Ge/Si(100) islands,” *Applied Physics Letters*, vol. 76, no. 24, pp. 3534–3536, Jun. 2000.

[130] I. Bonev, “On the terminology of the phenomena of mutual crystal orientation,” *Acta Crystallographica Section A*, vol. 28, no. 6, pp. 508–512, Nov. 1972.

[131] Á. Barna, B. Pécz, and M. Menyhard, “TEM sample preparation by ion milling/amorphization,” *Micron*, vol. 30, no. 3, pp. 267–276, Jun. 1999.

[132] A. Pramann, O. Rienitz, D. Schiel, J. Schlote, B. Güttler, and S. Valkiers, “Molar mass of silicon highly enriched in ^{28}Si determined by IDMS,” *Metrologia*, vol. 48, no. 2, pp. S20–S25, Apr. 2011.

[133] http://www-d0.fnal.gov/hardware/cal/lvps_info/engineering/elementmagn.pdf, “MAGNETIC SUSCEPTIBILITY OF THE ELEMENTS AND INORGANIC COMPOUNDS.”

Appendix 1: AFM

In this study, most of the imaging was completed using NT-MDT NSG10 and NT-MDT NSG01 cantilevers. The NSG01 has a moderately weak cantilever (resonant frequency 150 kHz), thus allowing operation at lower driving voltages. As a result, the force constant is also low, 5 N/m, compared to that of the stiffer NSG10 tips (240 kHz, 12 N/m). The use of lower force, lower frequency tips allows for increased tip lifetime at the expense of increased sensitivity to absorbed surface layers (e.g. water), although the latter has never caused an issue. Both the NSG10 and NSG01 cantilevers use the same size tip which has a radius of <10 nm. In practice, the best tips have radius of approximately 6 nm. The tip shape is pyramidal, see Figure A1-0-1, and the length of the sharp point is specified to be ~50 nm.

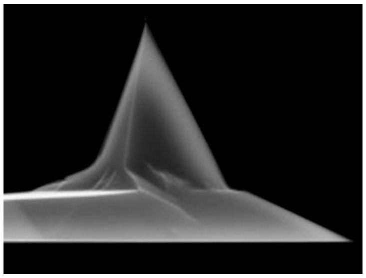

Figure A1-0-1: SEM image of a typical NSG01 AFM tip.

Island size analysis using AFM data

Post processing of AFM was done using both the NT-MDT software as well as Gwyddion software, with the latter being the main program. Gwyddion was used for analysis of height fields to correct any leveling, bowing and tip noise level on AFM images. Besides Gwyddion was also employed to perform statistical analysis on post AFM images. Volume analysis was performed using flooding technique in gwyddion. The zero basic volume was used. This gives the volume between grain surface and the plane z = 0. Values below zero form negative volumes. To use this value, the zero level in the image has to be set to a zero. Figure A1-0-2 shows an application of flooding analysis in determining the volume of material deposited in a film.

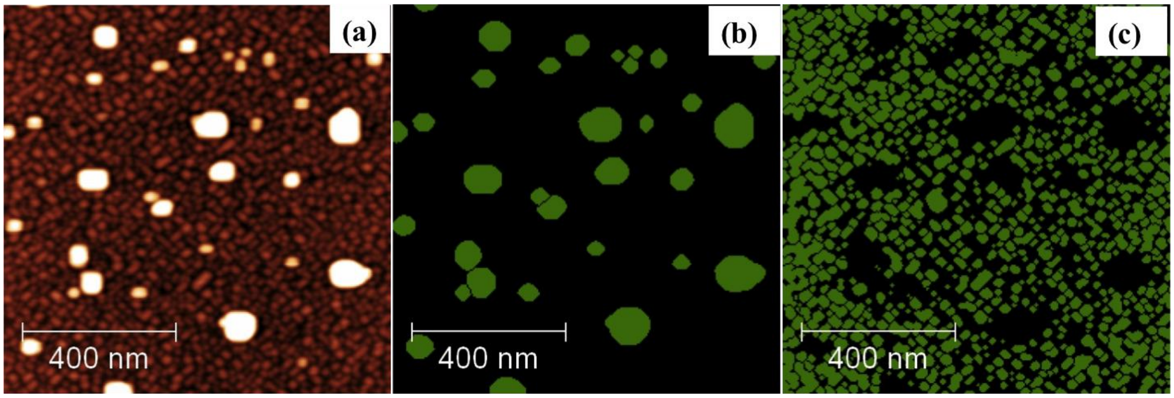

Figure A1-0-2 Volume analysis procedure showing the step-by-step flooding analysis procedure using Gwyddion software package (a) AFM scan to be analyzed (b) flooding analysis representing dome and superdome island volume (c) flooding analysis representing huts/pyramids island volume. In analysis (c) the technique is limited especially while enumerating huts since the grains start coalescing.

Once the masking process is completed, the grain measurement tool is the interactive method to obtain information about individual grains as Grain Distributions in raw mode. Several physical quantities can be extracted from each quantum dot and nanocluster. In particular, we collect the structures' volume Figure A1-0-3, surface area, perimeter, sidewall angle, and max height. The volume of quantum dots obtained from AFM scans was compared with those from TEM micrographs for quantitative comparison tip convolution effect estimation. Since the islands investigated here are approximately equal to the tip radius, volume error is numerically calculated to be nearly 15 to 30% [105]. Tip convolution was observed to vary with the tip radius, island sidewall angle, and island diameter (width).

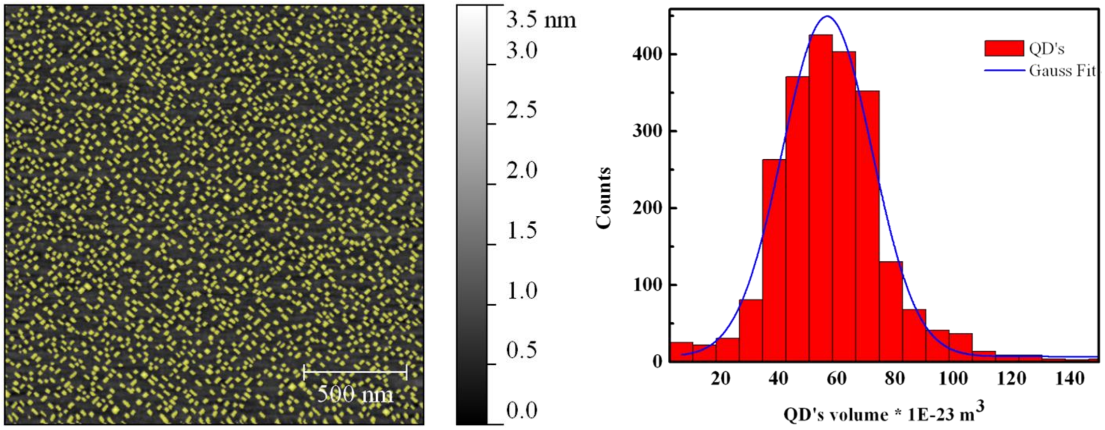

Figure A1-0-3: Left: the 4 µm2 AFM scan of a 6ML Ge/Si (001) QD's grown at $T_g = 550$ ˚C showing a dense array of huts clusters. The yellow coverage represents the flooding volume. Right: Statistical volume distribution of the island with a Gaussian peak used to fit the distribution data. This is a unimodal growth distribution.

Appendix 2: TEM sample preparation

Cross-sectional TEM

For high-resolution imaging, the specimen must be less than 50 nm thick. Mechanical polishing, dimpling and chemical etching techniques were used employed.

Mechanical polishing: A Si wafer is cleaved along the <110> into ≈1 mm x ≈2 mm pieces. These pieces are glued face-to-face using two-part epoxy and then clamped on a non-stick plastic clamp. As illustrated in Figure A2-0-1, edges 1 through 3 of the stacked samples are level and polished to a mirror finish using a 600 to 15 to 12 to 6 to 3 to 1 to 0.5 µm diamond lapping paper (starting with 100 rpms polishing speed down to 10 rpms on the final polishing step). Side 2 is polished to a mirror finish. This process is followed by mounting the mirror polished side (3) of the specimen onto a pyrex sample chuck with crystalbond. The final polishing step is performed on side 4 from a course polish to a final mirror finish polish. After the mechanical polishing is complete, the sample approximately 50 µm thick. The specimen is then detached from the pyrex using acetone to chemically dissolve the crystalbond and avoid any breaking the thinned and specimen through mechanical movements. The thin specimen is then glued onto a TEM grid using epoxy.

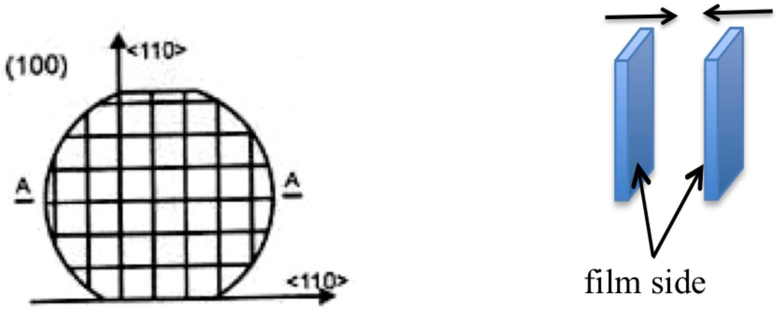

(a) Si wafer is cleaved along the <110> direction into 1 mm x 2 mm pieces

(b) Form stacks with the film side glued together

(c) Level up the Si <111> cleavage edge planes 600 µm diamond lapping paper

(d) PIPS ion mill dual post sample holder loaded with a grid and specimen

Figure A2-0-1: A schematic of the TEM sample preparation step by step process including specimen dicing, mechanical polishing and a final ion mill step.

Ion milling: Ion milling is used to finally thin the sample from several microns to electron transparency. Inert gas, typically argon, is ionized and then accelerated toward the specimen surface. By means of momentum transfer, the impinging ions sputter material from the specimen at a controlled rate. In this dissertation, a Gatan Model 691 precision ion polishing system was employed.

Studies have shown that improved-quality HREM samples can be prepared by reduction of the ion energy to the range of 125–250 eV during the final stage of ion milling [131]. This improvement is due to a reduction in the damaged-layer thickness and hindering of surface roughening. Samples sensitive to oxidization cannot be prepared without an amorphous covering layer, which also avoids surface roughening and results in better images as well. To avoid the misinterpretation of TEM results one should be aware that sputtering by energetic Ar ions during ion milling can cause the formation of artifacts due to the energetic ion beam. Although the applied energy of ion milling is relatively low (3–10 keV), formation of damage and thus the modification of the original sample structure should be considered

Sample preparation for Plan View TEM

This is achieved through chemically back etching the substrate away using HNO_3: HF substrate until an electron transparent film is achieved on the front side. To do this, a $1cm^2$ sample pieces is placed on a glass slide with the film side facing down. Using a painting a fine painting brush, the sample was then covered with Apiezon W wax (black wax) paste along its perimeter to protect the etchant from infiltrating into the film side of the sample. The black wax paste was made from dissolving the solid wax in trichloroethylene (TCE) to the desired thickness. Once the black wax is dry, the substrate was etched away using a solution of HF, $HN0_3$ and acetic acid mixed in the ration 1:1:3. Using a dropper, this solution was applied to the black wax free area in a fume hood until the sample was light transparent.

Dimpling: Dimpling is a rapid technique that involves simultaneously rotating the specimen about one axis and a grinding wheel about a perpendicular and intersecting axis. This combination of motion provides a specimen with its central area reduced to a thickness of a few microns. By thinning only the central area of the specimen, a thick, rugged outer rims remains, eliminating the need for special handling techniques for fragile specimens. This technique creates specimens free from uneven thinning, surface defects, and irradiation damage. A Fishione model number 2000 dimpler was used for this work. An abrasive slurry containing 3 μm suspensions, followed by 1μm and finally a 0.5 μm are used to thin the Si substrate away. The platen that holds the specimen has a glass center section that allows light to be transmitted through the specimen from a source located beneath the specimen stage. This is particularly important when dimpling silicon, which undergoes changes in color relative the sample thickness (Figure A2-0-2) as the specimen approaches electron transparency.

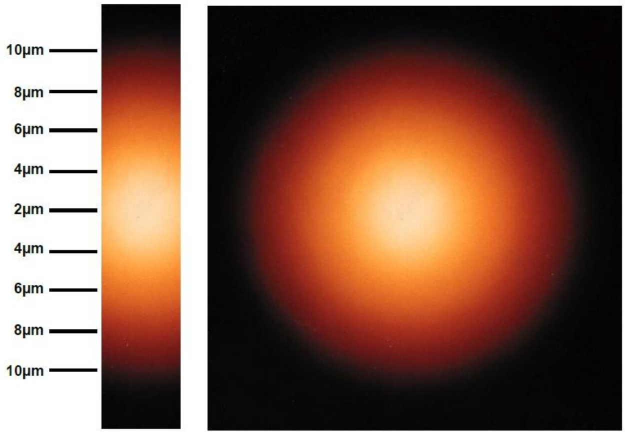

Figure A2-0-2: Dimpling chart showing transparency colors vs. thickness in dimpled si (100) [Gatan Inc.]

The specimen is mounted with a low melting point polymer to the top half of a two-piece platen. The platen fits into a magnetic base, which is coupled to the specimen stage by a rare-earth magnet. This magnetic coupling allows the base to be positioned so that a particular area of the specimen can be precisely placed under the grinding wheel.

Positioning can be observed through a 40X optical microscope. Specimen rotation speed is continuously varied by a front panel mounted potentiometer. For effective preparation and to avoid specimen damage, an electromechanical stage lowers the grinding wheel at an optimized rate. This creates a very controlled reduction of specimen thickness.

Focused ion beam lift-out

This is an alternative technique for TEM sample preparation. A focused ion beam is used to cut thin specimen from precise locations in a large specimen. In this dissertation work, it was critical to lift-out TEM specimen for XTEM analysis due to low nanorods densities in the low Mn concentration samples. This technique ensures that we at least cut through one nanorod, which would otherwise be statistically less likely to hit using polishing techniques. A 20 μm x 1 μm area of interest is selected from the sample being used to produce the FIB lift off sample is coated with ~50 nm e-beam deposited amorphous C at 2 keV followed by a ~300 nm e-beam Pt and finally a ~1.5 nm ion implanted Pt. The purpose of this mask is to protect the underlying QD structures from ion beam damage caused by ion beam implantation (~30nm thickness) and grain interference during TEM imaging. The area-of-interest is milled at an oblique angle exposing two parallel, vertical sides. A needle is then manually positioned on the lamella and “welded” in place using *in-situ* EBID Pt. Following, the vertical edges are milled and the bottom is undercut in order to release the specimen from the substrate.

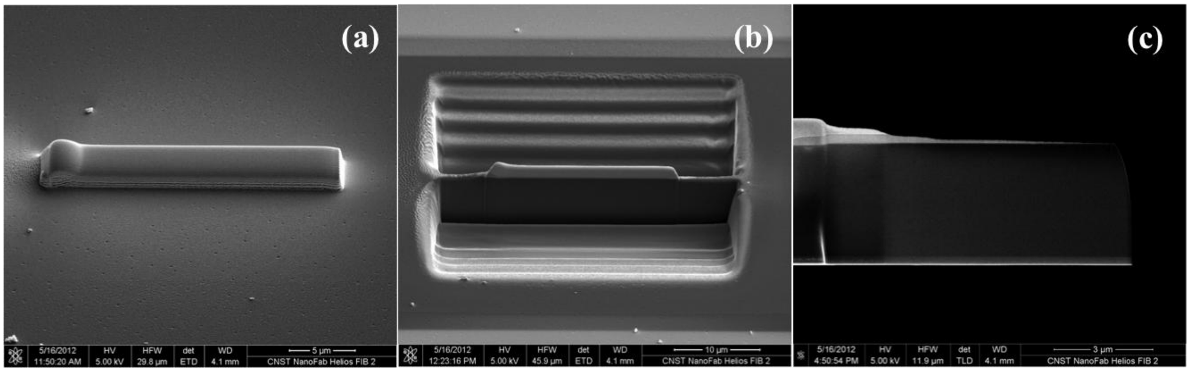

Figure A2-0-3: (a) ~10 µm FIB lift off area post amorphous C and Pt protective coating deposition (b) partially cut out lamella before the bottom and sides are cut to free the lamella (c) Finished cross-sectional TEM lamella after attachment to a post on the TEM half grid. [FIB performed by Dr. Joshua Schumacher at CNST NIST using a FEI Helios Nanolab 650].

Figure A2-0-3 shows a partially milled cross-section using SEM imaging in a dual-beam FIB (left), and a low magnification view of the finished lamella in the TEM (right). A major disadvantage of using FIB thinning technique is that due to the heavy Ga^+ ions used for thinning, an amorphous layer may be created at the surface of the sample. For Si, this layer can be up to 20 nm or more, depending on the conditions used. Finally, upon lifting out the lamella, it is lightly milled using low energy (1-3 keV) Ga+ ions. This light milling mills out the any damaged from previous milling and thins the specimen from 100 µm down to <50 nm. It is important to note that the FIB milling process can damage the quality of crystalline material and makes the very thin regions of the specimen amorphous.

Appendix 3: Deposition rates and calibrations

Calibration

We use a quartz crystal microbalance (QCM) from Maxtek for calibration of all deposition fluxes. In this device, a quartz crystal is actively oscillated during deposition. As mass collects on the crystal, the frequency (*f*) is damped, allowing one to calculate the amount of deposited material for a known density over a period of time. These quantities are related by the following equation:

$$h_f = \frac{N_q \cdot \rho_q}{\rho_f} \left(\frac{1}{f_o} - \frac{1}{f_1}\right)$$ Equation A3-1

where h_f is the film thickness, N_q is the frequency constant for the bare quartz crystal, ρ_q is the density of the quartz, ρ_f is the density of the film, and f_o, f_1 are the frequencies before and after deposition.

Deposition rate trends

Utilizing Equation A3-1, we can determine deposition rates with an uncertainty of approximately 0.01 Å/s. Figure A1 shows two deposition rate charts. In the top panel, DC sputtering deposition rates for Si are plotted for two linear translation distances. At 0”, the gun is fully retracted from the substrate, resulting in an approximate 6” working distance. With a 2” translation, the working distance is approximately 4”. The increase in deposition rate is linear with power, but the effect of working distance is enhanced at larger powers (and hence, sputtering yields).

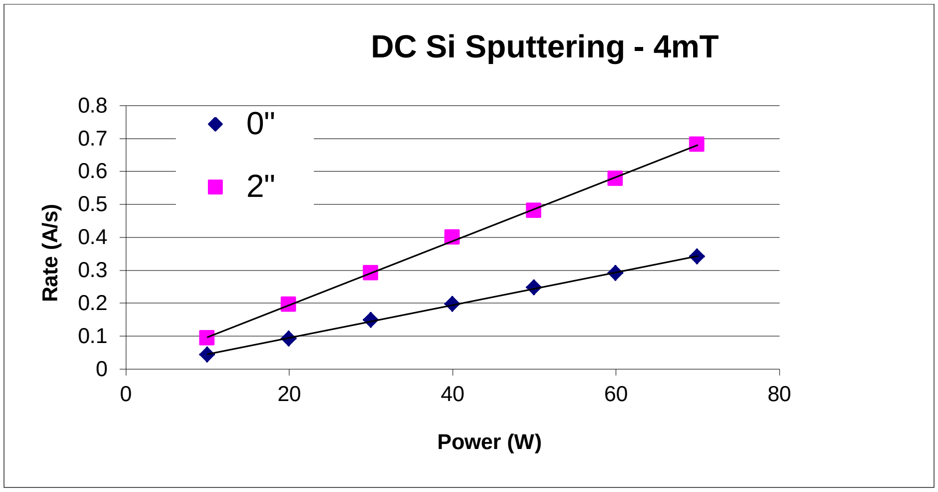

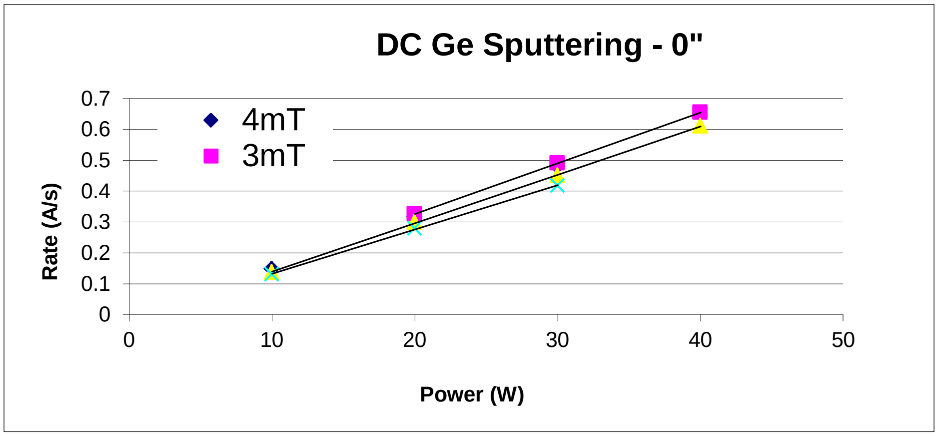

Figure A3-1: (Top) Deposition rate from a Si target as a function of DC power. The two trend lines show linear behavior for each data set collected at different working distances. (Bottom) Deposition rate from a Ge target as a function of DC power. Trend lines show linear behavior for each data set collected at different working pressures [105].

The bottom panel of Figure A3-1 displays DC sputtering deposition rates for Ge for various Ar-process gas pressures. Like Si, the deposition rate of Ge is linear with power. Increased background pressures of Argon ultimately increase scattering and reduces the effective deposition rates. The effects of scattering are slightly enhanced for increased powers.

Ex situ SIMS calibration and impurity detection

We have also performed *ex-situ* secondary ion mass spectroscopy (SIMS) to extrapolate deposition rates and to detect low level impurity incorporation in our films. In the following depth profile (Figure A2-2) the Si and Ge signals have been removed to show detail in the impurity levels. Oxygen and carbon represent the greatest impurities, with especially high levels near the surface. These species are likely introduced into the film by forward recoil sputtering during the SIMS process. The total film thickness was 200 nm; profiling from 200 to 450 nm is into the substrate. There is a spike in B and Mo content at 200 nm which is surface contamination prior to growth.

Most importantly, we find that the metal (Fe, Ni, Mn, and Ta) contents are negligible throughout the film and the substrate. This indicates that we do not observe sputtering of the MBE tooling.

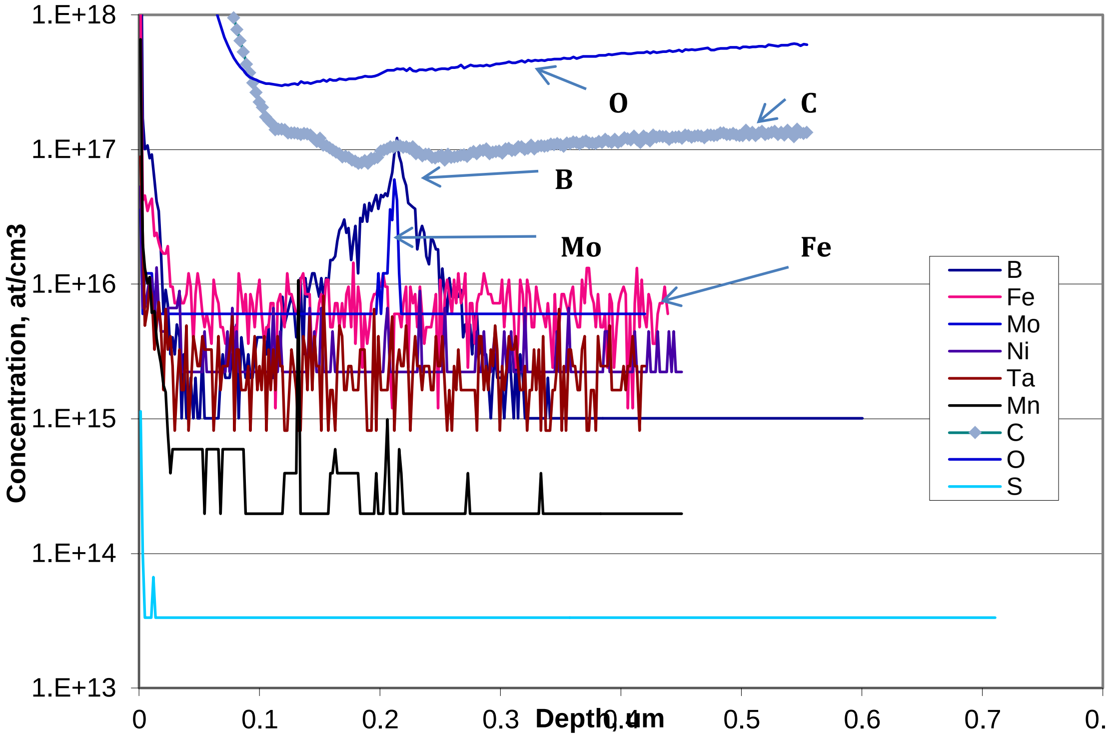

Figure A3-2: SIMS depth profile of a 200 nm SiGe film. The Si/Ge signals have been removed to investigate the impurity concentrations.

Appendix 4: Magnetometry

VSM measurements

To obtain good and repeatable data in the VSM, a few key practices were taken into account. It was critical to ensure that the sample is positioned at the center of the pick up coil level when loading the samples on the sample holder. Mounting samples using GE7031 vanish produced repeatable results, involved less steps that would pose contamination hazards and was a clean procedure. In addition, GE7031 vanish mounting technique did not require any heating steps unlike crystalbond which required the sample holder and consequently the sample to be heated to about 120 ° C. The samples were mounted with the film parallel to the external magnetic field. To detach the sample from the holder, acetone was used as the solvent of choice regardless of the mounting adhesive used. Finally the VSM was occasionally calibrated using the Pd standard to ascertain the condition of the tool

Calibration of the Quantum Design MPMS

Calibration of the Quantum Design MPMS was performed by measuring the *susceptibility* of Pd standard originally purchased from the National Bureau of Standards (NBS Standard Reference Material 765) weighing 0.2630 g at 30 0K.

When a material is placed in a magnetic field H, a magnetization (magnetic moment per unit volume) M is induced in the material which is related to H by $M = \kappa H$, where κ is called the volume susceptibility. Since H and M have the same dimensions, k is dimensionless. A more useful parameter is the molar susceptibility χ_m , defined by $\chi_m = \kappa V_m = k\ M/\rho$ where V_m is the molar volume of the substance, M the molar mass, and ρ the mass density. When the cgs system is used, the customary units for χ_m are $cm^3\ mol^{-1}$. To convert to SI units, χ_m value is multiplied by 4π with units of m^3 mol-1.

As shown in Figure A4-0-1 below, the moment vs. field of the Pd standard has a positive slope and hence implies a positive susceptibility of palladium.

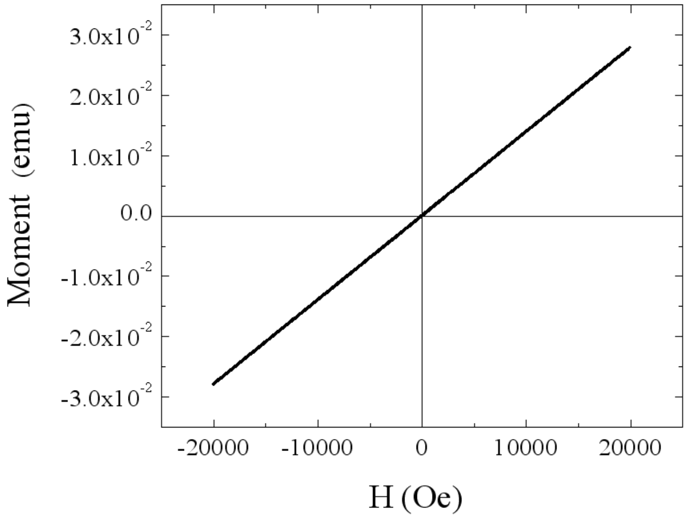

Figure A4-0-1. M(H) curve of Pd standard obtained using the PPMS VSM at 300 K.

From our M v H plot the susceptibility was calculated as the slope of the curve i.e. $\chi = M/H$ which is known as the volume susceptibility. The slope was 1.39494E-6 emu/Oe. Knowing that emu = A m^2 and Oe = A m^{-1}, then the volume susceptibility is in m^3 (SI units) or cm^3 (cgs). Using the mass of the Pd sample (0.2630 g), we determined the magnetic mass susceptibility $\chi_g = \chi$ /mass. The calculated value of $\chi_g =$ 5.3E-6 cm^3/g. This compares very well with literature value shown in Figure A4-0-2 within the allowed tolerance value of ± 0.25% .

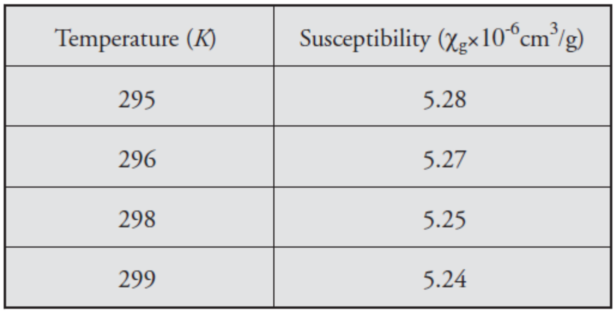

Temperature (*K*)	Susceptibility ($\chi_g \times 10^{-6} cm^3/g$)
295	5.28
296	5.27
298	5.25
299	5.24

Figure A4-0-2: The magnetic gram susceptibility of palladium as a function of temperature. [http://www.qdusa.com/sitedocs/appNotes/mpms/1041-001.pdf]

Diamagnetic susceptibility of Si on a SQUID

In addition to the VSM conducted at UVa, additional magnetic measurements were performed using a superconducting quantum interference device (SQUID) by our collaborator Dr. Jamet Mathieu at the Nanostructures and Magnetism Laboratory, INAC/SP2M CEA-Grenoble, France. The SQUID is a more sensitive device compared to the VSM and is capable of measuring magnetization signal as low as 10^{-11} Am^2. The magnetometry was performed at a 5 T and a temperature range of 5 K to 300 K.

From the SQUID data, the susceptibility is determined by a straight line with its slope fitted with the MvH plot are high fields as shown in Figure A4-0-3.

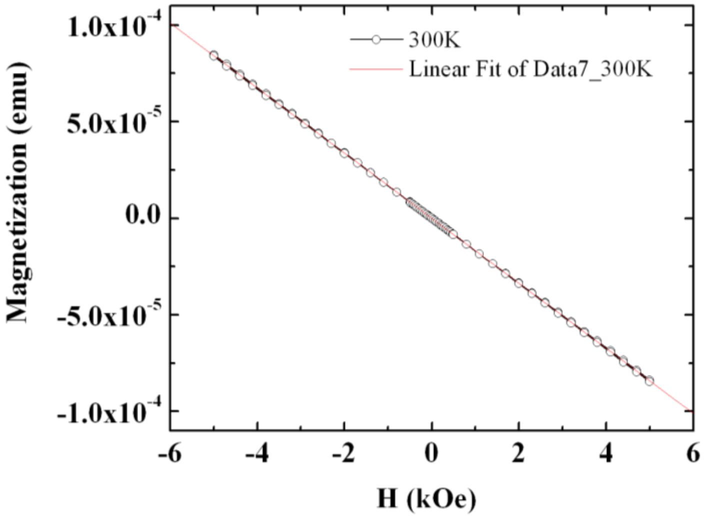

Figure A4-0-3: M(H) of 2% Mn sample weighing 0.0127g performed on a SQUID at

The diamagnetic susceptibility obtained from the above MvH curve of Si. i.e. $\chi = M/H$ was determined to be -1.6857E-9 emu/Oe. Dividing the χ by the mass of the Si sample SQUID sample (0.0127 g) and multiplying with the molar mass of Si (27.976 8 g mol^{-1} [132]), we obtain a molar susceptibility χ_m **= -3.5E-6 $cm^3.mol^{-1}$.** This value compares well with the literature value at room temperature of -3.12 E-6 $cm^3.mol^{-1}$ [133]

Magnetization saturation calculation

```
/* Program to calculate the magnetic moment
 * of Mn in a GeMn/Si(001) thin film
 * using VSM data
 * Date: August 4th 2010
 * By Kassim, J.
 */

#include <stdio.h>
#include <math.h>

int main (void){
/* Local definitions */
     double Borh_num = 9.274E-21; //µB =  9.274 x10-21 emu
          double numOfGeperVol = 4.411E22; //atoms/cm^3
          double Si_wafer_thickness = 0.026162;//280um =
0.0280cm
          float Si_bulk_density = 2.329; //g/cm^3
          //float Ge_bulk_density = 5.323; //g/cm^3
          float Mn_percentage = 0.05;
          float mass_measured = 0.0289;//grams
          float volume; //cm^3 from mass/weight obtained
from micro-scale
          double graph_max_moment = 1.25E-6; // emu
          double film_thickness_in_Ang = 12; //Angstrom
          double film_vol;
          double Ge_num; //numOfGeperVol * Volume
          double sample_area;
          double Mn_num;
          double Max_moment;
          double borh_per_Mn;
          double film_thickness;
          int field_max = 20000;

     /* Statements */
          volume = mass_measured/Si_bulk_density; //cm^3
          film_thickness = (film_thickness_in_Ang* 1E-8);
          sample_area = volume/Si_wafer_thickness; //cm^2
          film_vol = sample_area*film_thickness;
          Ge_num = (numOfGeperVol*film_vol); //atoms
          Mn_num = Ge_num*Mn_percentage;//atoms
          Max_moment = (graph_max_moment/Borh_num); //µB
          borh_per_Mn = Max_moment/Mn_num; // µB/Mn

          printf("Max external field: %d Oe\n",field_max);
```

```
          printf("Mass of sample: %6.4f grams  Film volume:
%ecm^3\n", mass_measured,film_vol);
          printf("Mn dose: %e atoms\n",Mn_num);
          printf("Film thickness: %e cm
\n",film_thickness);
          printf("Mn atomic ratio: %6.4f
\n",Mn_percentage);
          printf("Maximum moment from 5K graph = %eemu
\n",graph_max_moment);
          //printf("Assuming 100 percent of the Mn is
active and using the calculated Mn # = %e atoms\n",
Mn_num);
          printf("M_sat = %7.4f µB/Mn\n",borh_per_Mn);

     return 0;
     }
     /* main */
```

Output file:

```
Max external field: 20000 Oe
Mass of sample: 0.0289 grams  Film volume: 5.691656e-008cm^3
Mn dose: 1.255295e+014 atoms
Film thickness: 1.200000e-007 cm
Mn atomic ratio: 0.0500
Maximum moment from 5K graph = 1.250000e-006emu
M_sat =  1.0737 µB/Mn
```

Ferromagnetism

Besides being a charge carrier, an electron has a dipole moment know as quantum mechanical spin, with the magnetic field either pointing "up" or "down". The spin of the electrons in atoms is the main source of ferromagnetism, although there is also a contribution from the orbital angular momentum of the electron about the nucleus. When these tiny magnetic dipoles are aligned in the same direction, their individual magnetic fields add together to create a measurable macroscopic field. Only atoms with partially filled shells (i.e., unpaired spins) can have a net magnetic moment.

Some substances give rise to a magnetic field in the absence of an applied field, i.e. remanent or spontaneous magnetization. This magnetic remanence is caused by strong interactions between neighboring spins that occur in certain crystals. Exchange energy is minimized when the spins are aligned parallel or anti-parallel depending on the details of the crystal structure. Exchange energy is a consequence of the Pauli Exclusion Principle (no two electrons can have the same set of quantum numbers). In the transition elements, the 3d orbital is particularly susceptible to exchange interactions because of its shape and the prevalence of unpaired spins, so remanence is characteristic of certain crystals containing transition elements with unfilled 3d orbitals. According to classical electromagnetism, two nearby magnetic dipoles will tend to align in *opposite* directions, so their magnetic fields will oppose one another and cancel out. However, this effect is very weak, because the magnetic fields generated by individual spins are small and the resulting alignment is easily destroyed by thermal fluctuations. In a few materials, a much stronger interaction between spins arises because the change in the direction of the spin leads to a change in electrostatic repulsion between neighboring electrons, due to exchange interaction. At short distances, the exchange interaction is much stronger than the dipole-dipole magnetic interaction. As a result, in a few materials, the ferromagnetic ones, nearby spins tend to align in the same direction. **Exchange interaction** is a purely quantum mechanical effect due to the wave function of indistinguishable particles being subject to exchange symmetry, that is, the wave function describing two particles that cannot be distinguished must be either unchanged (symmetric) or inverted in sign (antisymmetric) if the labels of the two particles are changed.

In oxides, oxygen can form a bridge between neighboring cations(TM elements) which are otherwise too far apart for direct overlap of the 3d orbitals in a phenomenon known as superexchange. The result is that the two cations are coupled. For two ions with the same charge, the coupling will be parallel. Exchange energies are huge. As temperature increases, crystals expand and exchange becomes weaker. Above a temperature characteristic of each crystal type (known as the Curie temperature T_c), cooperative spin behavior disappears entirely and the material becomes paramagnetic.

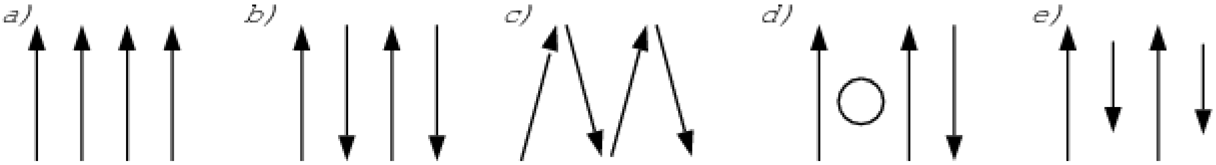

Types of spin alignment in ferromagnetism: a) ferromagnetism, b) antiferromagnetism, c) spin-canted antiferromagnetism, d) defect anti-ferromagnetism, e) ferrimagnetism.